REVIEW

Check for updates

Magnetically driven, plant-extract-modified Fe₃O₄ nanoparticles for sustainable and eco-friendly wastewater detoxification: recent developments

Chanchal Das [ID] [ab] and Goutam Biswas [ID] *[b]

The increasing burden of toxic heavy metals, dyes, pharmaceuticals, and pathogenic microorganisms in aquatic environments necessitates the development of sustainable purification strategies. This review comprehensively elucidates recent progress in the synthesis, characterization, and application of phytogen-based synthesis of functionalized magnetic nanoparticles (phytogen@MNPs) for eco-friendly wastewater treatment. Plant-derived bioactive compounds serve as green capping agents, facilitating the synthesis of multifunctional, biocompatible, and surface-reactive MNPs. This review details diverse phytogenic sources, synthesis methodologies, and advanced characterization techniques, highlighting the influence of surface modification on stability, adsorption efficiency, and superparamagnetic behavior. Applications in the adsorption and catalytic degradation of inorganic, organic, and microbial contaminants are critically discussed, along with the kinetics, isotherms, and thermodynamics of pollutant removal. The antibacterial properties, reusability, and impact of real water matrices are covered, highlighting the superior performance and cost-effectiveness of phytogen@MNPs. Mechanistic insights into pollutant–nanoparticle interactions reveal the decisive roles of surface functionalization and particle size. This review also encompasses the advantages of phytogen@MNPs over conventional materials, while also identifying the need for standardized protocols, evaluation of long-term stability, and strategies for scalable production to fully realize their potential in environmental remediation in future work.

1. Introduction

Every year, large amounts of toxic inorganic and organic pollutants, such as harmful heavy metals (cations, oxycations, and oxyanions), organic dyes, and pharmaceutical wastes, are discharged because of overproduction, overuse in various applications, and overprescription.[1] These detrimental contaminants are directly or indirectly discharged into rivers and oceans, where they adversely affect the flora and fauna. In addition to these pollutants, pathogenic microorganisms persist in surface water, which is the primary reason why water remains non-potable even after undergoing purification processes.[2] The removal of toxic metal ions, organic pollutants, and harmful microbes from wastewater can provide clean and pure drinking water.

Among the different types of materials and composites, nanoparticles (NPs) have been extensively developed for wastewater purification applications. NPs can be of various types, such as metals, metal oxides, metal sulfides, and spinel materials. In this study, we focused on magnetite nanoparticles (MNPs). Iron oxide nanoparticles are generally of three types:

hematite (α-Fe₂O₃), maghemite (γ-Fe₂O₃), and magnetite (Fe₃O₄).[3] The latter two interact strongly with the magnetic field, whereas hematite is weakly magnetic. MNPs are superparamagnetic mixed metal oxides with Fe(II) and Fe(III) ions in octahedral and tetrahedral sites (inverse spinel cubic lattice), respectively. They can also be easily prepared using straightforward methods and recycled for numerous cycles, making them cost-effective materials.[4] Surface-modified MNPs can be classified into two categories based on the selection of surface modifiers: chemically modified and biogenic or biomodified. Biomodified magnetic nanoparticles (MNPs) are distinguished by their unique properties, as they can be synthesized in a cost-effective and environmentally sustainable manner under open-air conditions, utilizing extracts from leaves, crude latex, bark, and seeds of various plants. There is growing research interest in the fabrication of MNPs by biomodification, that is, surface modification with various bioactive compounds, including phytogens, enzymes, peptides, and fungi, and their application in water and wastewater treatment. Here, we discuss only phytogen@MNPs, which are found in various plant parts and extracted using specific solvents. Polyphenols, flavonoids, terpenoids, peptides, nucleic acids, enzymes, cellulose, and starch are phytogens. The features of nanoparticles, such as biocompatibility, stability, magnetic properties, functionality, and band gap, can be modified by phytogen coating or

aDepartment of Chemistry, Saheed Kshudiram College, Uttar Kamakhyaguri, Alipurduar, West Bengal-736202, India

bDepartment of Chemistry, Cooch Behar Panchanan Barma University, Vivekananda Street, Cooch Behar, West Bengal-736101, India. E-mail: goutam@cbpbu.ac.in

biomodification. These phytogen@MNPs were more advantageous than other chemically modified MNPs.

These nanoparticles were characterized with respect to their structural, morphological, magnetic, and thermal stability properties using advanced techniques such as dynamic light scattering (DLS), ultraviolet-visible (UV-vis) spectroscopy, Fourier-transform infrared (FTIR) spectroscopy, powder X-ray diffraction (pXRD), field emission scanning electron microscopy (FE-SEM), high-resolution transmission electron microscopy (HRTEM), superconducting quantum interference device (SQUID)/vibrating-sample magnetometry (VSM)/alternating gradient magnetometry (AGM), and thermogravimetric analysis (TGA).

The properties of these phytogen@MNPs include a high surface area-to-volume ratio, availability, cost-effectiveness, ease of dispersion in solutions, ability to generate reactive oxygen species (ROS), rapid adsorption kinetics, and superparamagnetic properties. Owing to their high saturation magnetization values, facile separation from the reaction mixtures can be achieved using a simple magnet. MNPs have been suggested as crucial agents or carriers in cancer treatment because of their distinct dynamic magnetization in response to alternating magnetic fields, such as in magnetic hyperthermia therapy.[5] Magnetic materials with nanoscale to microscale particle sizes are appealing for use in biological and medicinal applications, as well as in wastewater treatment and magnetic recording.[6] Most of these applications require nanoparticles that are evenly sized, shaped, and distributed in a solvent.[7] For example, nanoparticles at the nanometer scale can bind with DNA or proteins via a capillary tube, whereas microparticles are limited to interactions with cells.[6,8] Furthermore, the attainment of single-domain particles and superparamagnetic behavior is contingent upon the critical size being within the range of 30–50 nm.[9] Functionalized MNPs have many such applications, including drug carriers,[10] drug release,[11] cancer therapy,[12] magnetic resonance imaging (MRI),[13] proton exchange membranes,[14] catalysis[15–18] and sensors.[19] Their biocompatibility and lack of

toxicity make them suitable for use in biotechnology.[20] A comparison table for phytogen@MNPs with other NPs is given in Table 1.

Owing to their small size, large surface area, and reactive surface sites, nanomaterials have shown excellent effectiveness in decreasing pollutant concentrations in adsorption and catalytic degradation studies. Batch adsorption methods and kinetic modeling demonstrated that phytogen@MNPs are significantly more cost-effective than traditional adsorbents and photocatalysts. Moreover, they exhibit high efficacy in removing heavy metals, dyes, pharmaceutical residues, and bacteria. Many review articles related to the synthesis and application of biogenic or plant extract-mediated MNPs have been published, discussing either the synthesis or a few specific applications, such as anticancer and drug delivery.[21,22] Some review articles of a similar kind discuss the removal of microorganisms,[23] and few address synthesis and provide a brief discussion on environmental and biomedical applications.[24] Among these articles, either the synthesis methodology, application, or both are missing, along with a brief discussion and mechanism. Therefore, our brief mechanistic findings highlight the potential of tailored MNPs for environmental cleanup and offer insights into the design of more efficient and sustainable materials. This study underscores the importance of functional group modification and the formation of phytogen@MNPs to enhance the performance of MNPs in real-world applications. Future work will focus on scaling the synthetic process and testing the long-term stability and reusability of these materials under various environmental conditions.

2. Various phytogens and phytogen-coated nanoparticles

Plants and their derivatives have garnered significant interest in the synthesis and fabrication of nanoparticles. This interest is due to the presence of phytogenic compounds, such as

Table 1 Comparison of phytogen@MNPs with other metal oxide (TiO$_2$, ZnO, CuO) NPs

Parameter	Phytogen@MNPs	Phytogen coated other metal-oxide (TiO$_2$, ZnO, CuO) NPs
Separation by an external magnet	Phytogen@MNPs are recovered using an external magnet after preparation and application, which makes wastewater purification easier and effective	These NPs lack inherent magnetism and require complex separation like centrifugation, therefore making recovery difficult and complicated after wastewater purification
Mechanism of removal	Adsorption, photocatalytic degradation, Fenton-like oxidation	Adsorption, photocatalytic degradation, but not Fenton-like oxidation
Catalytic performance	Low photocatalysis efficiency is observed	Higher photocatalysis efficiency is observed for TiO$_2$ and ZnO under UV/visible irradiation
Recyclability	Due to the simple and effective magnetic recovery process, reusability frequency or recyclability are higher	As these are non-magnetic, hence the recovery process is complex and difficult, making it less recyclable
Cost analysis	Fe salts are relatively cheaper than other metal salts (Cu, Zn and Ti). Also, convenient magnetic separation makes the cost of production much less	Other metal salts are relatively expensive, and also in some cases use of non-aqueous solvents and an inert atmosphere makes overall production slightly expensive
Environmental toxicity	MNPs themselves have been proven to be less/non-toxic towards aquatic as well as normal cell lines at higher concentrations	Toxicity varies depending on concentration, e.g., ZnO and CuO NPs have a considerable toxicity profile while TiO$_2$ NPs are relatively safer at higher concentrations

flavonoids, polyphenols, ascorbic acid, sugars, proteins, gums, and pectic molecules, which contain various coordinating groups, including –OH, –NH$_2$, –CONH$_2$, >C=O, and –COOH. These compounds act as stabilizing agents, provide multifunctionality, and impart biocompatibility to NPs on the surface. Some common plants containing bioactive molecules are discussed below.

Tinospora cordifolia is a well-known medicinal plant that is used in traditional medicine to treat various illnesses. Amrita, Guduchi, and Gulancha are common names of the Menispermaceae family. It has been used to treat a wide range of illnesses, including fever, diarrhea, leprosy, skin conditions, and diabetes. It is regarded as an essential plant in the Indian medicinal system. Alkaloids, terpenoids, lignans, steroids, and other chemical compounds have been identified in *Tinospora cordifolia*, supporting its phytochemical and pharmacological activities. In particular, it has antiinflammatory, antimicrobial, antibacterial, antifungal, antidiabetic, antistress, hypolipidemic, hepatic, anticancer, antiHIV, antiosteoporotic, antitoxic, wound-healing, anticomplementary, immunomodulatory, systemic infection, and anti-Parkinson's disease effects.[25–27] Using various parts of *T. cordifolia*, several types of NPs, such as silver nanoparticles (AgNPs),[28] titanium dioxide (TiO$_2$) NPs,[29] magnesium oxide (MgO) NPs,[30] copper nanoparticles (CuNPs),[31] and zinc oxide (ZnO) NPs,[32] have been synthesized. These nanoparticles have been employed as antibiofilm agents, photocatalysts, antibacterial agents, diabetes regulators, antioxidants, antiinflammatory agents, and adsorbents for lead, iron, phosphate, and arsenic ions.

Various parts of the *Azadirachta indica* (*A. indica*) plant are used in traditional medicines. Some important polyphenolic phytochemicals found in the ethanolic extract of *A. indica* leaves include ellagic acid, quercetin, quercetin-3-*O*-glucoside, gallic acid, 2,3-(*S*)-hexahydroxydiphenoyl-(α/β)-D-glucopyranose, avicularin, and castalagin. Abdulhady *et al.* reported that these substances exhibit strong cytotoxic and antioxidant properties.[33] The presence of hydroxyl groups in the chemical structures of phenolic compounds may account for the substantial free radical scavenging capacity observed in neem leaves.[33] Various nanoparticles, including TiO$_2$, ZnO, CuO, α-Fe$_2$O$_3$, Fe$_3$O$_4$@ZnO, and MoO$_3$, have been synthesized using different components of the *A. indica* plant.[34] These nanoparticles have been employed for the adsorption of different adsorbates, degradation of various molecules, sensing, thermal catalysis, cytotoxicity, dye degradation, and antimicrobial activity. *Jatropha curcas* (*J. curcas*) is of significant commercial interest because of the industrial-scale extraction of biodiesel from its seeds.[35,36] Although *Jatropha* latex has some ethnomedical uses, such as wound healing and coagulant activities in the blood,[37] it is acrid and irritating to the skin.[38] Extensive studies on *J. curcas* have revealed that the major constituents of its latex are curcain (an enzyme), curcacycline A (a cyclic octapeptide), and curcacycline B (a cyclic nonapeptide).[39] *J. curcas* plant parts can be used to synthesize NPs, such as lanthanum cobalt oxide (La$_2$CoO$_4$),[40] AgNPs,[39]

and ZnO,[41] which have been studied for catalysis, single-molecule magnets, and bacterial removal.

The *Cinnamomum tamala* (CT) leaf is a well-known Indian spice, called "Indian bay leaf" or "tejpatta", which is used as a traditional medicine in the treatment of scabies, anal diseases, rectal disorders, heart troubles, bad taste, ozena, diarrhea, *etc.*[42] Because CT leaves have antioxidant and antibacterial properties, they may also be used as antifouling agents for ships and boats in marine and freshwater systems in the future.[43,44] The aqueous part of CT leaf extract consists of eugenol and kaempferol (as the main ingredients) and many flavonoids,[45,46] which possess various coordinating groups such as hydroxyl (–OH) and carbonyl (>C=O) groups. Hence, this extract was used as a surface modifier for nanoparticle synthesis. CT extract has also been used to reduce metal ions to produce metal nanoparticles.[47] Using this, AgNPs[48] and ZnO[49] have been synthesized and successfully applied in catalysis and photocatalysis.

Terminalia arjuna (TA) is another traditional medicine used for the treatment of rheumatic heart disease, endothelial dysfunction, hypertension, oxidative stress, and a few other health conditions and has a good antibacterial effect.[50,51] In traditional medicine, a combination of elixir from TA bark with milk or ghrita is used to treat ulcers, whereas bark ash is used to treat snakebites and scorpion stings.[52] TA bark contains flavonoids, β-sitosterol, triterpenoids, polyphenols, steroids, and glycosides, which have no negative side effects.[53,54] Various parts of TA were used to prepare various types of NPs, such as MNPs,[54] Cu, and AgNPs embedded in multiwalled carbon nanotubes (MWCNTs),[55] which were used for the adsorption of contaminants from water and were successfully applied to study antimicrobial and anticancer activities.

Some parts of Asia and several southern European countries are home to the annual blooming plant *Nigella sativa* L. (NS). Seeds of this plant, known as black cumin, are well-known spices that are sometimes referred to as black seeds or black caraway seeds. People from the Middle East and Far East Asia have been using this plant to cure ailments such as headaches, asthma, infections, dysentery, back pain, obesity, gastrointestinal disorders, and hypertension, as it is identified to have healing properties in traditional medicine.[56] It is generally called 'kalonji' or 'kala jeera' and is extensively used as traditional medicine and in cooking within India. NS seeds primarily consist of 2-isopropyl-5-methyl-1,4-benzoquinone (thymoquinone, TQ), which has good anticancer, antineoplastic, antiinflammatory, and antimicrobial properties.[57] Furthermore, NS has been documented to possess antioxidant properties in various animal models of neurological disorders, and several human studies corroborate these findings. NS seeds normalize the level of glutathione and thus activate enzymes with antioxidant properties, such as superoxide dismutase, catalase, and glutathione peroxidase.[58] NS seed extract and TQ are also effective against a few infectious and non-infectious allergies, as well as other skin disorders,[59] and have antidiabetic effects.[60] Ali *et al.*[61] studied the toxicological and pharmacological properties of NS and found that it is safer to use. Various NPs

Table 2 Plant extracts containing bioactive compounds and examples of nanoparticles synthesized using these extracts
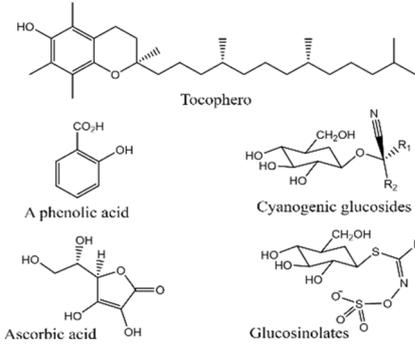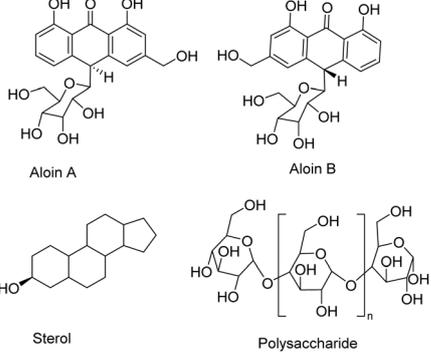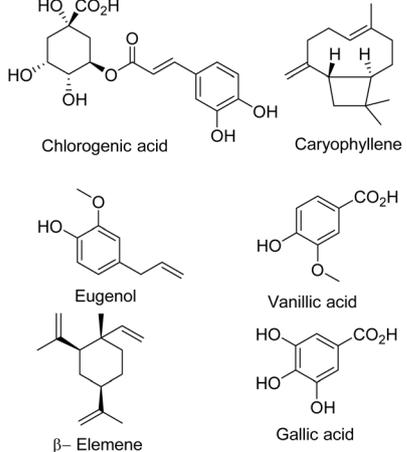
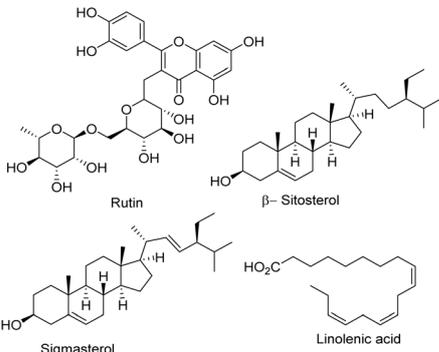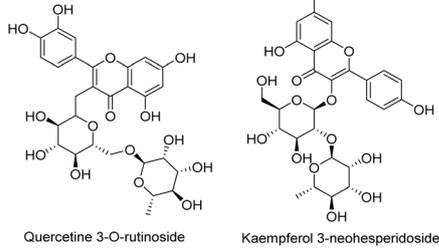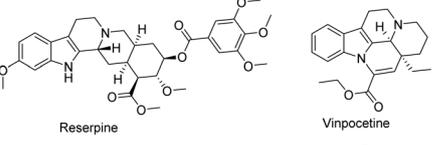| Plant	Plant extract containing major compounds	Nanoparticles synthesized	Reference
Carica papaya	Tocophero; A phenolic acid; Cyanogenic glucosides; Ascorbic acid; Glucosinolates	Fe_2O_3NPs, Fe_3O_4NPs, AgNPs, ZnONPs, ZnO-CuONPs	66–71
Aloe vera	Aloin A; Aloin B; Sterol; Polysaccharide	BiZnFe NCs, α-Fe_2O_3NPs, Fe_3O_4NPs, AgNPs	72–76
Ocimum sanctum	Chlorogenic acid; Caryophyllene; Eugenol; Vanillic acid; β-Elemene; Gallic acid	CoNPs, Pd@CuONPs, CuNPs, AgNPs	77–81

Table 2 (*Contd.*)

Plant	Plant extract containing major compounds	Nanoparticles synthesized	Reference
Clitoria ternatea	Rutin, β–Sitosterol, Sigmasterol, Linolenic acid, Quercetine 3-O-rutinoside, Kaempferol 3-neohesperidoside	Co_3O_4NPs, AuNPs, AgNPs, CuNPs, ZnO/NiONPs	82–85
Catharanthus roseus	Reserpine, Vinpocetine, Ajmalicine, Serpentine, Quercetin, Kaempferol	$CuAl_2O_4$NPs, AgNPs, ZnONPs, TiO_2NPs	86–90
Saraca asoca	n-Decanoic acid, Catechin, Procyanidin B2, Benzene-1,2-dioic acid, Lupeol, Methyl commate D	MnO_2NPs, AgNPs, FeNPs, Ag@α-Fe_2O_3NPs, CuONPs	91–97
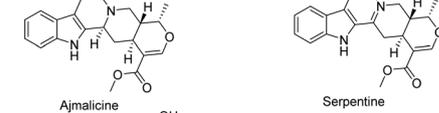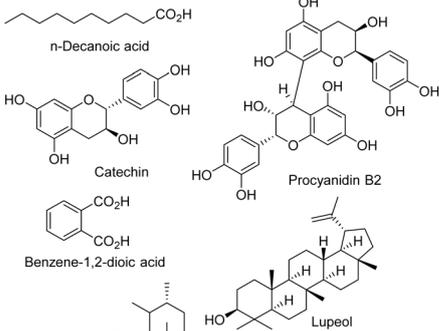
Table 2 (*Contd.*)

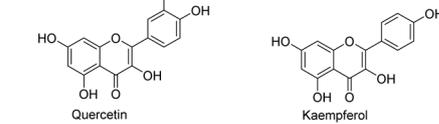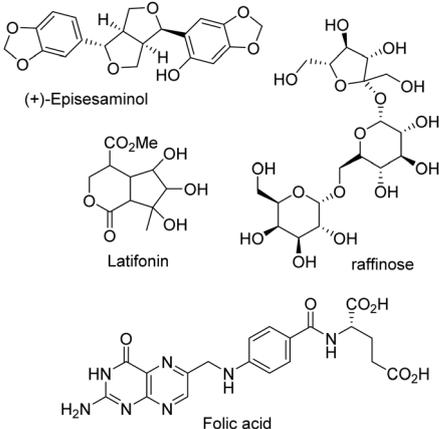| Plant	Plant extract containing major compounds	Nanoparticles synthesized	Reference
Sesamum indicum	(+)-Episesaminol, Latifonin, raffinose, Folic acid	ZnNPs, $Mn_x Co_{1-x} Al_2 O_4$, FeNPs, MnSNPs	98–102
Tagetes patula	Quercetagetin, Patuletin, Quercetin-3-glucoside, Isoeuparin, 4-vinyl guaiacol	CuSNPs, AgNPs, CuNPs	103–107
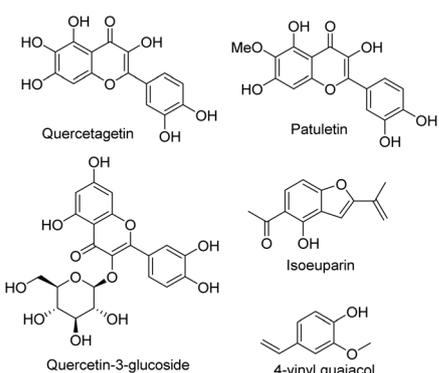
functionalized with NS seed phytogens, including AgNPs,[62] CuNPs,[63] ZnO NPs,[64] and TiO_2 NPs,[65] have been reported to exhibit antibacterial, anti-obesity, and anticancer properties.

Overall, these plant parts and their extracts can be used for efficient fabrication of NPs. A few other common plants and extracts of different plant parts containing these compounds are listed in Table 2.

This review explores innovative green synthesis methods for MNPs, emphasizing the role of plant-derived bioactive compounds in the fabrication of nanoparticles.

3. Synthesis of magnetite nanoparticles

Magnetite nanoparticles have been synthesized using various physical, chemical, and biological approaches. Chemical co-precipitation is the simplest and most commonly used method. Other categories of synthetic procedures for MNPs include bottom-up and top-down methods.[108] Here, we only discuss the bottom-up approach. Examples of synthetic approaches for all categories are listed in Table 3.

3.1 General synthetic procedure for phytogen@MNPs

Massart *et al.*[124] first synthesized MNPs *via* co-precipitation in 1981, after which they were widely investigated. The first biosynthesized MNPs were reported by Blakemore *et al.* (1975)[125] in magnetotactic bacteria, and the first images of phytogen@MNPs in magnetotactic bacteria were captured by Williams *et al.* in the 1990s.[126] In subsequent studies, various phytogen@MNPs were synthesized in the laboratory using diverse methodologies. However, this discussion focuses on the synthesis of phytogen@MNPs derived from different plant extracts. Phytogens contribute to the stabilization of nanoparticles and enhance their bioactivity, as well as their adsorption and degradation capabilities. Phytogen@MNPs can also be prepared using the co-precipitation method, which is convenient, eco-friendly, and cost-effective. In a conventional procedure, ferrous salts (*e.g.*, $FeCl_2$, $FeSO_4$) and ferric salts (*e.g.*, $FeCl_3$, $Fe_2(SO_4)_3$) are combined in a 1 : 2 ratio to form a solution. Subsequently, an extract from a specific plant part was introduced, followed by the addition of NaOH solution to maintain an alkaline pH (~11). Following additional stirring, magnetic separation, and repeated washing four to five times, the final

Review

Table 3 Various reported synthetic procedures for magnetite nanoparticles

| Synthetic procedure	Typical methodology	References
Thermal decomposition	Fe(III) solution + surfactant solution + heating under an inert environment	109 and 44
Sonochemical	Fe(III) + Fe(II) solution + HCl solution + ammoniacal hydrazine + ultrasonication in a plastic tube with heating	110 and 111
Electrochemical	Electrodes: Hg$\|$Hg$_2$SO$_4$, a platinum wire, and an iron rod. Electrolyte: saturated K$_2$SO$_4$ solution	112–114
Hydrothermal	Fe(III) solution + surfactant + hydrazine + stirring + heating in an autoclave	115,116
Microemulsion	Lipophilic solvent + aqueous solution of metal ions and surfactant + stirring + evaporation	117–119
Biological	Biological culture + metal ion containing solution	120–122
Co-precipitation	Fe(III) + Fe(II) salt solution + coating agent + OH$^-$ (pH~11)	9 and 123
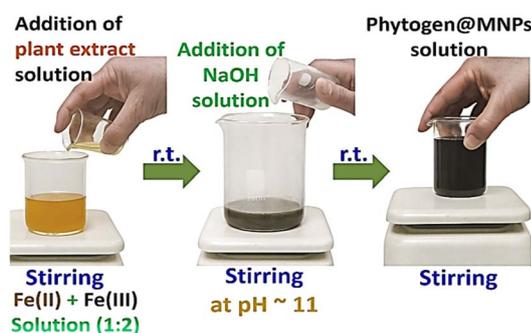
Fig. 1 Typical co-precipitation methods for the synthesis of phytogen@MNPs.

separation and drying processes yielded the desired phytogen@MNPs (Fig. 1).

Washing several times with deionized water and other solvents is an important step in the preparation of MNPs. This is because some ferrous/ferric hydroxides, along with an excess concentration of the base (*e.g.*, sodium hydroxide, ammonium hydroxide, *etc.*) and the coating agent, were removed during this process. Drying is crucial for the removal of adsorbed water molecules, as their presence in the FTIR spectra results in a broad and high-intensity peak, which is undesirable.

A comparison of various plant extract-mediated magnetite nanoparticles is shown in Table 4. The analysis of the table indicates that an open-air environment and aqueous solutions are adequate for the synthesis of MNPs when a concentrated plant extract solution is introduced. In most cases, NaOH was

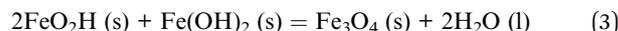**Table 4** Phytogen@MNPs synthesized under various conditions

Phytogen@MNPs	Fe-salts	Plant extract	Base	Synthetic procedure	Reaction environment	pH, temperature, time
TOL@MNPs[16]	FeCl$_3$ (1 g), FeSO$_4$ (1 g)	*Taraxacum officinale* leaf (aq.)	NH$_3$ (30%)	Refluxometry	Open-air	pH 10, rt and then boiling, 60 min and then 190 min
TC@MNPs[15]	FeCl$_3$ (2 g), FeSO$_4$ (1 g)	*Tinospora cordifolia* leaf (aq.)	NH$_4$OH (25%)	Refluxometry	Open-air	pH 10, rt and then 100 °C, 60 min then 180 min
MC@MNPs[128]	FeCl$_3$ (1 M)	*Matricaria chamomilla* flower (aq.)	NaOH (8 M)	Microwave	Open-air	260 °C, 5 min
NS@MNPs[129]	FeCl$_3$ (1.62 g), FeCl$_2$ (0.65 g)	*Nigella sativa* seed (aq. alc.)	NaOH (3.19 M)	Coprecipitation	Open-air	pH 11, rt, 60 min
Pom@MNPs[130]	FeCl$_3$ (2 mM), FeCl$_2$ (1 mM)	Pomegranate peel (aq.)	NaOH	Coprecipitation	N$_2$-gas	pH 10, rt (if NaOH is used) or 60 °C (if NH$_3$ is used as base), 65 min
ACV@MNPs[18]	FeCl$_3$ (1 mM), FeSO$_4$ (1 mM)	*Adiantum capillus-veneris* (aq.)	NaOH (10%)	Refluxometry	Open-air	pH 10, rt, 180 min
TA@MNPs[54]	FeCl$_3$ (0.65 g), FeCl$_2$ (0.26 g)	*Terminalia arjuna* bark (aq.)	NaOH (6.4 M)	Coprecipitation	Open-air	pH 11, rt, 60 min
TS@MNPs[131]	FeCl$_3$ (13.6 g), FeCl$_2$ (5 g)	*Thymus schimperi* leaf (aq.)	NaOH (2 M)	Coprecipitation	Open-air	60 °C, 60 min
CP@MNPs[127]	FeCl$_3$ (6.25 g), FeCl$_2$ (3.12 g)	*Calotropis procera* leaf (aq.)	NaOH (1.0 M)	Coprecipitation	Open-air	pH 11, 80 °C, 80 min
CS@MNPs[132]	FeCl$_3$ (0.2 M), FeSO$_4$ (0.1 M)	*Citrus Sinensis* peels (aq)	NaOH (0.1 M)	Coprecipitation	Open-air	pH 11–12, rt, 30 min

used as the base, and no other chemicals were used; hence, the procedure for the preparation of plant extract-mediated MNPs was greener and more cost-effective. Kalu et al.[127] synthesized MNPs using an aq. extract of *Calotropis procera*. They qualitatively analyzed the plant extract and found it to contain polyphenols, flavonoids, alkaloids, tannins, and saponins with total contents of 43.54 (mg g^{-1}), 33.83 (mg g^{-1}), 28.38 (mg g^{-1}), 25.95 (mg g^{-1}), and 24.42 (mg g^{-1}), respectively. Each phytochemical contains several coordinating groups that effectively coordinate with MNPs.

3.2 Mechanism of synthesis of magnetite nanoparticles and dependency on various factors

The preparation of MNPs can be described by eqn (1)–(3) applying a 2 : 1 molar ratio of Fe(III) and Fe(II) at pH ~11.[54]

$$Fe(III) \ (aq) + Fe(II) \ (aq) + 5OH^- \ (aq) = Fe(OH)_3 \ (aq) + Fe(OH)_2 \ (s) \quad (1)$$

$$Fe(OH)_3 \ (s) = FeO_2H \ (s) + H_2O \ (l) \quad (2)$$

$$2FeO_2H \ (s) + Fe(OH)_2 \ (s) = Fe_3O_4 \ (s) + 2H_2O \ (l) \quad (3)$$
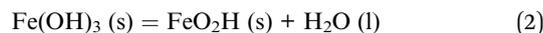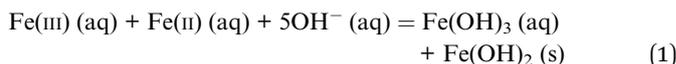
The growth, size, magnetic susceptibility, and nucleation of the produced nanoparticles were regulated by an alkaline medium or [OH$^-$]. The concentrations of Fe(III) and Fe(II) also affected the size and concentration of the Fe$_3$O$_4$ nanoparticles.

Akbar et al.[133] altered the Fe^{3+}/Fe^{2+} ratio to 1, 1.25, 1.5, 1.75, and 2. The application of Fe^{3+} cations caused iron oxide to form in both the hematite and maghemite phases; however, the use of Fe^{2+} cations caused the formation of the maghemite phase. Based on their report, it can be said that the maghemite phase was produced by varying the Fe^{3+}/Fe^{2+} ratio to 1, 1.25, 1.5, and
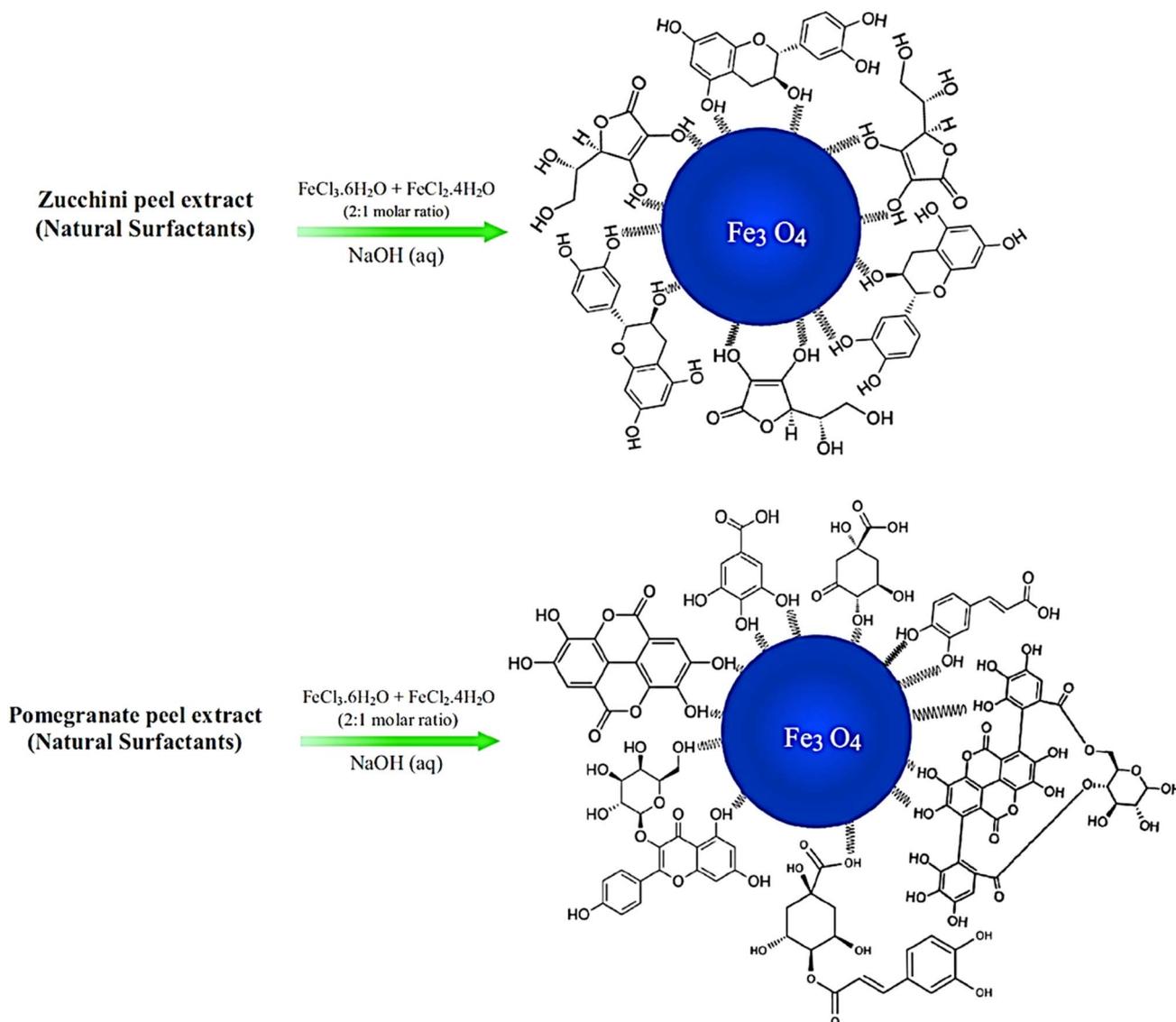

Fig. 2 Interaction of zucchini and pomegranate peel extract containing phytogen with magnetite nanoparticles (source: this image is taken from an article written by Etemadifar et al.[134]).
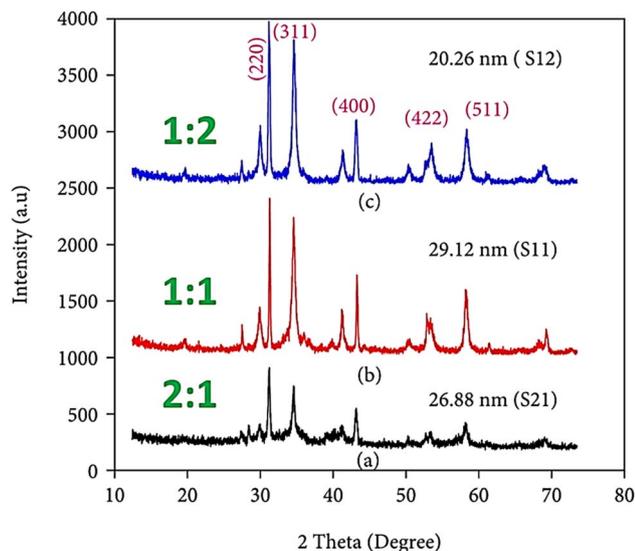
Fig. 3 pXRD patterns of MNPs synthesized using the leaf extract of *Thymus schimperi* in different ratios of plant extract to Fe salts: (a) 2 : 1, (b) 1 : 1, and (c) 1 : 2 (source: this image is taken from an article written by Geneti *et al.*[131]).

stability of zucchini and pomegranate peel extract-containing phytogen@MNPs is due to electrostatic forces, which also helps to prevent agglomeration (Fig. 2).

The ratio of the plant extract to the corresponding Fe salt is also an important factor that determines the formation and stability of the phytogen@MNPs. Geneti *et al.*[131] synthesized MNPs using the leaf extract of *Thymus schimperi* and applied them to remove chromium (Cr) and mercury (Hg). They synthesized MNPs using three different ratios of plant extract to iron salts: 2 : 1, 1 : 1, and 1 : 2. They concluded that the formation of crystal planes in the MNPs was indistinct when the plant extract contained twice the amount of salt precursors. Conversely, when the plant extract was half the amount of salt precursors, the crystal planes were well defined (Fig. 3), and the crystal sizes increased. The corresponding powder XRD patterns are shown in Fig. 3a–c.

4. Characterization techniques

Following the synthesis of MNPs, their characterization is crucial because it offers a definitive understanding of their stability, magnetic properties, and potential applications across various fields.

4.1 DLS and zeta potential study

DLS is frequently used to determine the hydrodynamic diameter of MNPs by generating dilute suspensions. The hydrodynamic diameter is defined as the diameter of hydrated

1.75, whereas the magnetite phase was formed when the ratio was 2.

The introduction of coating materials is another important aspect that determines the stability of MNPs through van der Waals interactions, and electrostatic, covalent, and hydrogen bonding. For instance, Etemadifar *et al.*[134] reported that the

Fig. 4 (a) ZP at neutral pH, (b) histogram of hydrodynamic size, and (c) ZP at various pH values for *Citrus reticulata* (mandarin) peel inspired magnetite nanoparticles (source: this image is taken from an article written by Nassar *et al.*[139]).
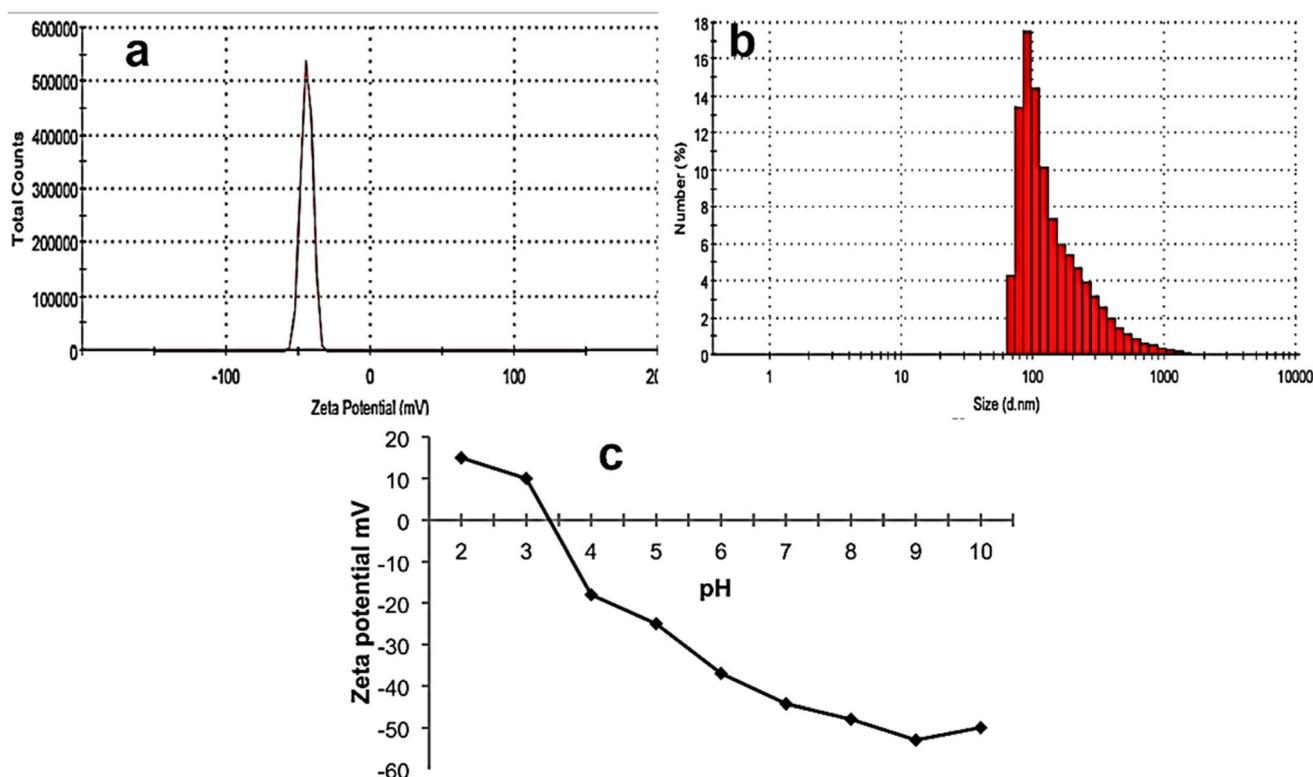
nanoparticles, which is generally influenced by the presence of electronegative atom-containing groups, such as –N<, –OH, –CONH–, and –COOH. An increase in the number of these groups typically results in greater hydration and a larger DLS diameter owing to the extensive hydrogen bonding interactions between water molecules and the surface of the coated MNPs. Another important factor in size measurement is the polydispersity index (PDI). The lower the PDI value (generally less than 0.3 or 30%), the narrower is the size range and uniformity of the particles. The measurement of the surface charge, expressed as zeta potential (ζ), is a critical parameter in DLS analyses. This measurement provides insights into the potential of MNPs to attract ions, thereby elucidating the mechanism of pollutant removal in wastewater. The zeta potential (ZP) is a measure of the electrical double layer or charge of nanoparticles. While performing the ZP study for nanoparticles, different pH conditions, generally in the range of pH 1–12, were used; in general, at pH 7, the surface charges on the MNPs were found to be negative.[135–138] Some phytogen@MNPs have been reported to have positive ZPs below pH 4.[139] Therefore, the point at which the charges of the MNPs become zero, rendering them electrically neutral, is referred to as the point of zero charge (PZC). Below the PZC, the surfaces of the MNPs acquired a positive charge, thereby attracting negatively charged ions.

Conversely, above the PZC, the surface becomes negatively charged, facilitating the adsorption of positively charged ions. The stability of the nanoparticles was determined by ZP analysis. For example, Kovář et al.[140] synthesized superparamagnetic MNPs for magnetic resonance imaging. They showed that the ZP remained constant at approximately −39 mV during the two months; hence, it was reported to be stable. Therefore, it can be concluded that a constant ZP charge signifies an increased stability. In general, NPs are considered stable when they possess a surface charge $\geq \pm 30$.

Nassar et al.[139] in their report used an extract from Citrus reticulata (CR, mandarin) peel during MNP synthesis. The surface modification of MNPs through the functional groups of the mandarin extract yielded a ZP value of −44.3 mV at pH 7, indicating the stability of the synthesized Fe_3O_4 NPs. The ZPs and hydrodynamic sizes are graphically presented in Fig. 4a–c and the PZC was found to be at pH 3.8 (Fig. 4c).

According to them, the tendency of the prepared NPs to repel each other reduced the polydispersity index (PDI = 0.419), which, in turn, increased the long-term stability of the NPs in solution. They suggested that in a basic medium (pH ~11), the deprotonation of the capping biomolecules (e.g., polyphenols, flavonoids, etc.) containing functional groups of the CR-extract was responsible for the significant negative charge on
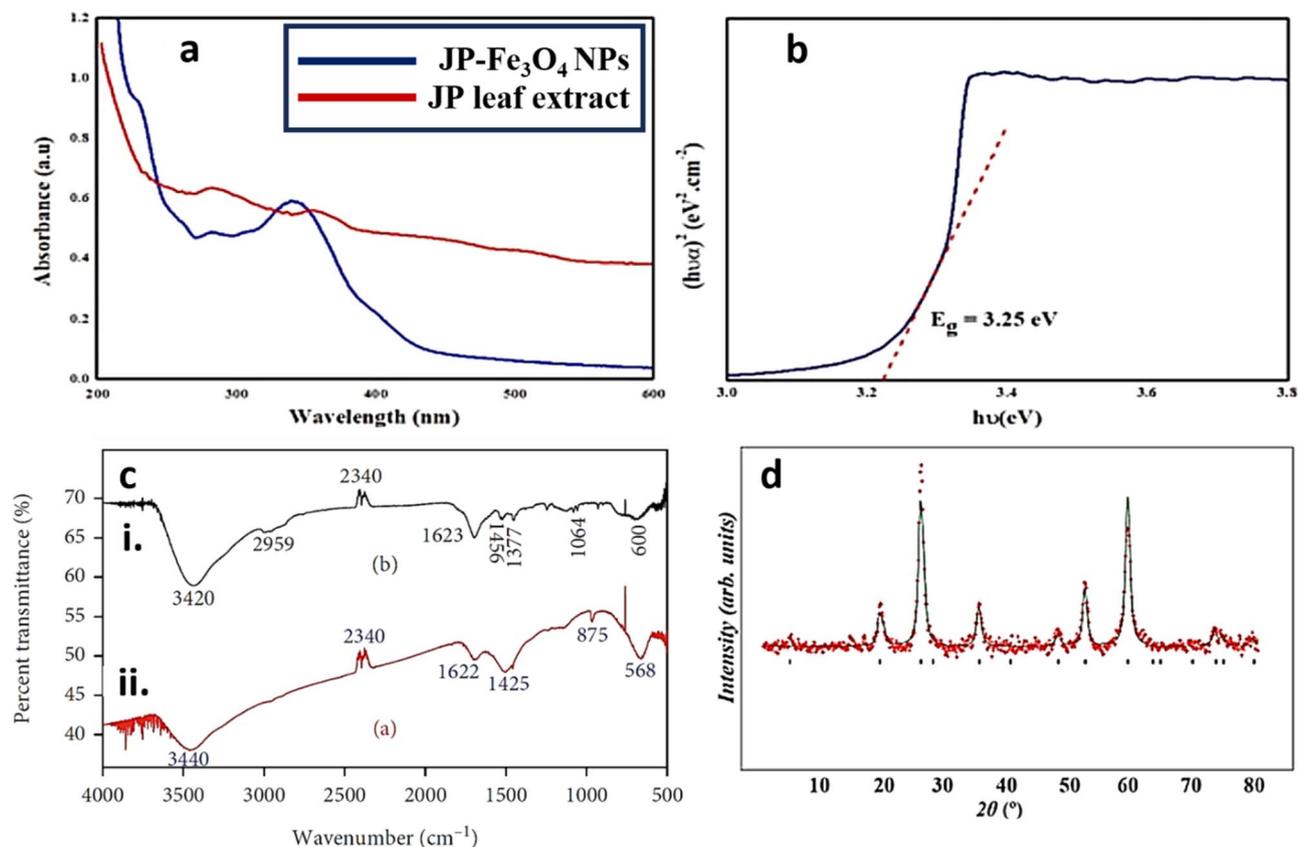
Fig. 5 (a) UV-vis spectra and (b) corresponding Tauc plot for the Fe_3O_4 nanoparticles synthesized using *Jatropha podagrica* leaf extract (source: this image is taken from an article written by Golthi et al.[145]); (c) FTIR spectra of magnetite nanoparticles using *Thymus schimperi* leaf extract (i) after and (ii) before calcination (source: this line is taken from an article written by Geneti et al.[131]); (d) pXRD of MNPs synthesized using the leaf extract of *Azadirachta indica* (source: this image is taken from an article written by Zambri et al.[150]).

phytogen@MNPs. Therefore, the dispersion of positively charged MNPs was stabilized by CR-extracted biomolecules, preventing their aggregation and agglomeration, and thus, their growth and expansion.

Hence, the better stability of the phytogen@MNPs is attributed to the presence of various coordinating groups containing surface coatings and high surface charges.

4.2 UV-vis spectral study and band gap analysis

Ultraviolet-visible spectroscopy was used to examine the absorbance profiles of the MNPs. In the typical UV absorption spectrum of the MNPs, a continuous decrease in absorbance from 300 to 800 nm was observed. Another piece of information obtained from the UV-vis spectra is the bandgap, which is a measure of the energy gap between the conduction and valence bands. Tauc et al.[141,142] applied an expression to determine the optical bandgap of Ge (eqn (4)):

$$(\alpha h\nu)^{1/n} = A\,(h\nu - E_g) \tag{4}$$

where h = Planck's constant, ν = frequency of the photons, E_g = bandgap energy, and A = constant. The n factor is dependent on the type of electron transition and can be $\frac{1}{2}$ or 2 for direct and indirect transition bandgaps, respectively. The bandgap of the synthesized phytogen@MNPs was analyzed using the Tauc equation by plotting $(\alpha h\nu)^{1/n}$ vs. $h\nu$.

The band gap of a semiconductor (MNPs) varies with size. Abdulla et al.[143] conducted a thorough investigation of the relationship between size and band gap. These results suggest that in semiconductors characterized by narrow to moderate band gaps, a reduction in size leads to an increase in the band gap. A similar study was performed by Singh et al.[144] using CdSe, CdTe, ZnS, ZnSe, and ZnTe semiconductor compounds, and they found that the optical band gap varied with the size and shape (i.e., spherical nanospheres, nanowires, and nanofilms) of the materials. According to this theory, the bandgap energy increases as the particle size (diameter or length) of semiconductor nanomaterials decreases.

Golthi et al.[145] used an aqueous leaf extract of Jatropha podagrica (JP) to synthesize JP-Fe$_3$O$_4$ NPs. Fig. 5a shows the UV-vis absorption spectra of the extract and the JP-Fe$_3$O$_4$ NPs. They reported that JP leaf extract exhibited pronounced absorption bands at 280 and 351 nm, attributable to the composition of various phytochemicals, including phenolic acids, tannins,

alkaloids, proanthocyanidins, flavonoids, and glycol flavones. Furthermore, the formation of JP-Fe$_3$O$_4$ NPs was confirmed by the presence of a characteristic absorption band at 341 nm, which was primarily due to the scattering and absorption of light by the nanoparticles. The presence of characteristic peaks from the JP leaf extract at 280 and 351 nm in the JP-Fe$_3$O$_4$ NPs spectra is noteworthy and confirms the capping of leaf extract over NPs. Fig. 5b displays the equivalent Tauc plot, and the value of the direct band gap was 3.25 eV.

From Table 5, it can be concluded that the band gap varies with the type of phytogen present on the phytogen@MNPs. The efficiency of a photocatalytic material is significantly dependent on its optical bandgap. This is because an incoming photon can only cause the electronic state to shift from the valence band to the conduction band if its energy is greater than or equal to the bandgap energy.

4.3 FTIR study

Fourier-transform spectroscopy validated the presence of phytogens on the surface of MNPs. In general, the O–H stretching frequency (from water or coating agents such as polyphenol and eugenol) appeared at 3200–3500 cm^{-1}. In the case of the N–H stretching of amides, it appears in the same range as that of O–H. The carbonyl group appeared at approximately 1600–1700 cm^{-1}. The spectral range of 1600 cm^{-1} corresponds to the C=C stretching vibration, whereas the range of 1400–1500 cm^{-1} is associated with the H–C–H scissoring vibration of the –CH$_2$– group. The range of 1300–1400 cm^{-1} pertains to N–O bending, the 1200–1300 cm^{-1} range is indicative of the C–O asymmetric stretching vibration in cyclic polyphenols, and the 1000–1100 cm^{-1} range corresponds to the C–O stretching vibration.[148] Owing to the presence of polyamides in the phytogen@MNPs, the N–H stretching frequency for 2° amines appeared at 2800–2900 cm^{-1}, which is in the same range as the C–H stretching of the alkyl groups. For MNPs, the Fe–O stretching frequency appears at approximately 400–600 cm^{-1}, which includes tetrahedral and octahedral Fe–O sites.[149] Based on FTIR analysis, it can be inferred which types of molecules containing coordinating groups may be present on the surface of the MNPs.

Geneti et al.[131] synthesized MNPs using the leaf extract of Thymus schimperi and recorded the FT-IR spectrum of the calcined NPs, as shown in Fig. 5c(i). Significant absorption bands were identified at 3440 cm^{-1} (O–H stretching),

Table 5 Variation in bandgap values for different phytogenic coatings on MNPs

Nanoparticles	Direct band-gap (E_g, eV)	References
Bare MNPs	2.00	129
Nigella sativa seed extract (aq. alc.)@MNPs	2.74	
Artemisia herba-alba (ARM)@MNPs	2.87	146
Rosemarinus officinalis (ROS)@MNPs	2.95	
Matricaria Pubescens (MAT)@MNPs	2.96	
Juniperus phoenicea (JUN)@MNPs	2.97	
Murraya paniculata (L) Jack flower extract (aq.)@MNPs	2.57	24
Caralluma acutangulla leaf extract (aq.)@MNPs	1.94	147

1622 cm^{-1} (N–H bending of amide), 1425 cm^{-1} (>CH$_2$< bending), 875 cm^{-1} (C–H bending), and 568 cm^{-1} (Fe–O stretching). In contrast, Fig. 5c(ii) shows the FTIR spectra of the uncalcined nanoparticles, with absorption bands observed at 3420 cm^{-1} (O–H stretching), 2959 cm^{-1} (>CH$_2$< stretching), 1623 cm^{-1} (N–H bending of amide), 1456 cm^{-1} (>CH$_2$< stretching), 1377 cm^{-1} (O–H bending), 1064 cm^{-1} (C–N stretching), and 600 cm^{-1} (Fe–O stretching of Fe$_3$O$_4$). According to them, phytochemicals such as thymol and carvacrol were present in the extract; hence, O–H stretching vibration was observed, and the presence of H$_2$O molecules may also contribute to its appearance.

4.4 Powdered X-ray diffractometry study

Powdered X-ray diffraction data generally provide information on the crystallinity and crystal size. The functionalized MNPs with a different surface coating with the same NP core had similar XRD patterns. For example, Bouafia et al.[151] synthesized
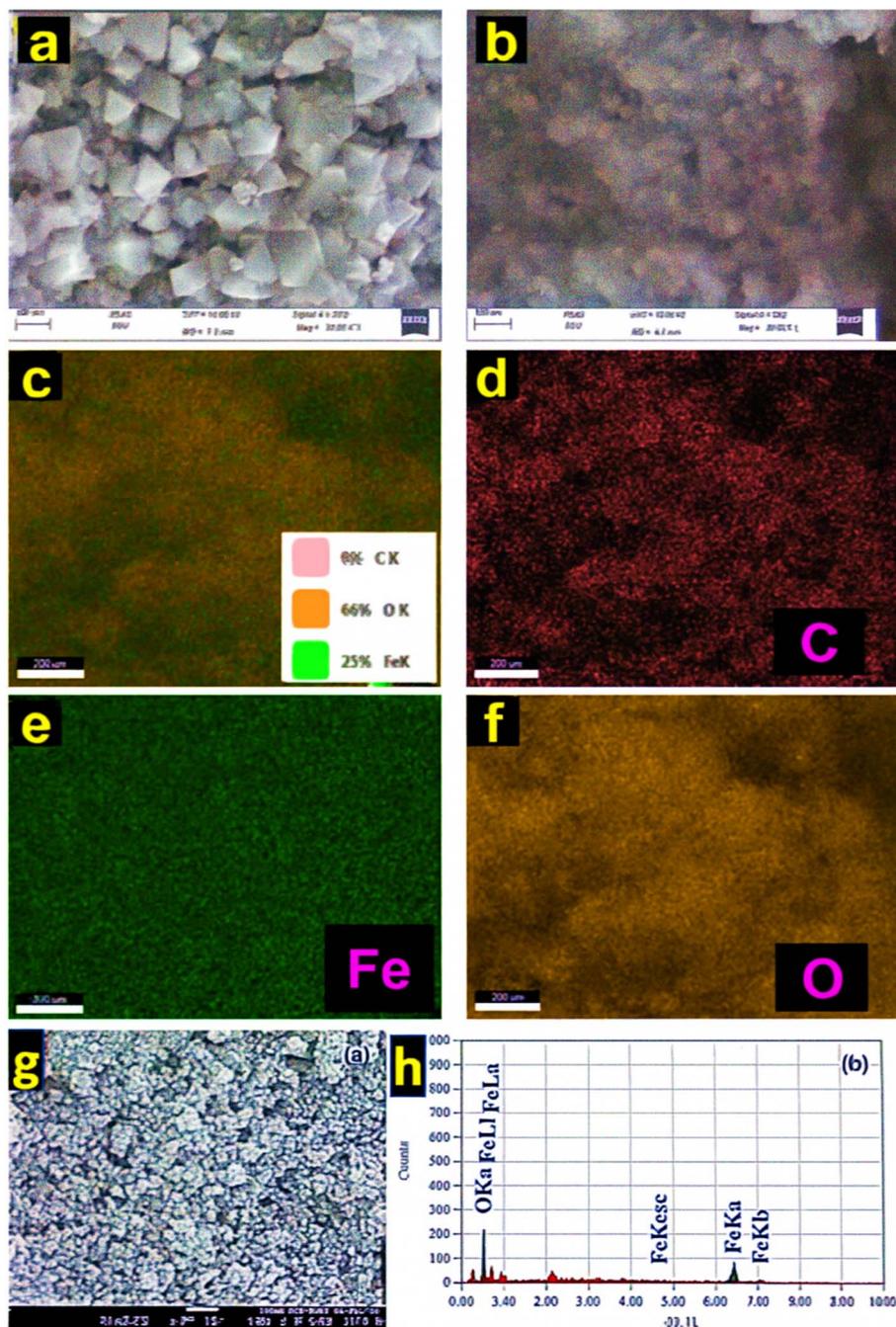
Fig. 6 (a and b) FESEM and (c–f) EDS color mapping analysis of the green-synthesized MNPs using green coffee (source: this image is taken from an article written by Dhar et al.[152]). A typical (g) SEM image and (h) EDS spectrum of MNPs obtained by green synthesis using *Lathyrus sativus* peel extract (source: this image is taken from an article written by Mohamed et al.[153]).

MNPs using an extract from the leaves of *Artemisia* L., employing a 10 : 1 volume ratio of Fe(III) chloride (0.1, 0.01, 0.04, and 0.07 M) to the leaf extract. The XRD patterns of both the synthesized and annealed MNPs (at 500 °C) exhibited sharp and narrow peaks, indicative of their fine particle nature and small crystallite size. Six distinct diffraction peaks were observed at 2θ values of 30.25°, 35.45°, 43.20°, 53.39°, 57.26°, and 62.90°, corresponding to the (220), (311), (400), (422), (511), and (440) crystallographic planes of the *Artemisia* L@MNPs phase. These reflections are consistent with the cubic structure of magnetite (space group: *Fd-3m*), indexed to Joint Committee on Powder Diffraction Standards (JCPDS) Card No. 01-075-0449. A progressive increase in peak intensity was observed with increasing ferric chloride concentration, suggesting enhanced crystallinity and a promotion effect on the degree of crystallization. The average crystallite size calculated using the Debye–Scherrer equation ranged from 24.67 to 34.28 nm.

After synthesizing MNPs using *Azadirachta indica* leaf extract, Zambri *et al.*[150] observed an XRD pattern that revealed six distinct Fe_3O_4 diffraction peaks. With the *Fd3ms* space group, the sample was indexed to a single-phase cubic structure, and all the diffraction peaks agreed well with JCPDS file No. 19-0629. Using Rietveld refinement, the lattice parameters were determined to be $a = b = c = 8.3559$ Å, and the unit cell
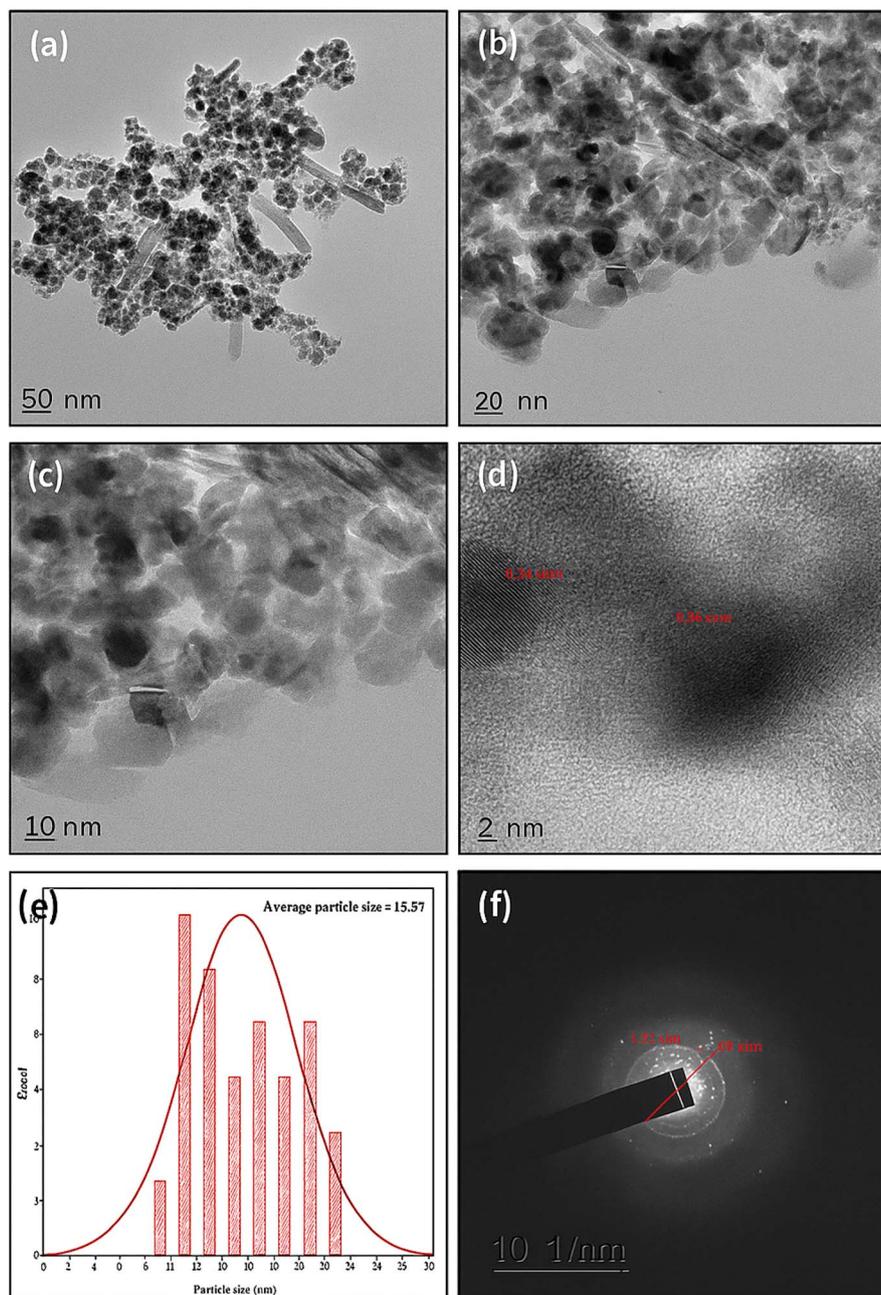
Fig. 7   (a–d) HRTEM images under resolutions of 50, 20, 10, and 2 nm, respectively; (e) histogram of size analysis; and (f) SAED pattern for the *Jatropha podagrica*-leaf extract synthesized MNPs (source: this image is taken from an article written by Golthi *et al.*[145]).

volume was 583.42 Å^3.[150] The structural planes of Fe_3O_4 and the Rietveld refinement of the XRD patterns are shown in Fig. 5d. The Debye–Scherrer equation, expressed as $D = (0.94\lambda)/(\beta \cos \theta)$, was employed to determine the average crystallographic size (D), where λ represents the X-ray wavelength, β denotes the broadening of the peak at half maximum, and the calculated average size was 9.48 nm.

4.5 FESEM study

Field emission scanning electron microscopy (FE-SEM) is usually used to determine the morphology of NPs, that is, their shape. FESEM usually provides an idea of whether the NPs are surrounded by some type of coating agent or not. In addition to FESEM, energy dispersive spectroscopy can be used to reveal the possible elements present on the coated NPs. Energy Dispersive Spectroscopy (EDS)-elemental mapping, another version of EDS, allows for the colorful mapping of each possible element.

Mohamed et al.[152] synthesized MNPs using green coffee and reported FESEM images (Fig. 6a and b) along with EDS color mapping (Fig. 6c–f) and found strong evidence for the formation of MNPs coated with green coffee containing molecules. The color mapping images clearly indicate that the NPs contained 25% Fe, 9% C, and 66% O.

The morphology of Lathyrus sativus peel extract-based MNPs, which were irregularly shaped and aggregated, was observed by Dhar et al.[153] (Fig. 6g). They speculated that this could be due to the interaction between the phytochemicals and Fe_3O_4-NPs, as discussed in their study. They stated that agglomeration could be caused by the steric effect attributed to the interaction between the MNPs' magnetic nature and their active sites. Fig. 6h shows the elemental composition of MNPs. Both elemental oxygen and iron were confirmed by the high peak at 6.398 keV and sharp peak at 0.525 keV in the EDS spectrum. Therefore, the unique Fe and oxygen peaks in the EDS image (Fig. 6h) indicate that the Fe_3O_4-NPs were formed via an eco-friendly and sustainable route.

4.6 HRTEM study

High-resolution transmission electron microscopy (HRTEM) was employed to determine the morphology and size of phytogen@MNPs. HRTEM image analysis confirmed their shape and provided insights into the presence of the coating material. Furthermore, the selected area electron diffraction (SAED) pattern obtained from HRTEM revealed the crystalline nature of the phytogen@MNPs, supporting the findings of the powder XRD analysis.

Golthi et al.[145] analyzed the size and morphology of Jatropha podagrica-leaf extract synthesized MNPs using TEM and found

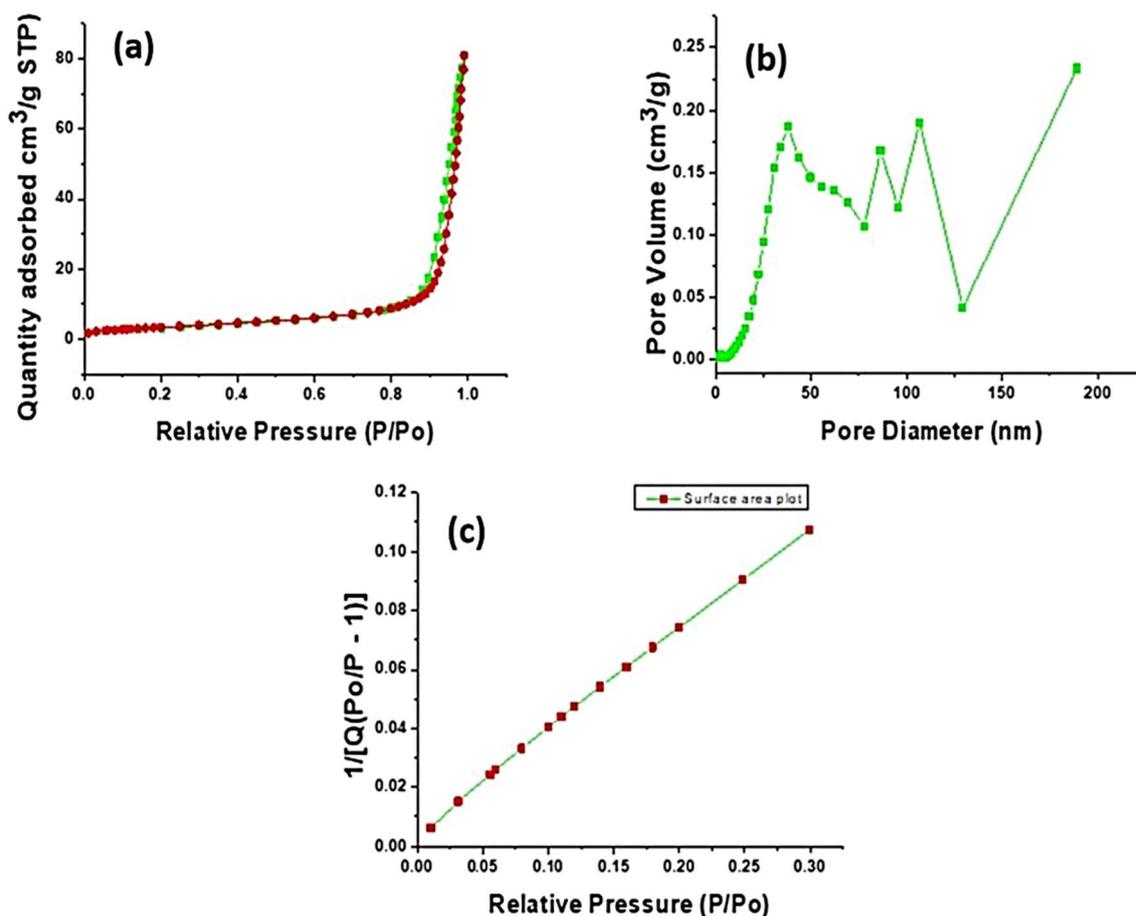
Fig. 8 (a) Adsorption–desorption isotherm, (b) pore size, and (c) surface area plot for the M. burkeana extract mediated Fe_3O_4 NPs (source: this image is taken from an article written by Mahlaule-Glory et al.[155]).

that the nanoparticles were irregularly shaped (Fig. 7a–d). According to their findings, most of the particles were agglomerated and had an average size of 15.57 nm (Fig. 7e). According to their findings, the crystal planes obtained from SAED results (Fig. 7f) resembled the XRD patterns for MNPs, which supported the XRD data.

4.7 Surface area analysis *via* the Brunauer–Emmett–Teller method

The Brunauer–Emmett–Teller (BET) method was used to determine the specific surface areas of the obtained materials, which depended on the synthesis method. The nitrogen physisorption isotherms and pore size distribution of each NM were used to determine its surface area. According to the International Union of Pure and Applied Chemistry (IUPAC) classification, nanocrystalline Fe_3O_4 can be microporous, mesoporous, or macroporous with pore sizes of <2, 2–50, or >50 nm.[154]

Mahlaule-Glory *et al.*[155] synthesized MNPs using *M. burkeana* extract and used them for the degradation of the sulfisoxazole antibiotic, methylene blue dye (MB), and the removal of microorganisms from real water. They performed BET analysis (Fig. 8a–c) to obtain information regarding the surface properties, such as surface area, pore volume, and size of the green-synthesized Fe_3O_4 NPs. They obtained a surface area of 12.83 $m^2 g^{-1}$, with a pore size of 35.67 nm, which falls within the range of 2–50 nm, implying that the sorbent is mesoporous. These data clearly indicate that MNPs can be used as photocatalysts for the degradation of various contaminants in wastewater.

4.8 TGA study

Thermogravimetric analysis (TGA) was used to measure the thermal stability and percentage of coating on the NP surface. In general, surface-coated MNPs were heated at 25–900 °C under a 10 °C min⁻¹ heat flow in an inert environment. Generally, in TGA, we obtained only a one-step weight loss, but in the case of phytogen@MNPs, only two or three weight loss steps were observed. The first step of weight loss generally occurs because of the evaporation of water or adsorbed ions, such as hydroxyl groups. In the following step, the coating begins to degrade, and the surfaces are exposed, which remain stable even at high temperatures (900 °C). Sometimes, coating materials can have very good coordinating groups, and thus the coated MNPs become thermally stable.

Das *et al.*[54] synthesized MNPs from aqueous *Terminalia arjuna* bark extract, which was characterized using various techniques, including TGA, and used to remove Pb(II) and MB. The experiment was performed in the temperature range of 25–900 °C at a rate of 20 °C min⁻¹, and three stages of degradation were observed (Fig. 9a). In the first stage (12.6%, <180 °C), H_2O, OH^-, *etc.* and weakly adsorbed volatile impurities left the surface. In the second stage (26.6%, 180–500 °C), degradation of phytogen occurred from the surface. In the third phase of degradation (4.1%, 500–900 °C), complete removal of the
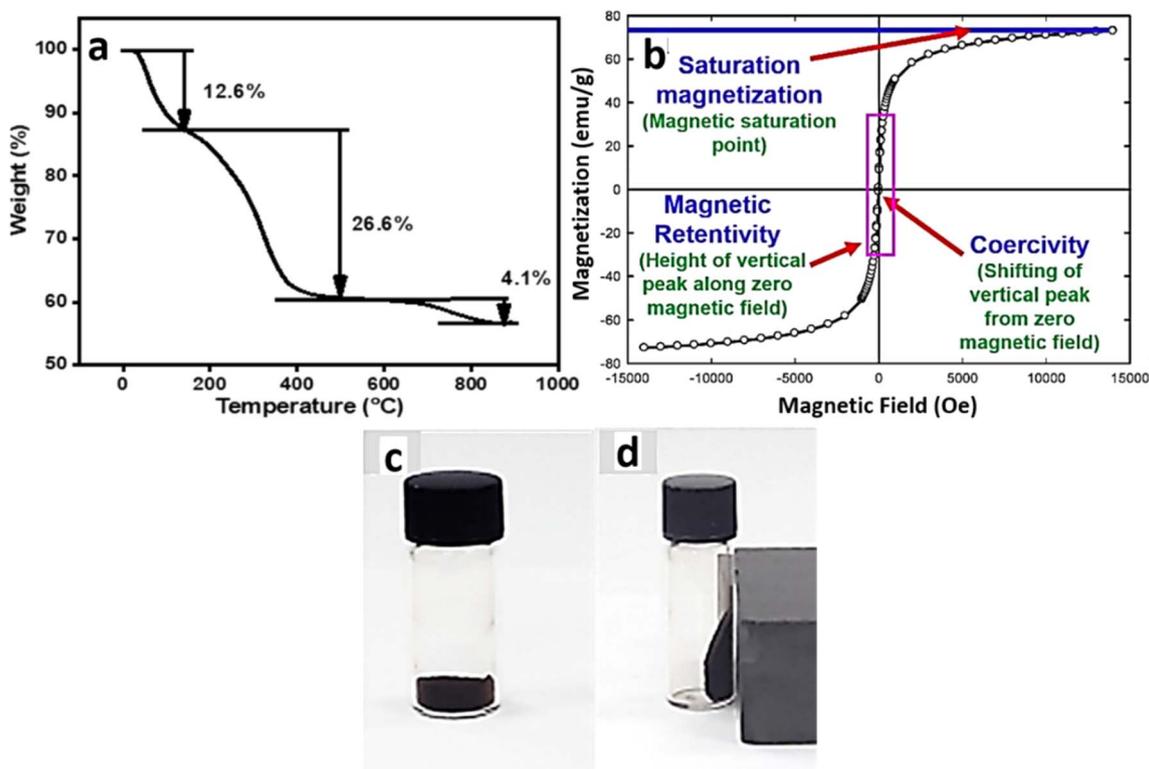

Fig. 9 (a) TGA analysis of *T. arjuna* bark extract (aq.) coated MNPs (source: this image is taken from an article written by Das *et al.*[54]); analysis of *Azadirachta indica* leaf extract-mediated MNPs: (b) VSM analysis, (c) before and (d) after magnetic separation (source: this image is taken from an article written by Zambri *et al.*[150]).

surface coating occurred. Based on these results, the surface of the synthesized MNPs had a coverage of approximately 43.3%.

4.9 Magnetic measurement study

Magnetic measurements were obtained by analyzing the samples using VSM or AGM. In standard magnetic measurements, when the coercivity approaches zero, the curve exhibits an absence of a hysteresis loop, thereby indicating a super-paramagnetic nature. The applicability of a material increases with its magnetic moment, specifically its saturation magnetization value. The magnetic moment of MNPs depends on the type of coating material present on the surface and the size of the MNPs. The larger the size of the MNPs, the greater the magnetic moment.[156] In brief, as the particle size decreased,

Table 6 Different characterization techniques used for various nanoparticles

Techniques	Information
DLS	Size distribution is determined by measuring laser light scattering through a colloidal solution (PDI), indicating nanosized particle formation through hydrodynamic analysis
ZP measurement	It determines the surface charge, stability of colloidal suspensions, and isoelectric point. The stability of the NPs is enhanced by increased electrostatic repulsion, as indicated by larger magnitude potentials
UV-vis spectroscopy	Detection of optical properties based on size, shape, concentration and agglomeration. The instrument allows precise measurement of solution concentrations including adsorbate, adsorbent, and post-treatment samples through absorbance analysis, and is also employed to estimate the band gap of semiconducting nanomaterials
Photoluminescence (PL) spectroscopy	Optical properties can be monitored by this technique. PL spectroscopy investigates biomaterial changes, characterizes nanoparticle conjugation, and assesses encapsulation efficiency and release mechanisms
Time resolved fluorescence (TRF) spectroscopy	Measures the decay of fluorescence over time after excitation
Cathodoluminescence (CL)	Optical properties can be observed from this technique. It is an emission spectroscopy that measures the light emission spectrum under free electrons
pXRD	It monitors crystal structure, composition, oxidation states, electronic structure, grain size, particle size, defects, and growth kinetics
FTIR, NIR	It shows functional groups (polymeric, organic, and inorganic materials) present on the surface and molecular interactions between medicines and encapsulating MNPs, which are crucial for tailoring properties and performance in drug delivery systems
Raman spectroscopy	It is a powerful and non-destructive tool for characterizing the density of defects and assessing the structural evolution of NPs, including the degree of graphitization
Electron microscopy (TEM, SEM, AFM, STEM)	TEM and SEM help to determine purity and exfoliation of material bundles along with size, morphology, crystal structure, dispersion of MNPs, and elemental composition. AFM provides 3D shape and surface evaluation
SAED	Crystal structure, diffraction pattern, and orientation can be determined
Energy-dispersive X-ray spectroscopy (EDX or EDS) or its mapping analysis	It measures elemental composition and colored mapping of different elements
X-ray photoelectron spectroscopy (XPS)	It is used to study the surface of a material, elemental composition, and oxidation states
CHNS analysis	It determines the percentage of carbon, hydrogen, nitrogen, and sulfur
Differential scanning calorimetry (DSC)/TGA	Compositional purity and thermal stability can be determined
BET surface area analysis	It measures the surface area, porosity, and density. Pore volume and pore size can also be determined
Magnetic moment measurements (VSM, AGM, SQUID)	They establish the magnetic nature and determine the magnetic moment. SQUID is the most sensitive, and VSM is the least sensitive technique, while AGM lies in between them
Atomic emission spectroscopy (AES)	Elemental composition can be measured from this technique
Inductively coupled plasma-mass spectrometry (ICP-MS)	It can determine the size, size distribution, and NP concentration, and it identifies and quantifies the elemental composition of samples
Static laser light scattering (SLS)	It measures and detects particle sizes ranging from nm to mm, and distributions. It also measures the angular variation of light scattering used to indicate particle size
Grazing incidence small-angle X-ray scattering (GISAXS)	It gives information about the structure, morphology, correlations, and mutual orientation
Four-point-probe resistivity measurement	Provides quantitative data of conductive properties

the number of magnetic dipoles also decreased. The interactions between the magnetic moments result in the internal coupling of magnetic resistance, which is subsequently reduced by these dipoles.[157] For example, bare MNPs had a saturation magnetization value (M_s) of 70 emu g^{-1}, whereas when *Cinnamomum tamala* leaf extract (aq.) containing molecules were present on the surface, a significant reduction in M_s occurred, which was found to be 33.8 emu g^{-1}.[148]

Zambri *et al.*[150] synthesized MNPs with the help of *Azadirachta indica* leaf extract and recorded the magnetic moment by a VSM study; the results are shown in Fig. 9b. The absence of a hysteresis loop in their results suggests a superparamagnetic behavior. The maximum saturation magnetization (M_s) of the synthesized MNPs was 73.040 emu g^{-1}, which was lower than that of the bare MNPs ($M_s = 92$ emu g^{-1}), most likely because of the disordered spin layer on their surfaces. According to their findings, a decrease in the size of the resultant particles significantly increases the ratio of the disordered layer to the radius of the MNPs. Consequently, this surface spin disorder contributed to the reduced M_s of smaller nanoparticles. Therefore, M_s was enhanced by increasing the crystallite size of the magnetic particles. It has been reported that M_s values of 7–22 emu g^{-1} are suitable for biomedical applications. They also showed the behavior of Fe_3O_4 nanoparticles before and after the application of an external magnetic field, as shown in Fig. 9c and d.

Table 6 summarizes the information obtained from the characterization techniques and provides additional details.

In conclusion, it can be stated that the performance of the synthesized MNPs in pollutant removal is linked to their physicochemical characteristics, particularly particle size, surface area, and surface functionalization. The nanoscale dimensions provide a high surface-to-volume ratio and abundant active sites, enhancing the adsorption of heavy metals, dyes, and pharmaceutical residues. A controlled size distribution is essential for achieving superparamagnetism, which allows magnetic recovery from complex aqueous matrices. Surface modification using phytogenic functional groups improves the colloidal stability, prevents aggregation, and introduces binding sites that promote selective interactions with contaminants. These surface moieties enable strong chemisorption of metal ions and facilitate catalytic pathways for generating ROS, which are essential for the photocatalytic degradation of organic pollutants. The structural and surface attributes of MNPs directly influence their adsorption capacity, degradation kinetics, and recyclability, highlighting the need for rational design to maximize environmental remediation efficiency.

5. Removal of wastewater contaminants

5.1 Wastewater containing contaminants: a deep insight

Organic pollutants in wastewater include dyes, humic substances, phenolic compounds, petroleum, surfactants, pesticides, microplastics, polyfluoro/chloro alkyl/arenes, and pharmaceutical organic compounds.[158] Organic contaminants in water can produce harmful compounds during disinfection. According to an estimate, on average, approximately 11 000 micro- and nanoplastics are ingested annually by every person through seafood.[159] Exposure to microplastics in humans can result in oxidative stress, cytotoxicity, neurotoxicity, disruption of the immune system, and translocation to other tissues.[160] Aquatic organisms in stream ecosystems may experience both acute and chronic adverse effects such as behavioral changes, tissue accumulation of contaminants, reproductive impairments, and inhibited cellular proliferation resulting from prolonged exposure to low concentrations of complex pharmaceutical wastes. They can also cause carcinogenicity, neurotoxicity, and developmental toxicity.[161]

Inorganic pollutants that can be harmful to humans include metallic (mostly heavy metals) and non-metallic ions such as $Hg(II)$, $Cu(II)$, $Pb(II)$, $U(VI)$, $Cd(II)$, $As(V/VIVI)$, $Cr(VI)$, NO_3^-, PO_4^{3-}, SO_4^{2-}, F^-, Cl^-, and $C_2O_4^{2-}$.[162] These pollutants lead to environmental disruption, adversely affect aquatic life and wildlife, and pose several health risks to humans, including kidney and liver damage, as well as an increased risk of cancer.[163,164] Previous studies have reported the impact of heavy metals on cellular organelles and various biological systems. These include the cell membrane, lysosomes, mitochondria, nuclei, endoplasmic reticulum, and several enzymes involved in detoxification, metabolism, and damage repair. It has been reported that metal ions interact with DNA and nuclear proteins within cells, resulting in DNA damage and conformational changes that may influence cell apoptosis, cell cycle progression, or carcinogenesis.[165,166]

Among the harmful microorganisms, *Escherichia coli* (*E. coli*), *Staphylococcus aureus* (*S. aureus*), *Vibrio cholerae*, *Shigella dysenteriae*, *Vibrio parahaemolyticus*, *Cryptosporidium*, *Campylobacter*, *Enterovirus*, *Giardia*, *and Rotavirus* are most commonly found in water.[167] These microorganisms can cause several health problems, such as diarrhea, stomach cramps, fever, vomiting, cough, runny nose, skin rashes, upset stomach, yellow skin or eyes, abdominal pain, and shortness of breath. Some infections manifest in a way that can even result in death; for example, according to an estimate by the World Health Organization (WHO), approximately 485 000 diarrheal deaths occur each year due to contaminated drinking water.

5.2 Magnetite nanoparticles towards wastewater purification *via* adsorption and degradation

Owing to the presence of these contaminants, the future demand for potable water is unlikely to be met, and nearly all water sources are rendered unsuitable for consumption. Different methods have been used to remove various organic and inorganic pollutants from wastewater, such as membrane filtration (nanofiltration, distillation, ultrafiltration, and microfiltration), adsorption, chemical, electric, photocatalytic, chemical transformation, coagulation, flocculation, and biological treatments. Among the available techniques, photocatalytic degradation and adsorption are the two most efficient, simple, and environmentally friendly processes for cleaning

contaminated water.[168,169] Photocatalytic removal of various organic substances and inorganic ions by NPs can occur *via* the formation of several ROS, such as singlet oxygen (O_2^1), hydroxyl radicals (OH·), superoxide ions (O_2^-), hydrogen peroxide (H_2O_2), electrons (e^-), and holes (h^+). ROS, e, and h^+ can oxidize or reduce organic and inorganic pollutants to form CO_2, H_2O, and other non-toxic forms of pollutants. Conversely, adsorption pertains to the interaction between the adsorbent, which consists of pollutants, and the adsorbate, represented by the NPs. This interaction can manifest as either a surface phenomenon, known as physisorption, or a whole-body phenomenon, known as chemisorption, involving NPs. In both processes, NPs can be reused several times, thereby making the process cheaper, which is another advantage of the photocatalytic degradation and adsorption techniques.

5.2.1 Adsorption and photocatalytic degradation of pollutants in wastewater: pros and cons. Reverse osmosis (RO) is considered one of the most sophisticated techniques for purifying water; however, it is expensive and energy-intensive.[170] Osmosis makes water acidic and does not remove volatile organic compounds or pharmaceuticals.

Adsorption is a water purification method that removes dissolved impurities by adhering substances from liquids or gases to the interface between two phases. It is a low-cost and effective method for removing inorganic pollutants, synthetic dyes, and organic pollutants from polluted waters.[171] Adsorption can remove several metallic and non-metallic ions/compounds:

• Many types of pesticides and other synthetic organic chemicals.

• Heavy metals like lead, cadmium, uranium, copper, *etc.*

• Synthetic dyes.

• Pharmaceutical molecules.

• Other organic pollutants like phenols, nitrobenzene *etc.*

Adsorption has several advantages over other methods, including a simple design, low investment in terms of the initial cost and area required, and the ability to remove almost all types of pollutants from water. The adsorption process is extensively used for treating industrial wastewater containing organic and inorganic pollutants and has attracted considerable attention from researchers. In recent years, the search for cost-effective adsorbents with pollutant-binding capacities has gained popularity. Eco-friendly and renewable materials, such as natural materials, industrial waste, and agricultural waste, are now used as cost-effective adsorbents. Activated carbon prepared from these materials can be used as an adsorbent for water and wastewater treatment. Various metals, metal oxides, metal sulfides, and nanoparticles have been used for adsorptive removal of contaminants from water. MNPs are highly suitable for application as adsorbents when optimally coated.

Although adsorption is a convenient and successful technique for removing pollutants, it has several limitations, such as high complexity, excessive use of reagents, high operational costs, and stability of adsorbents over time.[172] For example, Bankole *et al.*[173] reported that commercial activated carbons are good adsorbents, but their limitation is their high cost. Agglomeration, sludge production, and slowness are other disadvantages of the adsorption techniques.[174]

Photocatalysis is an important green method for decontamination and detoxification of aquatic environments because its functionality remains consistent regardless of temperature for almost all types of organic contaminants. It has several applications, including CO_2 reduction, organic contaminant degradation, toxic and heavy metal ion removal, water splitting, bacterial eradication, and self-cleaning.[175] Therefore, the development and design of innovative photocatalyst-semiconductors, specifically heterogeneous magnetic materials, have attracted significant attention. They are simple to use, have low toxicity, are easily separable, and consume significantly less energy during operation. According to Liu *et al.*,[176] a magnetite-carbon nanofiber composite (Fe_3O_4-NPs@CNF) may be an effective choice for reducing carbamazepine pollution. However, the complex synthetic procedures and high-temperature requirements render this material expensive. Lotfi *et al.*[177] used a polysulfone membrane covered with TiO_2 to degrade four steroid hormones in wastewater. The high cost, high temperature, and use of dangerous materials are the major drawbacks in these cases. Shi *et al.*[178] removed acetaminophen using a combination of magnetite nanoparticle-modified cyclodextrin and potassium permanganate; however, the oxidizing agent used and the procedure involved were complex. Awwad *et al.*[179] synthesized carbon-doped ceria-NPs for the degradation of cortisone acetate. The two major issues are lengthy processes and high energy consumption. In addition, Jimenez-Salcedo *et al.*[180] proposed that graphitic carbon nitride nanosheets can efficiently degrade sodium diclofenac; however, they used high temperatures and complicated separation procedures.

To purify wastewater, safer nanoparticles should be used to ensure the safety of both aquatic and land uses. Various types of chemically coated nanoparticles have been previously reported. Chemical modification is also a method to stabilize MNPs and endow them with multifunctionality; however, owing to the high production temperature, high cost, and material toxicity, this process is less frequently used. A schematic representation
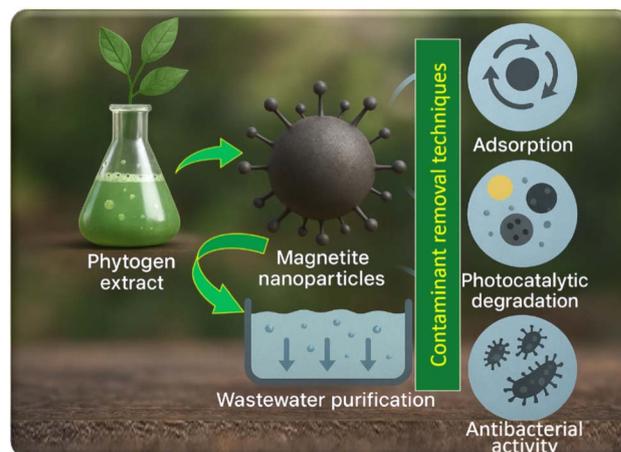

Fig. 10 Pictorial illustration of the use of phytogen@MNPs in wastewater treatment.

of the use of phytogen@MNPs for wastewater treatment is shown in Fig. 10.

5.3 Organic and inorganic contaminant removal through adsorption

5.3.1 Kinetics of the adsorption process. The adsorption mechanism and uptake rates of inorganic and organic ions and neutral species were elucidated using kinetic analysis. Generally, in kinetic studies, adsorptive removal occurs rapidly, and the removal mechanism plays a crucial role. To investigate the kinetics, a constant ratio of adsorbate to adsorbent was maintained, and the mixture was agitated until equilibrium was achieved. During the study, the MNPs were magnetically separated, and the solution was monitored using UV-vis spectroscopy at the λ_{max} of the adsorbate. An illustration of the adsorption of wastewater contaminants onto the phytogen@MNPs is presented in Fig. 11.

The entire process was performed over a fixed time interval of a few minutes to hours until equilibrium was reached. The same study was performed by varying the pH and concentrations of adsorbates and adsorbents. Four linear kinetic models were used (eqn (5)–(8)):

Pseudo-first-order:

$$\ln(Q_e - Q_t) = \ln Q_e - k_1 t \tag{5}$$

Pseudo-second-order:

$$\frac{t}{Q_t} = \left(1/\left(k_2 Q_e^2\right)\right) + \frac{t}{Q_e} \tag{6}$$

Elovich kinetic model:

$$Q_t = \frac{1}{\beta}\ln(\alpha\beta) + \frac{1}{\beta}\ln t \tag{7}$$

Intra-particle diffusion:

$$Q_t = k_p t^{1/2} + X \tag{8}$$

where k_1, k_2, and k_p are rate constants of pseudo-first-order, pseudo-second-order, and intraparticle diffusion, respectively; Q_t is the adsorption capacity after a certain time t (in mg g^{-1}), which is the amount of adsorbate (in mg) on a particular amount of adsorbent (in g); α is the Elovich sorption rate constant; β is the Elovich constant, which corresponds to the extent of surface coverage; and X is a constant of integration.

The adsorption capacity (Q_t, mg g^{-1}) was calculated using the equation (eqn (9)):

$$Q_t = \frac{(C_0 - C_t)V}{m} \tag{9}$$

where C_0 and C_t are the initial and final (after adsorption) concentrations at time t, respectively, and V and m are the volumes of the solution and mass of the adsorbent, respectively. To determine the equilibrium adsorption capacity (Q_e), concentration at equilibrium (C_e) was used instead of C_t. When the kinetic process follows a pseudo-second-order model, it can be inferred that the process involves chemisorption. This phenomenon is attributable solely to the two components present in the solution mixture: the adsorbent and adsorbate. This is analogous to the rate of a chemical reaction, which is characterized by electron exchange between the adsorbate and the adsorbent.[181] The intra-particle diffusion constant indicates that the greater the value of this constant, the greater the mass transfer between the phases.[182]

For instance, Fato et al.[183] removed Pb(II), Cd(II), and Cu(II) from river water using ultrafine mesoporous magnetite nanoparticles synthesized using simple co-precipitation techniques. These MNPs were 4–17 nm in size and could efficiently remove
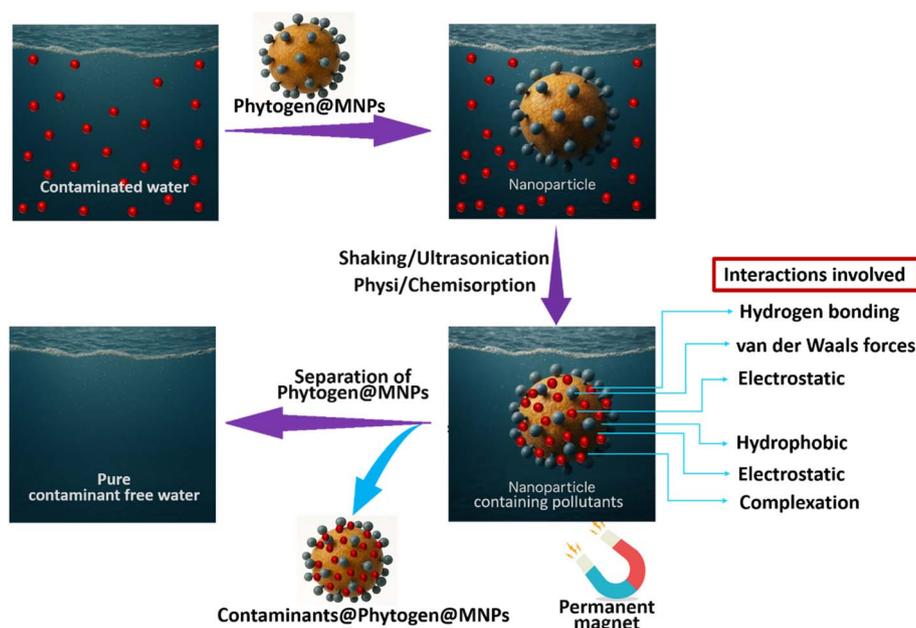

Fig. 11 Pictorial representation of the adsorption technique for phytogen@MNPs.

these ions from water. The authors reported that a pseudo-second-order kinetic model was followed for both single and competitive adsorption processes. According to them, in the case of single adsorption, R^2 for the pseudo-second-order model was >0.99 in every case, and the theoretical adsorption capacities [q_e (cal) = 25.06 (for Pb(II)), 21.88 (for Cd(II)), and 22.99 (for Cu(II)) mg g^{-1}] matched well with the experimental values [q_e (exp) = 24.4 (for Pb(II)), 21.64 (for Cd(II)), and 22.38 (for Cu(II)) mg g^{-1}]. Because the R^2 in every case was very close to unity and the calculated adsorption capacity matched well with the experimental one, they concluded that the sorption process obeyed pseudo-second-order kinetics and not pseudo-first-order kinetics. Andelescu et al.[184] used magnetite/carbon nanocomposites to remove Cu(II), Cd(II), and Zn(II) from water using a batch adsorption method. According to their findings, the adsorption mechanism was not fully described by the pseudo-first-order [R^2 = 0.84–0.98 including all concentrations of Cu(II), Cd(II), and Zn(II)] and Elovich [R^2 = 0.77–0.95 including all concentrations of Cu(II), Cd(II), and Zn(II)] equations (eqn (5) and (7)), as indicated by their weaker correlation coefficients (R^2). This indicates that chemical adsorption was the predominant controlling mechanism and that the process was fast. The pseudo-second-order [R^2 = 0.993–0.999 for all concentrations of Cu(II), Cd(II), and Zn(II)] equation (eqn (6)) yielded the highest correlation coefficients, indicating that it was the most compatible with the experimental results. In addition, the experimentally obtained equilibrium adsorption capacity values [q_e (exp)] using the pseudo-second-order model coincided with the calculated values [q_e (calc)].[184] The possibility of intraparticle diffusion was investigated using the intraparticle diffusion model represented by the Weber and Morris equation (eqn (8)). The plots were examined for all metal ions and depicted in two stages: the external surface adsorption stage in the first step and the closeness to the equilibrium stage in the second step. The fact that the plot did not pass through the origin suggests that intra-particle diffusion was not the limiting step in the adsorption of Cu(II), Cd(II), and Zn(II).

5.3.2 Isotherm study for adsorption. An isotherm study of the adsorption process can elucidate whether the process occurs in a multilayer or a single layer and whether it involves physisorption or chemisorption. Distinct equilibrium adsorption capacities were obtained by varying the adsorbate concentration. When these capacities were applied to the five linear isotherm models (eqn (10) and (12)–(15)), a comprehensive understanding of the general adsorption mechanism was concluded.

Langmuir isotherm:

$$\frac{C_e}{Q_e} = \frac{1}{K_L Q_m} + \frac{C_e}{Q_m} \tag{10}$$

where C_e (mg L^{-1}) and Q_e (mg g^{-1}) are equilibrium concentration and adsorption capacity, respectively, and Q_m is the maximum adsorption capacity (mg g^{-1}).

K_L is the Langmuir isotherm constant (in L mg^{-1}) related to the separation factor (R_L), which provides information about the favorability of the isotherm model, such as (eqn (11)),

$$R_L = \frac{1}{1 + K_L \; C_0} \tag{11}$$

R_L predicts the favorability ($0 < R_L < 1$), unfavourability ($R_L > 1$), irreversibility ($R_L = 0$), or linearity ($R_L = 1$), regardless of the adsorption process.[185] From the Langmuir adsorption model, the maximum adsorption capacity was obtained, which is a measure of the maximum possible amount of adsorbate that can be adsorbed onto the surface of the adsorbent. The linear isotherm model represents the partitioning of adsorbates between solid and liquid phases, involving van der Waals, electrostatic, and hydrophobic interactions. This indicates monolayer adsorption at low initial concentrations.

Freundlich isotherm:

$$\ln Q_e = \left(\frac{1}{n}\right)\ln C_e + \ln K_F \tag{12}$$

K_F and $1/n$ = Freundlich isotherm constant (mg g^{-1}) and adsorption intensity, respectively. In one study, if the adsorption process follows the Freundlich model, it indicates adsorption on a heterogeneous surface and may suggest a chemisorption mechanism. The Freundlich constant provides information on the adsorption capacity.

Temkin isotherm:

$$Q_e = B \log K_T + B \log C_e \tag{13}$$

K_T is the Temkin isotherm constant (L g^{-1}), B is a constant related to the heat of adsorption ($= \frac{RT}{b}$, where b is the Temkin constant (J mol^{-1}), T is the absolute temperature (K), and R = universal gas constant (J mol^{-1} K^{-1})). The Temkin model suggests that adsorption is a multilayer process, considering that indirect interactions between the adsorbate and adsorbent and a linear decrease in adsorption heat with increased surface coverage occur, but are only valid for intermediate concentrations.

Dubinin-Radushkevich isotherm:

$$\ln Q_e = \ln Q_{max} - \beta \; \varepsilon^2 \tag{14}$$

β is the Dubinin-Radushkevich constant related to the adsorption energy; the mean adsorption energy (E) can be calculated as $E = \frac{1}{\sqrt{2\beta}}$, where ε = polanyi potential (in kJ^2 mol^{-2}) = $RT \ln\left(1 + \frac{1}{C_e}\right)$. The Dubinin-Radushkevich isotherm is an empirical model that describes the adsorption on surfaces with varying properties. However, it is only suitable for intermediate concentrations owing to its unrealistic asymptotic behavior. A semi-empirical equation, which assumes a multilayer character, was used to distinguish between the chemical and physical adsorption of metal ions. This depends on the temperature.

Elovich isotherm:

$$\ln\left(\frac{Q_e}{C_e}\right) = \ln(K_E Q_{max}) - Q_e/Q_{max} \tag{15}$$

Table 7 Summary of the advantages and limitations of various isotherm models

Aspect	Advantages	Disadvantages
Langmuir isotherm		
Monolayer coverage	Accurate for single-layer adsorption	Not applicable for multilayer scenarios
Surface homogeneity	Ideal for homogeneous sites	Fails for real porous/rough surfaces
Simplicity	Convenient to use and understand	Oversimplifies complex systems
Adsorbate interactions	Simplified and ignores them	Leads to errors in high coverage or interactive adsorbates
Applicability range	Works well at low pressures	Fails at high pressures
Temperature dependence	Not required	Neglects temperature effects on adsorption
Freundlich isotherm		
Surface type	Handles heterogeneous, non-uniform sites	Poor fit for homogeneous, ideal surfaces
Adsorption layers	Works for multilayer adsorption	Cannot predict saturation/monolayer coverage at high pressure
Mathematical simplicity	Only two empirical constants	Constants lack mechanistic physical meaning
Practical application	Widely used for real-world adsorbents	Limited theoretical explanation; purely empirical
Range of applicability	Valid at low pressure/concentration	Invalid for high-pressure/saturation regions
Parameter dependency	Adaptable to different systems	Constants must be experimentally determined for every system
Temkin isotherm		
Adsorbate interactions	Considers molecular interactions	Assumes a linear decline, which may not fit all systems
Surface type	Useful for moderate heterogeneity	Still based on a homogeneous surface assumption
Coverage range	Accurate at moderate coverage	Not valid at very low/high concentrations
Mathematical simplicity	Two-parameter model, easy to apply	Parameters lack direct physical meaning
Predictive power	Good for catalysis, environmental science	Not suitable for extremes or true saturation
Dubinin-Radushkevich isotherm		
Micropore adsorption	Accurately models pore filling in microporous materials	Limited accuracy for low pressure/zero loading
Surface energy	Handles heterogeneous/Gaussian energy distribution	Not suitable for mesoporous/macroporous materials
Physical vs. chemical	Can help distinguish the adsorption mechanism	Parameter determination is empirical
Theoretical foundation	Based on polanyi potential theory	Does not model multilayer adsorption
Porosity insights	Estimates porosity and energy of adsorbents	Valid only above 15% micropore filling
Elovich isotherm		
Surface heterogeneity	Models varying site energies, suitable for complex surfaces	Not applicable to homogeneous surfaces
Adsorption process	Valid for chemisorption and multilayer scenarios	Less reliable at high coverage or multilayer not present
Mathematical utility	Simple to use; fits for kinetic and equilibrium data	Empirical parameters lack deep mechanistic meaning
Capacity prediction	Predicts multilayer and dynamic adsorption	Underestimates actual maximum adsorption capacity
Practicality	Widely used in environmental, pollutant adsorption	Sometimes exhibits lower fit quality than other models

K_E is the Elovich isotherm constant (L mg^{-1}). The model, based on a kinetic principle, suggests multilayer adsorption, assuming an exponential expansion of the adsorption sites initially designed for gas chemisorption onto solids. The advantages and limitations of the isotherm model are presented in Table 7.

In each case, the percentage of removal (including adsorption and degradation) was calculated using the following equation (eqn (16)).

$$\text{Removal(\%)} = \frac{C_0 - C_t}{C_0} \qquad (16)$$

where C_0 and C_t are the initial and final U(VI) concentrations, respectively.

Using the above equations, the efficiency, mechanism, and optimal conditions of the adsorption techniques for the removal of several contaminants can be evaluated.

For example, Kalantary et al.[186] removed nitrate from water using activated carbon-magnetite nanoparticles. After the batch adsorption experiment, the results were plotted in a linear form using the Langmuir, Freundlich, and Temkin isotherm models. The Langmuir isotherm model was found to be the most suitable ($R^2 = 0.99$, close to unity), with a maximum adsorption capacity of 57.1 mg g^{-1} at pH 3 and contact time of 60 min. Several nanomaterials have been reported to be effective in removing various hazardous contaminants (Table 8).

5.3.3 Thermodynamics study of adsorption. Thermodynamic parameters are crucial for estimating the spontaneity and viability of adsorption processes because they provide useful information for the design of adsorption processes. The enthalpy change [ΔH° (kJ mol^{-1})], Gibbs free energy of adsorption [ΔG° (kJ mol^{-1})], and entropy change [ΔS° (kJ mol^{-1} K^{-1})] were calculated using eqn (17) and (18).[197] The Langmuir constant K_L was computed for each of the aforementioned parameters at different temperatures. Langmuir model

Table 8 Reported phytogen@MNPs and their contaminant removal techniques

Nanomaterials	Waste contaminants	Conditions	Maximum adsorption capacity, Q_{max} (mg g^{-1})	Ref.
Adsorption				
Portulaca oleracea extract@MNPs	Cd(II)	20 ± 2.0 °C, pH 6, 60 min	177.48	187
	Pb(II)		108.22	
Leaf extract of *Thymus schimperi*@MNPs	Hg(II)	25 ± 0.5 °C, pH 5, 90 min	60.00	131
	Cr(VI)		57.37	
Artocarpus heterophyllus leaf extract coated maghemite@MNPs	Pb(II)	30 ± 1.0 °C, pH 6.5, 15 min	108.57	188
Sugarcane bagasse extract@MNPs	Carbofuran	rt, pH 7, 720 min	175.00	189
	Iprodione	rt, pH 7, 480 min	119.00	
Peanut shell extract@MNPs	Carbofuran	rt, pH 7, 480 min	89.30	
	Iprodione	rt, pH 7, 720 min	2.76	
Chromolaena odorata aqueous extract@MNPs	Cr(VI)	rt, pH 2, 10 min	173.12	190
Peel extract of jengkol (*Archidendron pauciflorum*)@MNPs	MB	rt, pH 6, 120 min	68.49 mol g^{-1}	191
Aqueous flower extract of *Murraya paniculata (L) Jack*@MNPs	Fast sulphon black-F dye	rt, pH 4, 40 min	6.62	24
Parkia Speciosa Hassk. peel extracts@MNPs		pH 4, 120 min	—	192

Nanomaterials	Waste contaminants	Conditions	Rate constant, k_n [(mg g^{-1})$^{1-n}$ min^{-1}]	Ref.
Photodegradation				
Nigella sativa seed aqueous extract@MNPs	Hydrocortisone	rt, pH 7, 540 min, 254 nm	$k_1 = 0.00271$	129
Cynara cardunculus leaf aqueous extract @MNPs NPs	MB	rt, pH 7, 80 min	$k_2 = 0.00617457^a$	193
Andean blackberry leaf extract@MNPs	MB	rt, 120 min, sunlight	$k_1 = 0.0105475$	194
	Congo red	rt, 120 min, sunlight	$k_1 = 0.0043240$	
	Methyl orange (MO)	rt, 120 min, sunlight	$k_1 = 0.0028930$	
Calotropis gigantea leaf extract@MNPs	MB	rt, 50 min, sunlight	—	195
Caralluma acutangula leaf aqueous extract@Fe^0/MNPs	MB	30 °C, 150 min, 254 nm	$k_1 = 0.13343$ (apparent)	147
ARM@MNPs	Cresol red	30 °C, pH 5.25, 60 min, 365 nm	$k_1 = 0.00152$	196
ROS@MNPs		30 °C, pH 5.05, 60 min, 365 nm	$k_1 = 0.00149$	
MAT@MNPs		30 °C, pH 4.63, 60 min, 365 nm	$k_1 = 0.00120$	
JUN@MNPs		30 °C, pH 3.69, 60 min, 365 nm	$k_1 = 0.00100$	

^{a} Denotes g mg^{-1} min^{-1}

parameters can be applied to the thermodynamics of adsorption. Therefore, we can determine the thermodynamic parameters by plotting $\ln K_L$ *vs.* $1/T$.

The Van't Hoff equation is as follows:

$$R \ln K_L = -\frac{(\Delta H^\circ)}{T} + \Delta S^\circ \qquad (17)$$

$$\Delta G^\circ = \Delta H^\circ - T\Delta S^\circ \qquad (18)$$

where T is the absolute temperature, $K_L = Q_e/C_e$ is the standard thermodynamic equilibrium constant, R is the universal gas constant (J mol^{-1} K^{-1}), ΔS° is the slope of the plot of $\ln K_L$ *versus* $1/T$, and ΔH° is the intercept. Another parameter that can be calculated is the activation energy (E_{act}), which is a measure of the initiation energy required for adsorption.

The above formulae can be used to plot the thermodynamic curve between $\ln K_L$ and $1/T$, and the slope and intercept of the van't Hoff plots can be used to deduce the thermodynamic parameters. At a specific temperature, the spontaneity and

feasibility of the adsorption reaction are indicated by the negative value of ΔG°.[198] The feasibility of adsorbate adsorption decreases as the temperature increases, as indicated by the increasing ΔG° value. This process is referred to as physisorption when the ΔH° values fall between −20 and 40 kJ mol^{-1}, and chemisorption when the values fall between –80 and 400 kJ mol^{-1}.[199] In addition, the negative ΔH° value indicates that the adsorption process is exothermic.[198] When the adsorbate was adsorbed, there was more unpredictability at the adsorbate–adsorbent interface, as indicated by the positive values of ΔS°.[198,199] The thermodynamic parameters are listed in Table 9.

5.4 Photocatalytic degradation of organic and inorganic pollutants

5.4.1 Kinetic equations used in the photocatalytic degradation process. The photocatalytic degradation rate was predicted by using a kinetic model. It also explains the mechanism by studying the photodegradation under different conditions,

namely pH, wavelength of light, substrate concentration and the presence of electron/hole/ROS acceptors (H_2O_2, $AgNO_3$, MeOH, IPA *etc.*). The three kinetic equations are as follows (eqn (19)–(21)):

Pseudo-first-order equation:

$$\ln C_t = -kt + \ln C_0 \qquad (19)$$

Pseudo-second-order equation:

$$\frac{1}{C_t} = kt + \frac{1}{C_0} \qquad (20)$$

Pseudo-zeroth-order equation:

$$C_t = -kt + C_0 \qquad (21)$$

C_0 and C_t = initial concentration and concentration after time t, respectively, and k = rate constant. $\ln C_t$ *vs.* t, $1/C_t$ *vs.* t, and C_t *vs.* t were plotted to determine whether the degradation of the respective dyes followed pseudo-first-order, pseudo-second-order, or pseudo-zeroth-order kinetics, respectively.

During the kinetic experiments, the initial steps were performed in the dark (without irradiation) to determine whether the process involved exclusively photodegradation or adsorption. If adsorption occurred, the experimental solution was kept in the dark, and the absorbance was continuously measured until equilibrium was reached. After adsorption, the experimental solution was exposed to UV or sunlight to initiate photodegradation. Fig. 12 shows the use of phytogen@MNPs for the photodegradation of wastewater contaminants.

Fatimah *et al.*[200] used MNPs synthesized using *Parkia speciosa* Hassk pod extract and applied them to bromophenol blue (BPB) degradation. From the obtained results, it was found that

Table 9 Various reported thermodynamic parameters for the adsorption of pollutants onto phytogen@MNPs

MNPs	Pollutant(s)	T (K)	E_{act} (kcal mol^{-1})	ΔH° (kcal mol^{-1})	ΔS° (cal mol^{-1} K^{-1})	ΔG° (kcal mol^{-1})
Terminalia arjuna@MNPs[54]	Pb(II)	290	—	−20.78[a]	−66.26[b]	−1.62[a]
		300				−0.78[a]
		310				−0.30[a]
Terminalia arjuna@MNPs[54]	MB	290	—	−38.60[a]	−99.69[b]	−9.74[a]
		300				−8.68[a]
		310				−7.75[a]
Artemisia herba-alba @MNPs[146]	Evans blue dye	303.15	2.79	2.85	13.03	−1.09
		308.15				−1.18
		313.15				−1.23
		318.15				−1.29
Rosemarinus officinalis @MNPs[146]	Evans blue dye	303.15	3.21	3.32	14.04	−0.93
		308.15				−1.00
		313.15				−1.09
		318.15				−1.14
Matricaria Pubescens @MNPs[146]	Evans blue dye	303.15	5.59	5.96	20.86	−0.36
		308.15				−0.47
		313.15				−0.58
		318.15				−0.67
Juniperus Phoenicia @MNPs[146]	Evans blue dye	303.15	6.29	6.54	22.70	−0.35
		308.15				−0.43
		313.15				−0.56
		318.15				−0.66
Artemisia herba-alba@MNPs[146]	MO	303.15	3.27	3.31	13.24	−0.69
		308.15				−0.78
		313.15				−0.83
		318.15				−0.89
Rosemarinus officinalis @MNPs[146]	MO	303.15	3.66	3.78	14.63	−0.65
		308.15				−0.74
		313.15				−0.81
		318.15				−0.87
Matricaria Pubescens @MNPs[146]	MO	303.15	6.28	6.75	22.54	−0.07
		308.15				−0.19
		313.15				−0.33
		318.15				−0.41
Juniperus phoenicea @MNPs[146]	MO	303.15	8.45	8.67	27.27	+0.16
		308.15				+0.08
		313.15				−0.07
		318.15				−0.24

[a] kJ mol^{-1}. [b] J mol^{-1} K^{-1}.
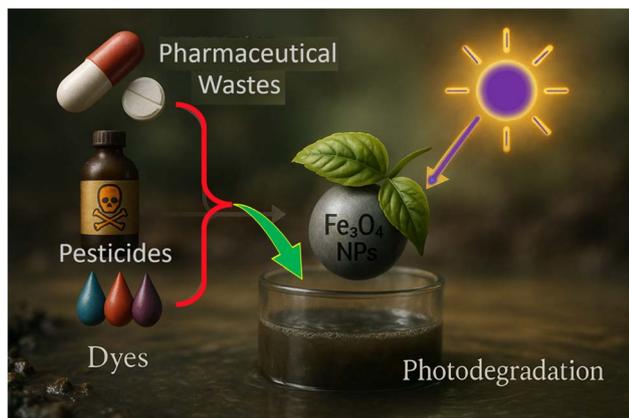
Fig. 12 A pictorial illustration of the photodegradation of water contaminants by phytogen@MNPs.

the R^2 values of the pseudo-second-order kinetic model were higher ($R^2 = 0.98$–0.99, *i.e.*, close to unity) than those of the pseudo-first-order kinetic model ($R^2 = 0.77$–0.90, not close enough to unity), so it can be concluded that the photocatalytic degradation of BPB obeyed pseudo-second-order kinetics at all initial concentrations of BPB. Additionally, they proposed that the data fit for the pseudo-second-order model demonstrated how the reaction rate was affected by both the photocatalyst material activity and the role of BPB as a reactant. After examining the kinetic models, the surface process was explained, indicating that the photocatalyst adsorbed BPB. These investigations demonstrated that chemisorption was the primary mechanism governing the interaction of cationic dyes such as BPB with the surface of the synthesized MNPs. A few reported photocatalytic degradations using phytogen@MNPs are presented in Table 8.

The degradation mechanism can be elucidated through scavenging experiments, which provide insights into the types of ROS responsible for the degradation process, such as superoxide anions ($^\bullet O_2^-$), hydroxyl radicals ($^\bullet OH$), and singlet oxygen ($^1O_2$). In these experiments, different types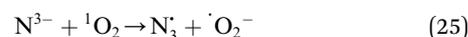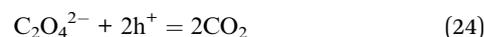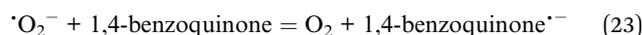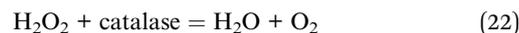 of agents (water-soluble compounds) were introduced into the solution containing the target pollutant and phytogen@MNPs. Upon irradiation, pollutant degradation by phytogen@MNPs was either suppressed or inhibited by specific interfering agents. This approach is known as the scavenging experiment. Different interfering agents are known to selectively scavenge specific ROS (Table 10), thereby providing concrete evidence regarding

the type of ROS that is actively involved in the degradation process. The degradation mechanisms of the different ROS are shown in Fig. 13.

Suppose that ROS are generated by visible or UV irradiation of phytogen@MNPs and degrade pollutants. When a specific scavenger for a particular ROS was introduced into the solution, the degradation percentage decreased compared with its initial value. The scavenger reacts, thereby reducing the concentration of ROS and subsequently deactivating them in the solution. The deactivation reaction of ROS is represented by eqn (22)–(29):

$$H_2O_2 + catalase = H_2O + O_2 \quad (22)$$

$$^\bullet O_2^- + \text{1,4-benzoquinone} = O_2 + \text{1,4-benzoquinone}^{\bullet-} \quad (23)$$

$$C_2O_4^{2-} + 2h^+ = 2CO_2 \quad (24)$$

$$N^{3-} + {}^1O_2 \rightarrow N_3^\bullet + {}^\bullet O_2^- \quad (25)$$

$$2Cl^- + 2e^- = Cl_2 \quad (26)$$

$$2I^- + 2e^- = I_2 \quad (27)$$

$$CO_3^{2-} + HO^\bullet \rightarrow CO_3^{\bullet-} + HO^- \quad (28)$$

$$HCO_3^- + HO^\bullet \rightarrow CO_3^{\bullet-} + H_2O \quad (29)$$
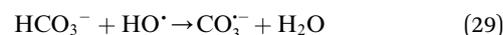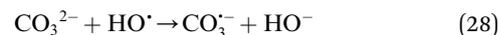
5.4.2 Thermodynamics study for degradation. Photocatalytic degradation is a chemical reaction in which an organic molecule is dissociated; hence, the process depends on temperature. A chemical reaction has a certain activation energy that determines whether the process will proceed further and faster. Therefore, experiments should be performed under irradiation at various temperatures. If the degradation process obeys a 1st order type reaction, the thermodynamic parameter (activation energy) can be obtained using the Arrhenius equation (eqn (30)). In general, between the variable temperatures, if there is a ten-degree difference, then the $\ln k_1$ values would not be very close. It is well known that when there is a ten-degree rise in temperature, k_1 becomes approximately double or triple.

$$\ln k_1 = \ln A - \left(\frac{E_{act}}{R}\right) \times \left(\frac{1}{T}\right) \quad (30)$$

Here in eqn (30), A, E_{act}, R, and T = the frequency factor (in s^{-1}), activation energy (in kJ mol^{-1}), universal gas constant (J mol^{-1} K^{-1}), and absolute temperature (in K), respectively. Table 11

Table 10 Representative molecules/ions/enzymes used to identify specific ROS

| ROS	Scavenger	References
$^\bullet O_2^-$	Methanol, 1,4-benzoquinone, superoxide dismutase	201–205
$^\bullet OH$	Isopropyl alcohol, *tert*-butyl alcohol, sulphate, monobasic phosphates, carbonate, bicarbonate	203–207
h$^+$	Oxalate, sulphite, chloride, iodide, ethylenediamintetraacetic acid disodium, triethanolamine, Formic acid	201–206
e$^-$	N-phenylaniline, cupric nitrate, dichromate, bromate	205–207
O$_2^1$	Azide, deuterium oxide, L-histidine	202, 205, and 206
H$_2$O$_2$	Catalase	205
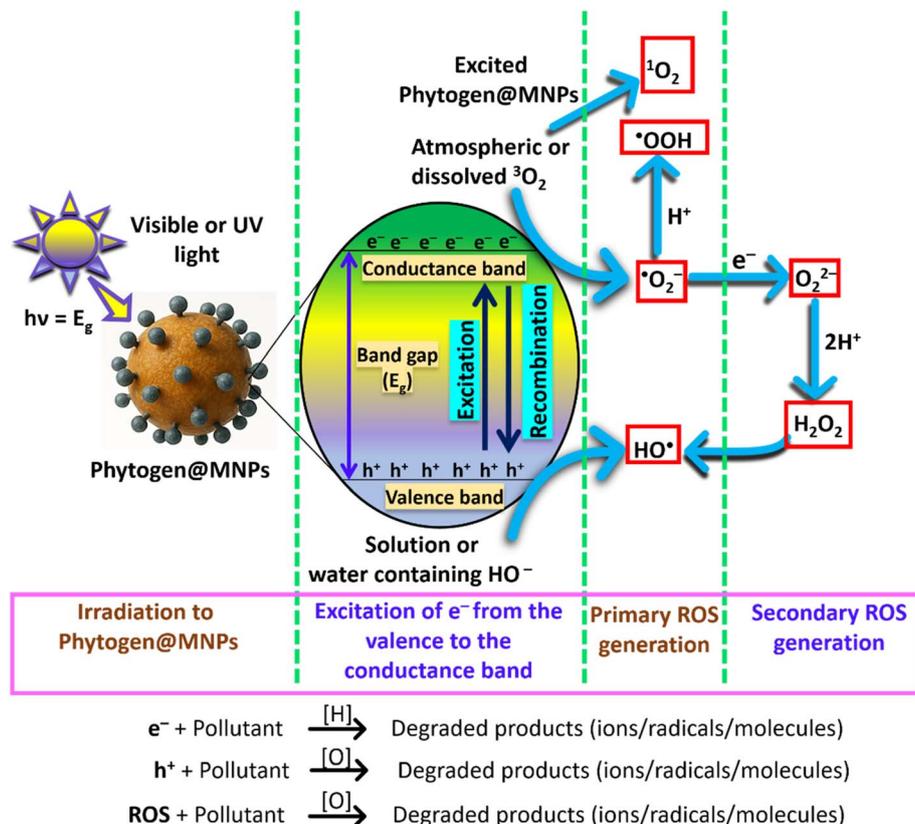
Fig. 13 ROS generation and mechanism of pollutant photodegradation by phytogen@MNPs.

presents the thermodynamic parameters for the degradation of various contaminants using the phytogen@MNPs.

6. Recovery of phytogen@MNPs and reusability study

The recovery of the adsorbent or photocatalyst is an important step because it reduces the overall cost of the process. There are two types of adsorption process: physisorption and chemisorption. In physisorption, adsorbates are bonded to the NP surface *via* weak interactions, such as van der Waals forces; hence, there is a high probability of reversing the process, that is, the recovery of the adsorbent. In the case of chemisorption, there is a very strong interaction between the adsorbate and the adsorbent; hence, desorption becomes inefficient. Fig. 14 illustrates the regeneration of phytogen@MNPs from contaminants@phytogen@MNPs using various eluents *via* desorption.

The desorption of adsorbates from the surface of the adsorbent can be performed *via* certain processes, including chemical elution. The desorption efficiency was calculated using eqn (31). Numerous factors affect the efficiency of an eluent, such as the type of adsorbent and adsorbate, interaction between the adsorbate and adsorbent, and desorbing agent used. Acids, alkalis, salts, chelating agents, and solvents (*e.g.*, ethanol, methanol, isopropanol, and acetone) are among the most commonly used desorption agents.[208] In addition to elution, degradation of the adsorbate from the surface of the

adsorbent is an alternative process for removing adsorbed adsorbates from the adsorbent surface.

$$\% \text{ desorption} = \frac{C_d}{C_a} \times 100 \qquad (31)$$

The desorbed and adsorbed concentrations of MB and Pb(II) (mg L^{-1}) are denoted as C_d and C_a, respectively.

The desorption mechanism is similar to that of cation or anion exchange. In general, eluents with small cations such as H$^+$ and Na$^+$ provide better results for desorbing cationic adsorbates. After successive desorption, further adsorption–desorption cycles can be performed.

In the case of the photocatalytic degradation process, reusability can be checked directly by the repeated introduction of MNPs into fresh adsorbate solutions in the presence of irradiation. The percentage of degradation was monitored using a UV spectrophotometer.

7. Stability of nanoparticles after adsorption and degradation

The stability of magnetite nanoparticles (MNPs) coated with plant extracts is a critical factor for their effective application, particularly in environmental remediation and biomedical applications. This stability is influenced by the interaction between the plant extract coating, magnetite core, and surrounding environment, especially after the adsorption of

Table 11 Various reported thermodynamic parameters for the degradation of different pollutants using phytogen@MNPs

MNPs	Pollutant(s)	T (K)	E_{act} (kcal mol^{-1})	ΔH^o (kcal mol^{-1})	ΔS^o (cal mol^{-1} K^{-1})	ΔG^o (kcal mol^{-1})
Caralluma acutangula leaf aqueous extract@Fe(0)/MNPs[147]	MB	288.00	87.78[a]	308.40[a]	−323.00[b]	−92.98[a]
		293.00				−93.96[a]
		298.00				−95.89[a]
		303.00				−97.50[a]
Aqueous *Nigella sativa* seed extract@MNPs[129]	Hydrocortisone	293.00	35.40[a]	—	—	—
		303.00				
		313.00				
Artemisia herba-alba @MNPs[196]	Cresol red	303.15	3.68	4.02	15.58	−0.71
		308.15				−0.78
		313.15				−0.85
		318.15				−0.95
Rosemarinus officinalis @MNPs[196]		303.15	3.72	4.78	17.60	−0.61
		308.15				−0.65
		313.15				−0.73
		318.15				−0.82
Matricaria Pubescens @MNPs[196]		303.15	5.09	5.63	19.81	−0.38
		308.15				−0.46
		313.15				−0.57
		318.15				−0.65
Juniperus phoenicea @MNPs[196]		303.15	6.23	6.24	21.35	−0.24
		308.15				−0.33
		313.15				−0.46
		318.15				−0.55

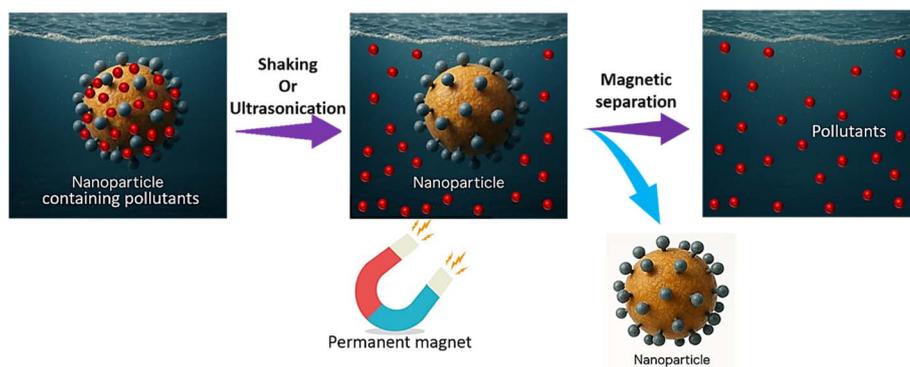[a] kJ mol^{-1} [b] J mol^{-1} K^{-1}.

Fig. 14 Schematic representation of nanoparticle recovery *via* desorption.

pollutants and degradation processes. After an adsorption–desorption cycle, if phytogen@MNPs do not exhibit any structural changes, they can be used repeatedly until their efficiency decreases. FTIR, powder XRD, TGA, and XPS analyses were used to obtain stability information for the MNPs. Similar (or identical) initial and final data suggest that the MNPs are stable and can be reused.

7.1 Stability before adsorption

7.1.1 Role of plant extracts in stability. Plant extracts are widely utilized in the green synthesis of MNPs, serving as natural reducing and stabilizing agents due to their rich composition of biomolecules like phenols, flavonoids, proteins,

and carboxylic acids.[209–212] These biomolecules form a protective layer around the magnetite core, which is essential for maintaining colloidal stability, preventing agglomeration, and enhancing the nanoparticles' overall performance.[213]

7.1.2 Protective coating. The plant extract coating acts as a barrier, preventing direct contact between the magnetite core and surrounding medium, which can lead to oxidation or dissolution. For instance, Yerba Mate (*Ilex paraguariensis*) extract-coated magnetite nanoparticles (YM@MNPs) were found to have a crystalline magnetite core surrounded by shells of Fe_3O_4, FeO, and Fe_2O_3 oxides. The YM extract effectively protected the MNPs by incorporating surface carboxylates, phenols, and organic N groups, which improved their stability in aqueous suspensions.[210]

7.1.3 Surface functionalization. The functional groups from plant extracts (*e.g.*, –OH and –COOH from polyphenols) provide active sites for adsorption and contribute to the electrostatic or steric stabilization of the nanoparticles, maintaining their dispersion in solution.[210] *Curcuma longa* L. extract, for example, provides a surface layer of polyphenol groups to MNPs, contributing to their stability.

7.2 Stability after adsorption

The stability of plant extract coated MNPs can be significantly affected by the adsorption of target substances such as pollutants in wastewater treatment or active molecules for drug delivery.[214]

7.2.1 Changes in surface properties. Adsorption of molecules onto the plant extract coating can alter the surface charge and hydrophilicity of nanoparticles, potentially leading to aggregation or sedimentation.[214] This is particularly relevant in wastewater treatment, where NPs are designed to adsorb organic pollutants, toxic metal ions, and bacteria.[43]

7.2.2 Examples. (i) Dye adsorption: in a study using *Cordia myxa* leaf extract-coated MNPs for methylene blue (MB) adsorption, the maximum adsorption capacity was found to be 17.79 mg g^{-1} after one hour of incubation at pH 7.5.[214] The electrostatic attraction between the MB and MNPs played a significant role in the adsorption process. Although the nanoparticles exhibited superparamagnetic behavior and could be easily recovered by an external magnet, their long-term stability and reusability over multiple adsorption–desorption cycles need to be thoroughly assessed. The phytochemical coating of nanoparticles is crucial for their stabilization during the adsorption process.[214]

(ii) Oil spill collection: magnetite nanoparticles modified with green hydrophobic biocomponents extracted from *Anthemis pseudocotula* (AP) were used to collect heavy crude oil spills.[215] Surface modification helped fine-tune the MNPs for this application. While these particles showed high efficiency in oil collection and could be recycled using an external magnetic field after 5 min of adsorption, their long-term stability after repeated oil adsorption and recovery cycles requires further investigation to ensure consistent performance and to prevent leaching of the plant extract coating or aggregation of the nanoparticles.[215] The thermal stability and magnetic properties of these nanoparticles were characterized, and the influence of the plant extract on dispersion and stability was noted.

7.3 Stability during degradation

The degradation of plant extract coated MNPs can occur owing to various factors, including chemical, biological, or thermal processes, and can lead to a loss of functionality or potential environmental risks.[216]

7.3.1 Coating degradation. The organic nature of plant extracts makes coatings susceptible to degradation over time or under harsh conditions. This degradation can expose the underlying magnetite core, leading to aggregation, oxidation, and interaction with the environment.[216,217]

7.3.2 Example. (i) Thermal degradation: TGA is often used to evaluate the thermal stability of plant extract coatings on MNPs. For example, in a study synthesizing Fe_3O_4 nanoparticles using *Cordia myxa* leaf extract, TGA was used to confirm the formation of a plant protein-coated magnetite nanobiohybrid.[214] The thermal stability of magnetite within the nanoparticles is crucial because a temperature that is too high can convert it into hematite.[216] The degradation behavior of the plant extract coating at elevated temperatures indicates its susceptibility to thermal processes, which could affect its stability in applications involving heat or long-term storage.[216]

(ii) Degradation of other organic coatings: although not derived from a plant extract, studies on BSA-coated magnetite nanoparticles demonstrated that thermal characterization using thermogravimetric analysis (TGA) was effective in understanding the degradation behavior of the protein coating.[217] The degradation of plant extract coatings follows similar principles, where the organic material breaks down over time, influencing the overall stability and reusability of the nanoparticles. The amount of coating, temperature, and time can significantly affect the stability and degradation of nanoparticles.[146]

7.3.3 Impact on functionality. The degradation of the plant extract coating can reduce the efficiency of the nanoparticles in subsequent adsorption cycles, as the active sites for binding pollutants may be lost or the nanoparticles may aggregate, thereby reducing their effective surface area.[214]

7.3.4 Environmental fate. The breakdown products of the plant extract and bare magnetite core can have different environmental impacts. Understanding the complete degradation pathway is vital for assessing the long-term environmental safety of these nanoparticles.[218] Although some studies have shown that plant extract-coated nanoparticles are effective in the degradation of organic contaminants, their own degradation products must also be considered.[218]

In conclusion, maintaining the stability of plant extract coated magnetite nanoparticles after adsorption and during degradation is paramount for their practical applications.[219] Careful selection of plant extracts, optimization of coating methods, and thorough characterization of their behavior under various conditions are crucial to ensure their efficacy, reusability, and environmental safety.[210,219]

8. Impact of natural ions on adsorption and degradation

Adsorption or degradation in synthetic wastewater can provide a good indication of the potential of MNPs for effective contaminant removal, whereas the same process in natural water bodies can provide specific insights into the real-world use of MNPs. Naturally occurring water bodies contain several cations and anions, such as Ca^{2+}, Na^+, F^-, SO_4^{2-}, CO_3^{2-}, and Cl^-. Adsorption is involved in the surface coverage process *via* adsorbent–adsorbate interactions. When these ions are present in solution, the competition between the adsorbate and these ions varies depending on the nature of the ZP (at the working
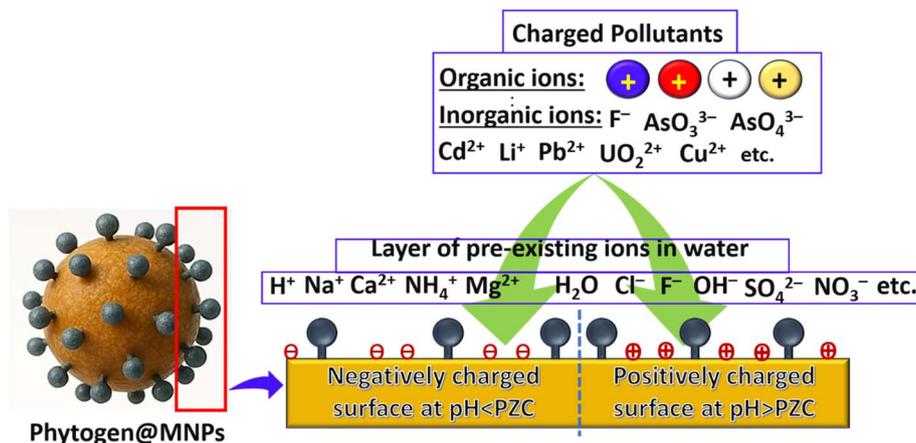
Fig. 15 Pictorial representation of the effect of natural ions on pollutant removal.

pH). The effects of water-containing ions on the adsorption process are illustrated in Fig. 15.

When an adsorbate possesses a positive charge and is introduced into MNPs, which are typically negatively charged, positive ions such as Ca^{2+} and Na^+ may interfere with the adsorbates. If these interfering ions exhibit a higher charge density than the adsorbate, they initially form surface coverage, followed by adsorbate ions, resulting in a decrease in the adsorption efficiency. During the degradation process, adsorbates are first adsorbed, after which degradation commences *via* reactive oxygen species (ROS) activity. Consequently, a reduction in degradation efficiency may occur for the same reason.

Guan *et al.*[220] investigated the effects of five cations and five anions on quinolone adsorption by iron-containing minerals and found that K^+, Na^+, NH_4^+, Cl^-, NO_3^-, and SO_4^{2-} exhibited less substantial inhibition of adsorption than Mg^{2+}, Ca^{2+}, HCO_3^-, and $H_2PO_4^-$. They also collected samples of naturally occurring surface water, which they then employed as a medium to study the adsorption behavior of quinolones on iron-containing minerals. Maintaining natural water's buffering capacity under circumneutral conditions, they observed that the amount of adsorption was primarily promoted in the goethite system (from 0.56–0.78 μmol g^{-1} to 0.52–1.43 μmol g^{-1}), but inhibited in the other systems (kaolin: from 1.98–1.99 μmol g^{-1} to 0.90–1.40 μmol g^{-1}; magnetite: from 1.13–1.33 μmol g^{-1} to 0.45–0.76 μmol g^{-1}; kaolin: from 1.98–1.99 μmol g^{-1} to 0.90–1.40 μmol g^{-1}); and hematite: from 0.52–0.65 μmol g^{-1} to 0.02–0.18 μmol g^{-1}

9. Antibacterial activity study

In addition to the efficiency of removing organic and inorganic contaminants, the antimicrobial efficacy of MNPs against various waterborne microbes is a crucial criterion, as these microbes can cause significant diseases, such as diarrhea and typhoid. Therefore, the elimination of microbes is also important.

The antibacterial activity of phytogen@MNPs is primarily enabled by multiple specific mechanisms that effectively target the bacterial cells. One key mechanism is the generation of ROS,

such as superoxide and hydroxyl radicals, which cause oxidative stress in bacterial cells, leading to damage to cellular components, including membranes, proteins, and DNA. Oxidative damage disrupts bacterial membrane integrity and metabolism, leading to cell death. Additionally, the physical contact of MNPs with bacterial cell walls results in membrane disruption through direct mechanical interactions and electrostatic forces, as many phytogen@MNPs carry surface charges that facilitate strong binding to negatively charged bacterial membranes. This binding weakens the bacterial wall and increases permeability, causing the leakage of essential intracellular materials. Moreover, phytogen@MNPs can interfere with intracellular processes by penetrating bacterial cells, where they can inhibit protein synthesis and disturb DNA replication, thereby further impairing bacterial survival and reproduction. Some biomodifications involve conjugation with antibacterial agents or molecules that enhance targeting and adhesion to bacteria, thereby amplifying the antimicrobial efficiency. These nanoparticles can also suppress bacterial defense mechanisms, such as efflux pumps and resistance gene expression, which helps overcome antibiotic resistance. The magnetic core facilitates the targeted delivery and concentration of nanoparticles at infection sites using external magnetic fields, improving localized antibacterial action and minimizing side effects. Together, these mechanisms contributed to the broad-spectrum and potent antibacterial activity of phytogen@MNPs against both Gram-positive and Gram-negative bacteria, including drug-resistant strains.

Antibacterial studies are a measure of the toxicity of MNPs towards various types of bacterial samples. Two different methods were used to study the antibacterial activity (Fig. 16).

(A) Measurement of minimum inhibitory concentration (MIC), that is, the concentration at which cell viability is minimal (compared to the reference).

(B) Measurement of the zone of inhibition (ZOI) using the disc diffusion method.

First, the bacterial culture was grown in broth (*e.g.*, Luria broth) by stirring the selected bacteria overnight. After overnight incubation (37 °C), colonies were counted to obtain CFU mL^{-1} from each plate. Then, it was diluted (a generally accepted
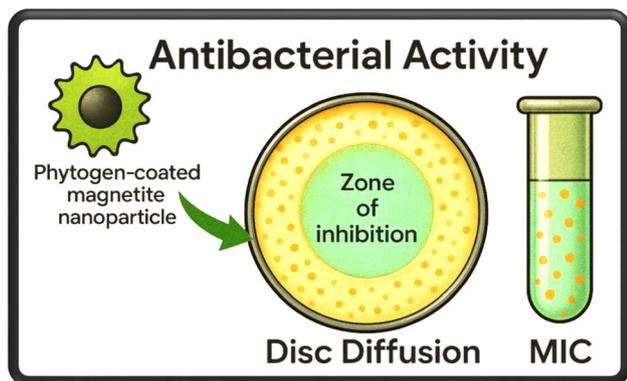
Fig. 16 Pictorial illustration of the antibacterial activity of phytogen@MNPs.

CFU lies between 30 and 300) at a particular dilution using the following equation (eqn (32)):

$$CFU = \frac{Number\ of\ colonies\ \times\ total\ dilution\ factor}{Volume\ of\ cultured\ plate} \quad (32)$$

Below 30 and above 300, the colony counts were very low and very high, respectively; thus, errors may occur. Therefore, these plates should be carefully selected for use in future studies.

Here,

$$Total\ dilution\ factor = 10^{sum\ of\ serial\ number\ of\ dilutions}$$

Subsequently, a primary (original) suspension of phytogen@MNPs was prepared and diluted to obtain suspensions with different concentrations. After taking a colony and growing it in broth media, dilution should be performed until an optical density of less than 0.1 is achieved. Different concentrations of phytogen@MNPs were added to the diluted bacterial solution (with an optical density of less than 0.1) and allowed to grow overnight. Thus, the minimum inhibitory concentration (at which the bacterial concentration was the lowest) was measured.

Freshly collected colonies were used to measure the ZOI using the disc diffusion method. Similarly, in this method, different commercial antibiotics and a very dilute suspension of phytogen@MNPs were used on agar plates containing the same dilution of bacterial culture. After one or more days, the size of the zone or well (the circle around which bacteria cannot grow) was measured and compared with that of the control. After comparison, it was concluded that MNPs are efficient candidates (for bacterial removal). Antibacterial processes must be performed at 37 °C, and all equipment, glassware, and tables should be sterilized. Almost in all cases, experiments were performed repeatedly at least three times to obtain data on the reproducibility of the antibacterial analysis.

For example, anthocyanin-rich berry extracts have been used to coat MNPs. Anthocyanin compounds not only improve the stability of nanoparticles but also significantly enhance their antibacterial activity against common bacterial strains, making them promising for biomedical and environmental applications.[221,222] In another study, MNPs were synthesized and stabilized using *Ipomoea aquatica* leaf extract, exhibiting significant antibacterial activity. During the agar well diffusion method, the nanoparticles exhibited a ZOI of 19 mm against Gram-negative *E. coli* and 14 mm against Gram-positive *Bacillus subtilis*. This indicates strong antibacterial effects, especially against *E. coli*, and demonstrates that the bioextract-coated

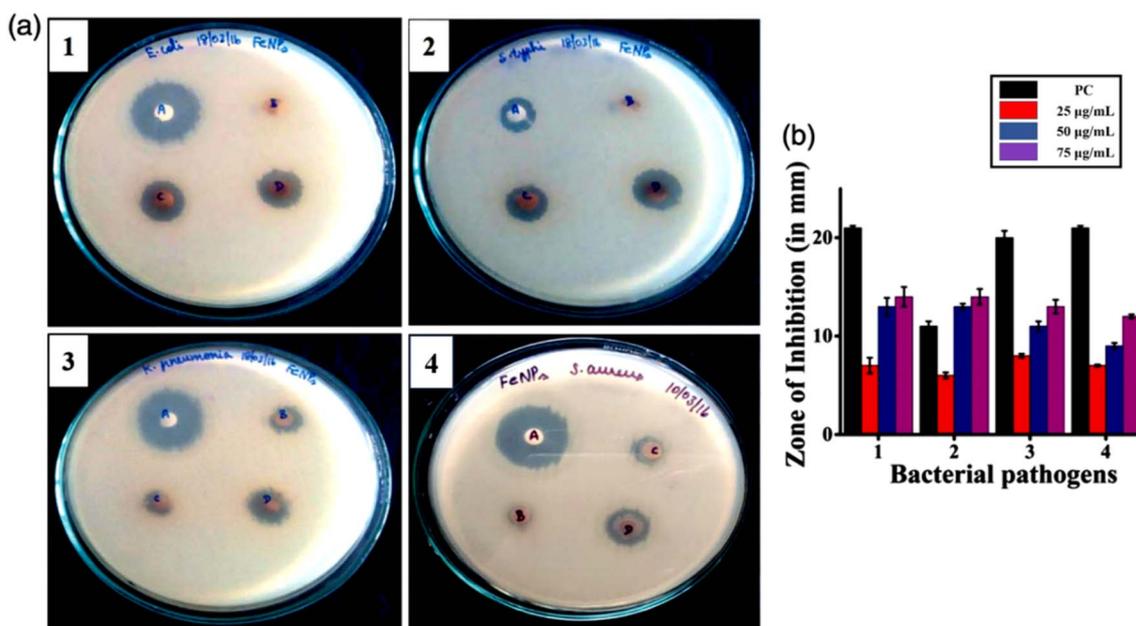Fig. 17 Antibacterial efficacy of CG@MNPs: (a) disc diffusion assay showing ZOIs in a dose-dependent manner against (1) *E. coli* MTCC 1687, (2) *S. typhi* MTCC 3917, (3) *K. pneumonia* MTCC 530, and (4) *S. aureus* MTCC 96, (A) positive control, (B–D) 25, 50 & 75 μg mL^{-1} CG@MNPs); (b) ZOIs for the CG@MNPs against the used bacterial samples (source: this image is taken from an artilcle written by Sathishkumar *et al.*[225]).

Table 12 ZOI of various phytogen@MNPs against different bacterial strains

MNPs	Bacterial strains	Concentration	ZOI	Ref.
Citrus sinensis peel extract@MNPs	*S. aureus*	400 μg mL^{-1}	30	132
	St. mutans		37.3	
	B. subtilis		22.3	
	E. coli		30	
	K. pneumonia		14.7	
	C. albicans		22.6	
Moringa oleifera@MNPs	*A. sobria*	—	21	226
Calotropis procera aqueous leaf extract@MNPs	*K. pneumonia*	—	7.1	127
	S. aureus		22.5	
	B. subtilis		22.4	
	A. niger		16.9	
	F. oxysporum		14.7	
Glycosmis mauritiana leaf extract@MNPs	*B. cereus*	30 μg per disc	11 ± 1.0	227
	B. subtilis		19 ± 2.6	
	E. faecalis		18 ± 2.0	
	E. coli		19 ± 1.0	
	K. pneumonia		12 ± 1.0	
	M. luteus		16 ± 2.0	
	P. mirabilis		11 ± 1.0	
	P. vulgaris		19 ± 1.7	
	P. fluorescence		18 ± 1.7	
	S. aureus		16 ± 1.2	
	V. fluvialis		10 ± 1.5	
Protoparmeliopsis muralis lichen aqueous extract@MNPs	*E. coli*	0.1 M (salt concentration)	12 ± 0.89	228
	S. aureus		15 ± 0.89	
	P. aeruginosa		13.66 ± 1.36	
Eichhornia crassipes leaf extract@MNPs	*S. aureus*	100 μg mL^{-1}	23.3 ± 1	229
	P. fluorescens		22.6 ± 1	
	E. coli		20 ± 1	
	P. aeruginosa		∼17	
	P. vulgaris		∼18	
Zea mays L.*ear* leaves aqueous extract@MNPs + kanamycin	*B. cereus*	25 + 5 μg per disc	9.87 ± 0.34	230
	E.coli		18.86 ± 0.82	
	L. monocytogenes		13.54 ± 0.30	
	S. aureus		13.09 ± 0.15	
	S. typhimurium		13.3 ± 0.47	
Zea mays L.*ear* leaves aqueous extract@MNPs + amphotericin b	*C. albicans* KACC 30003	25 + 5 μg per disc	9.37 ± 0.31	
	C. albicans KACC 30062		16.69 ± 0.10	
	C. glabrata KBNO 6P00368		10.39 ± 0.37	
	C. glabrata KACC 30061		15.97 ± 0.58	
	C. saitoana KACC 41238		10.59 ± 0.18	
Leucas aspera aqueous leaf extract@MNPs	*E. coli*	50 μg mL^{-1}	12	231
	K. pneumoniae		10	
	P. mirabilis		17	
	S. enterica		21	
	S. flexneri		20	
	V. cholera		12	
	P. aeruginosa		21	
	B. cereus		0	
Calotropis procera leaf extract@MNPs	*E. coli*	100 mg mL^{-1}	0	127
	K. pneumonia		7.1 ± 0.28	
	S. aureus		22.5 ± 0.42	
	B. subtilis		22.4 ± 0.89	
	A. niger		16.9 ± 0.67	
	F. oxysporum		14.7 ± 0.73	
Qazwan Seeds extract@MNPs	*E. coli*	20 mg mL^{-1}	18	232
	A. baumannii		20	
	P. aeruginosa		20	
	K. pneumonia		22	
	E. faecalis		20	
	C. albicans (fungi)		10	
Aqueous flower extract of *Murraya paniculata (L) Jack*@MNPs	*Enterococcus faecalis*	10 μg mL^{-1}	11	24
	Pseudomonas aeruginosa		10	

MNPs were effective in biocidal applications against pathogenic bacteria.[223] The synthesis of MNPs using *Jatropha podagrica* leaf extract highlights their potent antibacterial activity. In agar well diffusion tests, 150 μL of these nanoparticles showed ZOIs of 13 mm for *Bacillus coagulans*, 15 mm for *S. aureus*, 11 mm for *E. coli*, and 10 mm for *Klebsiella pneumoniae*. This study indicates that antibacterial effects occur through oxidative stress *via* ROS, damaging bacterial membranes and essential biomolecules.[145] MNP synthesis using *Borassus flabellifer* seed coat extract demonstrated significant antibacterial activity against *E. coli*, *S. aureus*, *Shigella*, and *B. subtilis*. The antibacterial efficacy increased with nanoparticle concentration, showing ZOIs of up to 26 mm for *B. subtilis* at a concentration of 500 μg mL^{-1}. This enhanced activity results from the synergistic effects of the nanoparticles and bioactive phytochemicals in the seed coat extract, which induce oxidative stress and disrupt bacterial cells. These nanoparticles exhibited strong antioxidant properties and high biocompatibility, supporting their potential biomedical applications.[224] Sathishkumar *et al.*[225] synthesized *Couroupita guianensis* Aubl. fruit extract (CGFE) coated magnetite nanoparticles (CG@MNPs) and applied them to *S. aureus* MTCC 96, *E. coli* MTCC 2939, *S. typhi* MTCC 3917, and *K. penumoniae* MTCC 530 to evaluate antibacterial efficacy. CG@MNPs and crude CGFE were loaded onto sterile discs at various concentrations (25, 50, and 75 μg mL^{-1}). After a 24 h incubation period at 37 °C, the CG@MNP-loaded discs exhibited dose-dependent inhibition, as shown in Fig. 17a. Compared to Gram-positive *S. aureus* MTCC 96, CG@MNPs showed the highest zone of inhibition (Fig. 17b) against Gram-negative *E. coli* MTCC2939, *S. typhi* MTCC3917, and *K. penumoniae* MTCC 530. They observed that structural differences in the cell walls of Gram-positive and Gram-negative bacteria accounted for this variation.

Eldeeb *et al.*[132] used *Citrus sinensis* peel extract to synthesize MNPs (CS@MNPs) and evaluated their antimicrobial activity against multidrug-resistant pathogens (*S. aureus*, *Streptococcus mutans*, *Bacillus subtilis*, *E. coli*, *Klebsiella pneumoniae*, and *Candida albicans*) using a disk diffusion assay, and found that the maximum ZOI was observed at a concentration of 400 μg mL^{-1} (Table 12). The MIC of CS@MNPs (using successive dilutions of 50, 25, 12.5, 6.5, 3, and 1 μg mL^{-1}) against the target pathogens was evaluated using a microtiter plate technique. The MICs of green-synthesized CS@MNPs against *S. aureus*, *Streptococcus mutans*, *Bacillus subtilis*, *E. coli*, *Klebsiella pneumonia* and *Candida albicans* were 3, 6.5, 6.5, 12.5, 50, and 25 μg mL^{-1}, respectively. These examples emphasize the versatility and enhanced antibacterial properties imparted by bio-extract coatings on MNPs, which combine natural antimicrobial activity with the physical and magnetic features of the nanoparticle core.

Various phytogen@MNPs have distinct ZOIs against different bacteria, a few of which are listed in Table 12.

The size, charge, and shape of nanoparticles are critical factors in determining their antibacterial mechanisms and efficacy. Smaller nanoparticles possess a larger surface area-to-volume ratio, which enhances their ability to interact with bacterial surfaces and penetrate cells, thereby increasing their antibacterial activity. They are readily taken up by bacteria and can release

antimicrobial ions or react more efficiently with cellular components. The nanoparticle surface charge, which is often positive (cationic), facilitates strong electrostatic interactions with the negatively charged bacterial cell membranes. This interaction can destabilize bacterial membranes, causing leakage of contents and cell death, while also increasing the selectivity towards bacteria over mammalian cells.[233]

This shape influences the interaction of nanoparticles with bacterial cells and biofilms. Non-spherical shapes, such as cubes, discs, or sharp-edged structures, can exhibit higher surface reactivity and improved contact with bacterial membranes, resulting in more potent antibacterial activity than spherical or wire-like nanoparticles. Different shapes also present various crystal facets that influence the surface energy and reactivity. For example, nanocubes with high-energy facets often exhibit greater antibacterial potency than nanospheres. Overall, optimizing the size, charge, and shape of nanoparticles can maximize bacterial cell wall disruption, efficient cellular uptake, biofilm penetration, and targeted delivery of antimicrobial agents, leading to enhanced antibacterial mechanisms and effectiveness.

10. Advantages, safety, toxicity, and lifecycle considerations for Phytogen@MNPs

10.1 Advantages

10.1.1 Green synthesis and its advantages. Phytogen@MNPs are a sustainable and economical substitute for traditional chemical and physical synthesis techniques. Nonetheless, to guarantee their long-term use, it is essential to comprehensively assess their safety profile, potential toxicological effects, and full lifecycle impact.[234]

10.1.2 Environmental advantages. Eco-friendly synthesis techniques typically eliminate the need for harmful chemicals, elevated temperatures, and high-pressure conditions, leading to lower energy demands and minimal production of harmful byproducts. Plant extracts serve as natural reducing agents (when only Fe(III) salts are employed rather than the conventional Fe(III): Fe(II) = 2 : 1 ratio) and stabilizers, enhancing the biocompatibility of the nanoparticles and promoting their biodegradability. Magnetite nanoparticles produced using crude latex from *Jatropha curcas* and the leaf extract of *Cinnamomum tamala* have demonstrated promising capabilities in purifying wastewater. These biologically derived nanoparticles effectively eliminate organic contaminants, toxic heavy metals, and pathogenic bacteria, highlighting their potential as eco-friendly water treatment solutions.[43] Another study demonstrated the use of widely available and costless mandarin (*Citrus reticulata*) peels for the synthesis of superparamagnetic MNPs.[139]

10.2 Toxicity and safety of phytogen-coated magnetite nanoparticles

Although green synthesis methods generally lead to less toxic nanoparticles, the safety of phytogen@MNPs still requires rigorous evaluation, especially given their intended use in water purification and potential environmental release.[234]

10.2.1 Reduced toxicity profile. Phytogen@MNPs are generally considered less toxic than those synthesized *via* conventional methods because of the absence of residual toxic chemicals and presence of biocompatible organic coatings. Studies on citric acid-coated magnetite nanoparticles, a type of phytogen-derived coating, have shown that they were not phytotoxic and even stimulate the growth of soybean and alfalfa.[235] This suggests a lower risk to plant life upon environmental release. *In vitro* and *in vivo* studies on iron oxide nanoparticles, including magnetite, have demonstrated their low toxicity and high biocompatibility compared to other magnetic nanomaterials.[234] Das *et al.*[129] used *Nigella sativa* seed extract coated MNPs towards the removal of hydrocortisone. They reported that the leaching of NS@MNPs was obvious but the residual amount in the solution did not harm normal cell lines.

10.2.2 Potential toxicity concerns. Despite general low toxicity, factors such as particle size, shape, surface charge, and concentration can influence toxicological outcomes.[234] Magnetite nanoparticles, even with green coatings, can generate ROS and cause oxidative stress, which can potentially impact aquatic organisms and human health if ingested.[234] The degradation products of MNPs and their potential interactions with environmental matrices must be thoroughly investigated. A systematic review of biogenic metallic oxide NPs, including MNPs, highlighted that while some studies reported antigenotoxic effects, most found genotoxicity at specific concentrations and in a dose or time-dependent manner. This emphasizes the need for careful dose–response analysis of phytogen@MNPs. The coating material itself, even if plant-derived, can influence the interaction of the nanoparticle with biological systems. For example, some plant extracts might introduce complex organic molecules that could alter the behavior of NPs or their persistence in the environment. A fundamental aspect of nanoparticle toxicity lies in their ultra-small dimensions, which enable them to infiltrate cells and even subcellular organelles. This deep penetration can interfere with essential biological processes. Documented toxicological outcomes include tissue inflammation and a shift in cellular redox equilibrium toward oxidative stress, potentially leading to impaired cellular function or apoptosis.[236]

10.3 Lifecycle assessment of Phytogen@MNPs

A comprehensive life cycle assessment (LCA) is crucial for evaluating the environmental performance of phytogen@MNPs used in wastewater purification, from their green synthesis to eventual disposal or recycling.

10.3.1 Production phase

10.3.1.1 Raw material acquisition. The use of abundant and renewable plant materials for phytosynthesis significantly reduces the environmental burden associated with extraction and processing of synthetic chemicals.

10.3.1.2 Energy consumption. Green synthesis often requires less energy than high-temperature or high-pressure chemical methods, contributing to a lower carbon footprint.

10.3.1.3 Waste generation. Reduced use of hazardous chemicals directly translates to less toxic waste generation during the synthesis phase, aligning with sustainable practices.

10.3.2 Use phase-wastewater purification

10.3.2.1 Efficacy and reusability. Phytogen@MNPs demonstrate high efficiency in removing various pollutants, including heavy metals, organic dyes, and bacteria, from wastewater. Their magnetic properties allow for easy separation and recovery from treated water using external magnets, thereby promoting reusability and reducing operational costs.

10.3.2.2 Reduced secondary pollution. The effective removal of pollutants prevents their discharge into natural water bodies, thereby mitigating environmental contamination.

10.3.2.3 Potential for leaching. Although phytogen coatings enhance stability, the possibility of MNP leaching or degradation during continuous use in wastewater treatment systems requires evaluation. This can release nanoparticles or their breakdown products into purified water or effluents.

10.3.3 End-of-life phase

10.3.3.1 Disposal. The ultimate disposal of spent phytogen@MNPs, along with adsorbed pollutants, must be managed responsibly. Options include landfilling, incineration, or specialized waste treatment, each with its own environmental implications.

10.3.3.2 Biodegradability. The organic phytogen coating can enhance the biodegradability of nanoparticles, potentially reducing their persistence in the environment compared to synthetic polymer coatings. However, core MNPs are stable and long-lasting.[234]

10.3.4 Recycling and recovery. The magnetic separability of MNPs opens new avenues for their recovery and potential regeneration or recycling, further minimizing their environmental footprint.

10.3.5 Recommendations for comprehensive LCA. ● Future LCAs should specifically compare phytogen@MNPs with other types of coated MNPs and with conventional wastewater treatment methods to quantify their net environmental benefits.

● Data gaps regarding the long-term fate, degradation pathways, and ecological impacts of phytogen@MNPs in diverse environmental matrices (*e.g.*, soil, sediment, and aquatic systems) must be addressed.

● Standardized protocols for toxicity testing and environmental risk assessment of these nanoparticles are essential to provide reliable data for regulatory decision-making.

● An LCA should consider the entire supply chain of plant extracts, including cultivation, harvesting, and processing, to ensure that the "green" aspect is maintained throughout the process.

11. Future perspectives

Future prospects for the synthesis of phytogen@MNPs in wastewater purification using plant extracts cover several important topics, with an emphasis on resolving present issues and improving their sustainability and applicability.[237–239] Nanoparticles are a viable alternative for wastewater detoxification, which is required due to the rising water pollution caused by ongoing industrialization and urbanization.[240]

Future studies should focus on investigating new plant sources and streamlining the green synthesis process.[241] Standardizing

biochar production and conducting in-depth field research are necessary to maximize its use in anaerobic biofiltration systems for successful and economical wastewater treatment.[239]

Therefore, enhancing the effectiveness and repeatability of plant extract-mediated synthesis techniques is essential. This involves gaining a greater understanding of how plant phytochemicals function as capping and reducing agents, enabling improved control over the size, shape, and stability of nanoparticles.[151,242] The optimization of these parameters is crucial because they have a considerable impact on the reaction yield. These factors include the reaction temperature, iron precursor concentration, leaf extract concentration, and reaction time.[243] Advanced characterization methods will help clarify the characteristics of green-synthesized nanoparticles and guarantee their appropriateness for various wastewater treatment applications.[241]

Further studies should examine a wider array of plant extracts, including agricultural waste, as capping and bioreducing agents.[244] This strategy not only offers a sustainable way to synthesize nanoparticles, but also helps to value waste. The synthesis of magnetite nanoparticles, for example, can be carried out using waste natural resources, such as onion, potato, tea, and moringa wastes, with differing results in terms of efficiency, yield, size, shape, and morphology.

Future research should focus on developing multifunctional phytogen@MNPs to improve their pollutant removal capacity by integrating them into composite structures or mixing them with other materials.[241,245] Surface modification with polymers, functional groups, or other NPs may be necessary to target certain contaminants, including heavy metals, dyes, medications, and microplastics.[237,246] The magnetic properties of MNPs facilitate their efficient separation from treated wastewater using an external magnetic field, offering significant advantages in terms of recyclability and cost-effectiveness.[237]

Addressing the challenges associated with scalability, environmental impacts, and long-term performance is vital for the widespread adoption of plant-mediated MNPs in wastewater treatment.[240]

One of the biggest challenges is the development of cost-effective processes for the large-scale production of plant-mediated MNPs. Although green synthesis techniques are typically less expensive and harmful to the environment than conventional chemical and physical procedures, more studies and improvements are required before these processes can be scaled for industrial use.[237,243] The economic feasibility of these techniques is enhanced by utilizing easily accessible and reasonably priced plant extracts.[247,248]

Even though plant-mediated synthesis is regarded as "green," further research is necessary to fully understand the long-term toxicity and possible environmental effects of the produced nanoparticles.[238] To ensure safe application, studies on ecological implications—such as permanence, toxicity to non-target organisms, and release into the environment, are essential.[238] One of the main benefits of green synthesis techniques is the use of non-toxic materials in the synthesis process.[249]

To construct more complete and effective systems, future studies should focus on integrating plant-mediated MNPs with current wastewater treatment technology.[238,250] To enhance the overall treatment efficacy and handle a larger spectrum of pollutants, nanotechnology can be integrated with traditional techniques, including adsorption, photocatalytic degradation, and membrane filtration.[240,250] For instance, research has demonstrated that, compared to traditional techniques, MNP-based approaches can improve contaminant concentration and separation efficiency.[251]

12. Conclusions

The development of phytogen@MNPs represents a significant advancement in sustainable wastewater detoxification. Plant-derived extracts facilitate green synthesis, imparting biocompatibility, stability, and surface multifunctionality to MNPs, which cannot be achieved using conventional methods. Through the analysis of plant sources, synthesis techniques, and material characterization, phytogen@MNPs were found to efficiently adsorb and degrade inorganic ions and organic pollutants, including heavy metals, dyes, pesticides, and pharmaceuticals. Kinetic, isotherm, and thermodynamic studies confirmed their high efficacy, whereas their biocompatibility and lower cost of production highlighted their potential for real-world implementation. However, challenges such as organic coating degradation, iron leaching, scale-up of synthesis protocols, and long-term stability under operational conditions remain, which require further research. Moreover, the standardization of characterization methods and understanding of pollutant–surface interactions should be strengthened to optimize performance and address safety concerns. In summary, phytogen@MNPs represent a promising and versatile solution for next-generation water-purification technologies. Continuous interdisciplinary efforts in scalable production, material optimization, and field-based testing are essential to realize their potential in addressing global water pollution challenges.

Author contribution

C. Das: conceptualization, investigation, formal analysis, and writing the original draft. G. Biswas: conceptualization, reviewing and editing.

Conflicts of interest

The authors have declared that no competing interests exist.

Data availability

No new data were generated in this review article. All data supporting the conclusions of this work are derived from previously published sources, which are fully cited within the manuscript.

Acknowledgements

References

1 K. Saravanakumar, S. De Silva, S. S. Santosh, A. Sathiyaseelan, A. Ganeshalingam, M. Jamla, A. Sankaranarayanan, V. P. Veeraraghavan, D. MubarakAli, J. Lee, G. Thiripuranathar and M.-H. Wang, *Chemosphere*, 2022, **307**, 135593.

2 R. L. Bell, J. A. Kase, L. M. Harrison, K. V. Balan, U. Babu, Y. Chen, D. Macarisin, H. J. Kwon, J. Zheng, E. L. Stevens, J. Meng and E. W. Brown, *Pathogens*, 2021, **10**, 1391.

3 A. M. Jubb and H. C. Allen, *ACS Appl. Mater. Interfaces*, 2010, **2**, 2804–2812.

4 B. Rezaei, P. Yari, S. M. Sanders, H. Wang, V. K. Chugh, S. Liang, S. Mostufa, K. Xu, J. Wang, J. Gómez-Pastora and K. Wu, *Small*, 2024, **20**, 2304848.

5 S. Dutta, R. Dixit and R. K. Sharma, *Sep. Sci. Technol.*, 2022, 97–138.

6 H. Iida, K. Takayanagi, T. Nakanishi and T. Osaka, *J. Colloid Interface Sci.*, 2007, **314**, 274–280.

7 J. H. Jang and H. B. Lim, *Microchem. J.*, 2010, **94**, 148–158.

8 M. Arruebo, R. Fernández-Pacheco, M. R. Ibarra and J. Santamaría, *Nano Today*, 2007, **2**, 22–32.

9 K. Petcharoen and A. Sirivat, *Mater. Sci. Eng. B*, 2012, **177**, 421–427.

10 J. Yang, S. Park, H. Yoon, Y. Huh and S. Haam, *Int. J. Pharm.*, 2006, **324**, 185–190.

11 B. Markovic, V. Spasojevic, A. Dapcevic, Z. Vukovic, V. Pavlovic, D. Randjelovic and A. Nastasovic, *Hem. Ind.*, 2019, **73**, 25–35.

12 F. X. Hu, K. G. Neoh and E. T. Kang, *Biomaterials*, 2006, **27**, 5725–5733.

13 Z. Ma and H. Liu, *China Particuology*, 2007, **5**, 1–10.

14 S. B. Brijmohan and M. T. Shaw, *J. Memb. Sci.*, 2007, **303**, 64–71.

15 V. Aggarwal, A. Kachore, E. Bala, H. Singh, M. Selvaraj, M. A. Assiri, Saima, R. Kumar and P. K. Verma, *J. Phys. Chem. Solids*, 2026, **208**, 113060.

16 H. Singh, Himanshu, A. Kachore, V. Aggarwal, E. Bala, Saima, R. Kumar and P. K. Verma, *Langmuir*, 2025, **41**, 23163–23181.

17 H. Singh, A. Kachore, V. Aggarwal, E. Bala, Saima, R. Kumar, P. Kumar and P. K. Verma, *ChemistrySelect*, 2025, **10**(14), e202501004.

18 A. Kachore, E. Bala, V. Aggarwal, H. Singh, Saima, M. H. A. Suleiman, M. Selvaraj and P. K. Verma, *J. Ind. Eng. Chem.*, 2025, **146**, 494–505.

19 T. A. P. Rocha-Santos, *TrAC Trends Anal. Chem.*, 2014, **62**, 28–36.

20 R. Kumar, B. S. Inbaraj and B. H. Chen, *Mater. Res. Bull.*, 2010, **45**, 1603–1607.

21 Y. P. Yew, K. Shameli, M. Miyake, N. B. B. Ahmad Khairudin, S. E. B. Mohamad, T. Naiki and K. X. Lee, *Arab. J. Chem.*, 2020, **13**, 2287–2308.

22 S. Nadaf, G. K. Jena, N. Rarokar, N. Gurav, M. Ayyanar, S. Prasad and S. Gurav, *Hybrid Adv.*, 2023, **3**, 100038.

23 W. Marimon-Bolivar and N. Toussaint-Jimenez, in *2019 Congreso Internacional de Innovación y Tendencias en Ingeniería (CONIITI)*, IEEE, 2019, pp. 1–8.

24 J. Laxmi Mangamma and K. Basavaiah, *Inorg. Chem. Commun.*, 2024, **162**, 112290.

25 M. Bala, K. Pratap, P. K. Verma, B. Singh and Y. Padwad, *J. Ethnopharmacol.*, 2015, **175**, 131–137.

26 O. M. Ahmed, in *Naturally Occurring Chemicals against Alzheimer's Disease*, Elsevier, 2021, pp. 351–358.

27 P. Sharma, B. P. Dwivedee, D. Bisht, A. K. Dash and D. Kumar, *Heliyon*, 2019, **5**, e02437.

28 S. Ghosh, S. Mondol, D. Lahiri, M. Nag, T. Sarkar, S. Pati, S. Pandit, A. A. Alarfaj, M. F. Mohd Amin, H. A. Edinur, M. R. Ahmad Mohd Zain and R. R. Ray, *Front. Chem.*, 2023, **11**, 1118454.

29 R. Saini and P. Kumar, *Inorg. Chem. Commun.*, 2023, **156**, 111221.

30 B. V. Vamsi Krishna, P. Tirupathi Rao, B. Durga Lakshmi, K. Vasudha, S. Esub Basha, B. Putra Kumar, P. S. S. Kiran, K. Shreyas Chandra and R. R K, *Next Mater.*, 2024, **3**, 100171.

31 M. V. D. Prakash, S. Sampath, K. Amudha, A. Nadeem, B. S. Lopes, B. Durga and S. Muthupandian, *Mater. Technol.*, 2023, **38**, 2247908.

32 G. Vyas, S. Bhatt and P. Paul, *RSC Adv.*, 2019, **9**, 34102–34113.

33 S. Sarkar, R. P. Singh and G. Bhattacharya, *3 Biotech*, 2021, **11**, 178.

34 S. P. Patil, R. Y. Chaudhari and M. S. Nemade, *Talanta Open*, 2022, **5**, 100083.

35 H. J. Berchmans and S. Hirata, *Bioresour. Technol.*, 2008, **99**, 1716–1721.

36 N. C. Om Tapanes, D. A. Gomes Aranda, J. W. de Mesquita Carneiro and O. A. Ceva Antunes, *Fuel*, 2008, **87**, 2286–2295.

37 O. Osoniyi and F. Onajobi, *J. Ethnopharmacol.*, 2003, **89**, 101–105.

38 H. A. Abdelgadir and J. Van Staden, *South African J. Bot.*, 2013, **88**, 204–218.

39 H. Bar, D. K. Bhui, G. P. Sahoo, P. Sarkar, S. Pyne and A. Misra, *Colloids Surf., A*, 2009, **348**, 212–216.

40 N. Satpute, M. K. Ghosh, A. Kesharwani and T. K. Ghorai, *Sci. Rep.*, 2023, **13**, 22122.

41 S. Thakur, M. Shandilya and G. Guleria, *J. Environ. Chem. Eng.*, 2021, **9**, 104882.

42 V. Sharma and L. J. M. Rao, *Crit. Rev. Food Sci. Nutr.*, 2014, **54**, 433–448.

43 C. Das, S. Sen, T. Singh, T. Ghosh, S. S. Paul, T. W. Kim, S. Jeon, D. K. Maiti, J. Im and G. Biswas, *Nanomaterials*, 2020, **10**, 1615.

44 W. Hassan and S. N. Zainab Kazmi, *J. Nutr. Disord. Ther.*, 2015, **06**, 1000190.

45 A. M. Ealias, J. V. Jose and M. P. Saravanakumar, *Environ. Sci. Pollut. Res.*, 2016, **23**, 21416–21430.

46 R. Ribeiro-Santos, M. Andrade, D. Madella, A. P. Martinazzo, L. de Aquino Garcia Moura, N. R. de Melo and A. Sanches-Silva, *Trends Food Sci. Technol.*, 2017, **62**, 154–169.

47 M. Jalal, S. Ali, M. Ansari, H. Khan and S. Cameotra, *Int. J. Adv. Res.*, 2016, **4**, 428–440.

48 M. A. Al Mashud, M. Moinuzzaman, M. S. Hossain, S. Ahmed, G. Ahsan, A. Reza, R. Bin Anwar Ratul, M. H. Uddin, M. A. Momin and M. A. Hena Mostofa Jamal, *Heliyon*, 2022, **8**, e09920.

49 S. Narath, S. K. Koroth, S. S. Shankar, B. George, V. Mutta, S. Wacławek, M. Černík, V. V. T. Padil and R. S. Varma, *Nanomaterials*, 2021, **11**, 1558.

50 S. Mandal, A. Patra, A. Samanta, S. Roy, A. Mandal, T. Das Mahapatra, S. Pradhan, K. Das and D. K. Nandi, *Asian Pac. J. Trop. Biomed.*, 2013, **3**, 960–966.

51 R. P. Samy and S. Ignacimuthu, *Pharm. Biol.*, 2001, **39**, 417–420.

52 M. Seghatoleslam, F. Alipour, R. Shafieian, Z. Hassanzadeh, M. A. Edalatmanesh, H. R. Sadeghnia and M. Hosseini, *J. Tradit. Complement. Med.*, 2016, **6**, 262–268.

53 S. Jayaraman, A. Saha and V. Pawar, *Indian J. Pharm. Sci.*, 2012, **74**, 339.

54 C. Das, S. Singh, S. Bhakta, P. Mishra and G. Biswas, *Chemosphere*, 2022, **291**, 132673.

55 S. Yallappa, J. Manjanna, B. L. Dhananjaya, U. Vishwanatha, B. Ravishankar, H. Gururaj, P. Niranjana and B. S. Hungund, *Nano-Micro Lett.*, 2016, **8**, 120–130.

56 S. Dwivedi and D. Chopra, *J. Tradit. Complement. Med.*, 2014, **4**, 224–231.

57 S. Goel and P. Mishra, *Mater. Sci. Eng. C*, 2019, **104**, 109881.

58 H. G. Anlar and M. Bacanli, in *Pathology*, Elsevier, 2020, pp. 369–378.

59 A. Rajabian and H. Hosseinzadeh, in *Nuts and Seeds in Health and Disease Prevention*, Elsevier, 2020, pp. 329–355.

60 T. Yuan, P. Nahar, M. Sharma, K. Liu, A. Slitt, H. A. Aisa and N. P. Seeram, *J. Nat. Prod.*, 2014, **77**, 2316–2320.

61 B. H. Ali and G. Blunden, *Phyther. Res.*, 2003, **17**, 299–305.

62 C. Ezeh, C. Eze, M. U. Dibua, S. Emencheta and C. Ezeh, *Biomed. Biotechnol. Res. J.*, 2022, **6**, 400.

63 M. Kumar, D. Kaushik, A. Kumar, P. Gupta, C. Proestos, E. Oz, E. Orhan, J. Kaur, M. R. Khan, T. Elobeid, M. Bordiga and F. Oz, *Int. J. Food Sci. Technol.*, 2023, **58**, 2883–2892.

64 S. Waseem, Z. U. Nisa, T. Zeeshan, M. D. Ali, T. Begum, Z. N. Kayani, I. Ali and A. Ayub, *Nano-Struct. Nano-Objects*, 2024, **38**, 101212.

65 K. Saravanakumar, S. Shin, A. Sathiyaseelan and M.-H. Wang, *Mater. Lett.*, 2023, **338**, 134000.

66 M. S. H. Bhuiyan, M. Y. Miah, S. C. Paul, T. Das Aka, O. Saha, M. M. Rahaman, M. J. I. Sharif, O. Habiba and M. Ashaduzzaman, *Heliyon*, 2020, **6**, e04603.

67 B. Malaikozhundan, R. Krishnamoorthi, J. Vinodhini, K. S. N. Nambi and S. Palanisamy, *Inorg. Chem. Commun.*, 2022, **144**, 109843.

68 A. V. Samrot, S. Saigeetha, C. Y. Mun, S. Abirami, K. Purohit, P. J. J. Cypriyana, T. S. Dhas, L. Inbathamizh and S. S. Kumar, *Sci. Rep.*, 2021, **11**, 24511.

69 T. C. Jackson, T. O.-O. Uwah, A. A. Agboke, B. E. Udo and E. M. Udofa, *Soft Nanosci. Lett.*, 2018, **08**, 1–7.

70 S. Nizamuddin, A. Hymavathi, G. Yaku and U. Umesh Kumar, *Mater. Today Proc.*, 2022, **62**, 6854–6856.

71 R. Aswini, K. Jothimani, K. Kannan, R. Pothu, P. Shanmugam, R. Boddula, A. B. Radwan, G. Periyasami, P. Karthikeyan and N. Al-Qahtani, *Environ. Geochem. Health*, 2024, **46**, 334.

72 E. Vélez, G. Campillo, G. Morales, C. Hincapié, J. Osorio and O. Arnache, *J. Nanomater.*, 2018, **2018**, 1–7.

73 B. M. Chandrika, H. C. Manjunatha, L. Seenappa, R. Munirathnam, K. N. Sridhar, S. Manjunatha and A. J. C. Lourduraj, *J. Phys. Chem. Solids*, 2023, **181**, 111538.

74 D. Mukherjee, S. Ghosh, S. Majumdar and K. Annapurna, *J. Environ. Chem. Eng.*, 2016, **4**, 639–650.

75 M. Herlekar, S. Barve and R. Kumar, *J. Nanoparticles*, 2014, **2014**, 1–9.

76 P. J. Burange, M. G. Tawar, R. A. Bairagi, V. R. Malviya, V. K. Sahu, S. N. Shewatkar, R. A. Sawarkar and R. R. Mamurkar, *Bull. Natl. Res. Cent.*, 2021, **45**, 181.

77 H. Jiang, S. Sathiyavimal, L. Cai, S. Devanesan, S. R. M. Sayed, G. K. Jhanani and J. Lin, *Environ. Res.*, 2023, **236**, 116749.

78 A. I. Hussain, S. A. S. Chatha, G. M. Kamal, M. A. Ali, M. A. Hanif and M. I. Lazhari, *Int. J. Food Prop.*, 2017, **20**, 1569–1581.

79 A. K. Ambedkar, D. Gautam, S. Vikal, M. Singh, A. Kumar, A. Sanger, K. Sharma, B. P. Singh and Y. K. Gautam, *ACS Omega*, 2023, **8**, 29663–29673.

80 P. Zambare, A. Survase and S. Kanase, *Int. J. Pharm. Investig.*, 2022, **13**, 106–112.

81 K. Baruah, M. Haque, L. Langbang, S. Das, K. Aguan and A. Singha Roy, *J. Mol. Liq.*, 2021, **337**, 116422.

82 R. R. Multisona, S. Shirodkar, M. Arnold and A. Gramza-Michalowska, *Appl. Sci.*, 2023, **13**, 2134.

83 D. Khwannimit, R. Maungchang and P. Rattanakit, *Int. J. Environ. Anal. Chem.*, 2022, **102**, 5247–5263.

84 N. Shaik, B. Rehana, T. Anitha, R. Vijayalakshmi, K. Sandhya and G. Bandari, *Int. J. NANO Dimens.*, 2025, **16**(1–12), 162505.

85 S. Prabhu, T. Daniel Thangadurai, T. Indumathi and P. Kalugasalam, *Inorg. Chem. Commun.*, 2022, **146**, 110077.

86 H. N. T. Pham, Q. Van Vuong, M. C. Bowyer and C. J. Scarlett, *Technologies*, 2020, **8**, 80.

87 A. K. Potbhare, S. Yerpude, A. R. Daddemal-Chaudhary, A. Lambat, A. Mondal, K. M. Dadure, A. R. Rai, A. Abdala and R. G. Chaudhary, *Chemosphere*, 2024, **359**, 142369.

88 M. Kandiah and K. N. Chandrasekaran, *J. Nanotechnol.*, 2021, **2021**, 1–18.

89 M. Gupta, R. S. Tomar, S. Kaushik, R. K. Mishra and D. Sharma, *Front. Microbiol.*, 2018, **9**, 2030.

90 K. Velayutham, A. A. Rahuman, G. Rajakumar, T. Santhoshkumar, S. Marimuthu, C. Jayaseelan, A. Bagavan, A. V. Kirthi, C. Kamaraj, A. A. Zahir and G. Elango, *Parasitol. Res.*, 2012, **111**, 2329–2337.

91 A. Scaria, R. Jayaraj and P. S. Sudheesh, *Mater. Today Proc.*, 2023, DOI: 10.1016/j.matpr.2023.11.083.

92 M. Mukhopadhyay, M. Shaw and D. Nath, *Pharmacogn. Mag.*, 2017, **13**, 216.

93 R. S. T. Suruchi Chaudhary, V. Shrivastava and A. Jyoti, *Int. J. Pharm. Phytopharm. Res.*, 2020, **10**, 147–154.

94 S. Khurshid, S. Arif, T. M. Ali, H. M. Iqbal, M. Shaikh, H. Khurshid, Q. Akber and S. Yousaf, *Starch/Staerke*, 2022, **74**, 2100228.

95 N. Gautam, K. B. Singh, Snigdha, D. D. Upadhyay and G. Pandey, *RSC Adv.*, 2023, **13**, 23181–23196.

96 K. S. Prasad, A. Patra, G. Shruthi and S. Chandan, *J. Nanotechnol.*, 2017, **2017**, 1–6.

97 S. S. Majani, S. Sathyan, M. V. Manoj, N. Vinod, S. Pradeep, C. Shivamallu, K. N. Venkatachalaiah and S. P. Kollur, *Curr. Res. Green Sustain. Chem.*, 2023, **6**, 100367.

98 P. Wei, F. Zhao, Z. Wang, Q. Wang, X. Chai, G. Hou and Q. Meng, *Nutrients*, 2022, **14**, 4079.

99 S. Zafar, A. Ashraf, M. U. Ijaz, S. Muzammil, M. H. Siddique, S. Afzal, R. Andleeb, K. A. Al-Ghanim, F. Al-Misned, Z. Ahmed and S. Mahboob, *J. King Saud Univ. - Sci.*, 2020, **32**, 1116–1122.

100 A. Manikandan, M. Durka, M. Amutha Selvi and S. Arul Antony, *J. Nanosci. Nanotechnol.*, 2016, **16**, 448–456.

101 F. Bano, M. Baber, A. Ali, Z. Shah and S. Muhammad, *Pharmacogn. Mag.*, 2017, **13**, 33.

102 J. Khan, A. Sajjad, M. Rukh, K. Khan, S. W. Hassan and M. Zia, *Biocatal. Agric. Biotechnol.*, 2024, **61**, 103386.

103 I. Chkhikvishvili, T. Sanikidze, N. Gogia, M. Enukidze, M. Machavariani, N. Kipiani, Y. Vinokur and V. Rodov, *Oxid. Med. Cell. Longev.*, 2016, **2016**, 4216285.

104 M. Riaz, R. Ahmad, N. U. Rahman, Z. Khan, D. Dou, G. Sechel and R. Manea, *J. Ethnopharmacol.*, 2020, **255**, 112718.

105 K. S. Barnwal, Y. Gupta and N. Jaggi, *Surf. Interfaces*, 2024, **55**, 105326.

106 A. Sukhwal, D. Jain, A. Joshi, P. Rawal and H. S. Kushwaha, *IET Nanobiotechnology*, 2017, **11**, 531–537.

107 N. K. Mondal and A. Hajra, *J. Mosq. Res.*, 2016, **6**, 1–9.

108 G. Priyadarshana, N. Kottegoda, A. Senaratne, A. de Alwis and V. Karunaratne, *J. Nanomater.*, 2015, **2015**, 1–8.

109 D. Maity, S.-G. Choo, J. Yi, J. Ding and J. M. Xue, *J. Magn. Magn. Mater.*, 2009, **321**, 1256–1259.

110 G. Marchegiani, P. Imperatori, A. Mari, L. Pilloni, A. Chiolerio, P. Allia, P. Tiberto and L. Suber, *Ultrason. Sonochem.*, 2012, **19**, 877–882.

111 D. Ghanbari, M. Salavati-Niasari and M. Ghasemi-Kooch, *J. Ind. Eng. Chem.*, 2014, **20**, 3970–3974.

112 L. Cabrera, S. Gutierrez, N. Menendez, M. P. Morales and P. Herrasti, *Electrochim. Acta*, 2008, **53**, 3436–3441.

113 M. Starowicz, P. Starowicz, J. Żukrowski, J. Przewoźnik, A. Lemański, C. Kapusta and J. Banaś, *J. Nanoparticle Res.*, 2011, **13**, 7167–7176.

114 R. Reséndiz-Ramírez, A. Rodríguez-López, J. A. Díaz-Real, H. F. Delgado-Arenas, A. Osornio-Villa, R. Hernández-Leos, V. Vivier and R. Antaño-López, *ACS Omega*, 2022, **7**, 761–772.

115 J. M. M. Silva, P. E. Feuser, R. Cercená, M. Peterson and A. G. Dal-Bó, *J. Magn. Magn. Mater.*, 2023, **580**, 170925.

116 T. J. Daou, G. Pourroy, S. Bégin-Colin, J. M. Grenèche, C. Ulhaq-Bouillet, P. Legaré, P. Bernhardt, C. Leuvrey and G. Rogez, *Chem. Mater.*, 2006, **18**, 4399–4404.

117 J. A. López Pérez, M. A. López Quintela, J. Mira, J. Rivas and S. W. Charles, *J. Phys. Chem. B*, 1997, **101**, 8045–8047.

118 M. Salvador, G. Gutiérrez, S. Noriega, A. Moyano, M. C. Blanco-López and M. Matos, *Int. J. Mol. Sci.*, 2021, **22**, 427.

119 T. Nanda, A. Rathore and D. Sharma, *Front. Mater. Sci.*, 2020, **14**, 387–401.

120 H. Reza Ghorbani, H. Pazoki and A. Shokuhi Rad, *Biosci. Biotechnol. Res. Asia*, 2017, **14**, 631–633.

121 S. Dave, S. Dave, A. Mathur and J. Das, in *Nanobiotechnology*, Elsevier, 2021, pp. 225–234.

122 M. Abdeen, S. Sabry, H. Ghozlan, A. A. El-Gendy and E. E. Carpenter, *J. Nanomater.*, 2016, **2016**, 1–7.

123 T. Ahn, J. H. Kim, H.-M. Yang, J. W. Lee and J.-D. Kim, *J. Phys. Chem. C*, 2012, **116**, 6069–6076.

124 R. Massart, *IEEE Trans. Magn.*, 1981, **17**, 1247–1248.

125 R. Blakemore, *Science*, 1975, **190**, 377–379.

126 S. Mørup, M. F. Hansen and C. Frandsen, in *Comprehensive Nanoscience and Technology*, Elsevier, 2011, pp. 437–491.

127 A. O. Kalu, E. C. Egwim, A. A. Jigam and H. L. Muhammad, *Nano Express*, 2022, **3**, 045004.

128 A. Paut, L. Guć, M. Vrankić, D. Crnčević, P. Šenjug, D. Pajić, R. Odžak, M. Šprung, K. Nakić, M. Marciuš, A. Prkić and I. Mitar, *Nanomaterials*, 2024, **14**, 729.

129 C. Das, N. Nath Ghosh, R. Bhardwaj, K. Narula, P. Mishra and G. Biswas, *J. Ind. Eng. Chem.*, 2023, **128**, 369–382.

130 M. Dehghani, B. Hajipour-Verdom and P. Abdolmaleki, *Front. Chem.*, 2024, **12**, DOI: 10.3389/fchem.2024.1413077.

131 S. T. Geneti, G. A. Mekonnen, H. C. A. Murthy, E. T. Mohammed, C. R. Ravikumar, B. A. Gonfa and F. K. Sabir, *J. Nanomater.*, 2022, **2022**, 1–15.

132 B. A. Eldeeb, W. M. A. El-Raheem and S. Elbeltagi, *Sci. Rep.*, 2023, **13**, 19000.

133 A. Akbar, S. Riaz, M. Bashir and S. Naseem, *IEEE Trans. Magn.*, 2014, **50**, 1–4.

134 R. Etemadifar, A. Kianvash, N. Arsalani and E. Abouzari-Lotf, *J. Mater. Sci. Mater. Electron.*, 2018, **29**, 17144–17153.

135 P. J. Vikesland, R. L. Rebodos, J. Y. Bottero, J. Rose and A. Masion, *Environ. Sci. Nano*, 2016, **3**, 567–577.

136 J. Zhang, S. Lin, M. Han, Q. Su, L. Xia and Z. Hui, *Water*, 2020, **12**, 446.

137 A. Wojciechowska, A. Markowska-Szczupak and Z. Lendzion-Bieluń, *Materials*, 2022, **15**, 1863.

138 S. F. Soares, T. Fernandes, T. Trindade and A. L. Daniel-da-Silva, *Molecules*, 2019, **24**, 1958.

139 H. N. Nassar, H. R. Ali and N. S. El-Gendy, *Fuel*, 2021, **294**, 120534.

140 D. Kovář, A. Malá, J. Mlčochová, M. Kalina, Z. Fohlerová, A. Hlaváček, Z. Farka, P. Skládal, Z. Starčuk, R. Jiřík, O. Slabý and J. Hubálek, *J. Nanomater.*, 2017, **2017**, 1–8.

141 J. Tauc, R. Grigorovici and A. Vancu, *Phys. Status Solidi*, 1966, **15**, 627–637.

142 P. R. Jubu, F. K. Yam, V. M. Igba and K. P. Beh, *J. Solid State Chem.*, 2020, **290**, 121576.

143 B. J. Abdullah, *Mater. Sci. Semicond. Process.*, 2022, **137**, 106214.

144 M. Singh, M. Goyal and K. Devlal, *J. Taibah Univ. Sci.*, 2018, **12**, 470–475.

145 V. Golthi and J. Kommu, *Hybrid Adv.*, 2023, **4**, 100110.

146 K. Ahmouda, M. Boudiaf and B. Benhaoua, *Nanoscale Adv.*, 2022, **4**, 3250–3271.

147 W. M. Alamier, M. M. El-Moselhy, A. M. Bakry, N. Hasan and A. A. Alamri, *Crystals*, 2022, **12**, 1510.

148 C. Das, N. N. Ghosh, V. Pulhani, G. Biswas and P. Singhal, *RSC Adv.*, 2023, **13**, 15015–15023.

149 S. Fekri Aval, A. Akbarzadeh, M. R. Yamchi, F. Zarghami, K. Nejati-Koshki and N. Zarghami, *Artif. Cells, Nanomedicine, Biotechnol.*, 2016, **44**, 188–193.

150 N. D. S. Zambri, N. I. Taib, F. Abdul Latif and Z. Mohamed, *Molecules*, 2019, **24**, 3803.

151 A. Bouafia, S. E. Laouini, A. Khelef, M. L. Tedjani and F. Guemari, *J. Clust. Sci.*, 2021, **32**, 1033–1041.

152 P. K. Dhar, P. Saha, M. K. Hasan, M. K. Amin and M. R. Haque, *Clean. Eng. Technol.*, 2021, **3**, 100117.

153 A. Mohamed, R. R. Atta, A. A. Kotp, F. I. Abo El-Ela, H. Abd El-Raheem, A. Farghali, D. H. M. Alkhalifah, W. N. Hozzein and R. Mahmoud, *Sci. Rep.*, 2023, **13**, 7227.

154 L. Wu, Y. Li, Z. Fu and B.-L. Su, *Natl. Sci. Rev.*, 2020, **7**, 1667–1701.

155 L. M. Mahlaule-Glory, S. Mapetla, A. Makofane, M. M. Mathipa and N. C. Hintsho-Mbita, *Heliyon*, 2022, **8**, e10536.

156 C. Caizer, in *Handbook of Nanoparticles*, Springer International Publishing, Cham, 2016, pp. 475–519.

157 T. Q. Bui, S. N.-C. Ton, A. T. Duong and H. T. Tran, *J. Sci. Adv. Mater. Devices*, 2018, **3**, 107–112.

158 S. Chowdhury, N. Khan, G.-H. Kim, J. Harris, P. Longhurst and N. S. Bolan, in *Environmental Materials and Waste*, Elsevier, 2016, pp. 569–589.

159 J. Hwang, D. Choi, S. Han, S. Y. Jung, J. Choi and J. Hong, *Sci. Rep.*, 2020, **10**, 7391.

160 M. S. Bhuyan, *Front. Environ. Sci.*, 2022, **10**, 827289.

161 N. Nassiri Koopaei and M. Abdollahi, *DARU J. Pharm. Sci.*, 2017, **25**, 9.

162 S. Singh, K. L. Wasewar and S. K. Kansal, in *Inorganic Pollutants in Water*, Elsevier, 2020, pp. 173–203.

163 M. Kumar, P. Borah and P. Devi, in *Inorganic Pollutants in Water*, Elsevier, 2020, pp. 33–49.

164 N. A. A. Qasem, R. H. Mohammed and D. U. Lawal, *npj Clean Water*, 2021, **4**, 36.

165 P. B. Tchounwou, C. G. Yedjou, A. K. Patlolla and D. J. Sutton, *Exp. Suppl.*, 2012, **101**, 133–164.

166 M. Jaishankar, T. Tseten, N. Anbalagan, B. B. Mathew and K. N. Beeregowda, *Interdiscip. Toxicol.*, 2014, **7**, 60–72.

167 J. P. S. Cabral, *Int. J. Environ. Res. Public Health*, 2010, **7**, 3657–3703.

168 I. Ali and V. K. Gupta, *Nat. Protoc.*, 2006, **1**, 2661–2667.

169 M. N. Chong, B. Jin, C. W. K. Chow and C. Saint, *Water Res.*, 2010, **44**, 2997–3027.

170 L. Jiang, Y. Tu, X. Li and H. Li, *E3S Web Conf.*, 2018, **38**, 01037.

171 M. Al Sharabati, R. Abokwiek, A. Al-Othman, M. Tawalbeh, C. Karaman, Y. Orooji and F. Karimi, *Environ. Res.*, 2021, **202**, 111694.

172 Z. N. Garba, W. Zhou, I. Lawan, W. Xiao, M. Zhang, L. Wang, L. Chen and Z. Yuan, *J. Environ. Manage.*, 2019, **241**, 59–75.

173 D. T. Bankole, A. P. Oluyori and A. A. Inyinbor, *Arab. J. Chem.*, 2023, **16**, 104699.

174 S. Moosavi, C. W. Lai, S. Gan, G. Zamiri, O. Akbarzadeh Pivehzhani and M. R. Johan, *ACS Omega*, 2020, **5**, 20684–20697.

175 Z. Moradi, S. Z. Jahromi and M. Ghaedi, *Interface Sci. Technol.*, 2021, 557–623.

176 K. Liu, J. C.-C. Yu, H. Dong, J. C. S. Wu and M. R. Hoffmann, *Environ. Sci. Technol.*, 2018, **52**, 12667–12674.

177 S. Lotfi, K. Fischer, A. Schulze and A. I. Schäfer, *Nat. Nanotechnol.*, 2022, **17**, 417–423.

178 Y. Shi, Y. Zhang, Y. Cui, J. Shi, X. Meng, J. Zhang and H. He, *Carbohydr. Polym.*, 2019, **222**, 114972.

179 N. S. Awwad, A. El-Khalafawy, H. A. Ibrahium and M. S. Hamdy, *Mater. Res. Express*, 2019, **6**, 095907.

180 M. Jiménez-Salcedo, M. Monge and M. T. Tena, *J. Environ. Chem. Eng.*, 2021, **9**, 105827.

181 E. Darezereshki, A. khodadadi Darban, M. Abdollahy and A. Jamshidi-Zanjani, *Environ. Nanotechnology, Monit. Manag.*, 2018, **10**, 51–62.

182 K. O. Yoro, M. K. Amosa, P. T. Sekoai, J. Mulopo and M. O. Daramola, *Int. J. Sustain. Eng.*, 2020, **13**, 54–67.

183 F. P. Fato, D.-W. Li, L.-J. Zhao, K. Qiu and Y.-T. Long, *ACS Omega*, 2019, **4**, 7543–7549.

184 A. Andelescu, M. A. Nistor, S. G. Muntean and M. E. Rădulescu-Grad, *Sep. Sci. Technol.*, 2018, **53**, 2352–2364.

185 N. Ayawei, A. N. Ebelegi and D. Wankasi, *J. Chem.*, 2017, **2017**, 1–11.

186 R. Rezaei Kalantary, E. Dehghanifard, A. Mohseni-Bandpi, L. Rezaei, A. Esrafili, B. Kakavandi and A. Azari, *Desalin. Water Treat.*, 2016, **57**, 16445–16455.

187 P. B. Hassan, R. O. Rasheed and K. Zargoosh, *J. Nanomater.*, 2022, **2022**, 1–18.

188 A. Siddiqa, M. H. Khatun and M. G. Mostafa, *Desalin. Water Treat.*, 2025, **321**, 100979.

189 H. P. Toledo-Jaldin, V. Sánchez-Mendieta, A. Blanco-Flores, G. López-Téllez, A. R. Vilchis-Nestor and O. Martín-Hernández, *Environ. Sci. Pollut. Res.*, 2020, **27**, 7872–7885.

190 J. Garvasis, A. R. Prasad, K. O. Shamsheera, T. A. Nidheesh Roy and A. Joseph, *Mater. Res. Bull.*, 2023, **160**, 112130.

191 M. Rahmayanti, A. Nurul Syakina, I. Fatimah and T. Sulistyaningsih, *Chem. Phys. Lett.*, 2022, **803**, 139834.

192 A. N. Syakina and M. Rahmayanti, *Chem. Data Collect.*, 2023, **44**, 101003.

193 Á. de J. Ruíz-Baltazar, S. Y. Reyes-López, M. de L. Mondragón-Sánchez, A. I. Robles-Cortés and R. Pérez, *Results Phys.*, 2019, **12**, 989–995.

194 B. Kumar, K. Smita, L. Cumbal, A. Debut, S. Galeas and V. H. Guerrero, *Mater. Chem. Phys.*, 2016, **179**, 310–315.

195 M. S. S. Bhuiya, Md. Anwarul Kabir, Md. Shahnawaz Parvez, J. Nasrin, Md Shoeb, Md A. Rahman, Md. A. Islam and T. Islam, *Int. J. Biosci.*, 2023, **23**(4), 110–124, DOI: 10.12692/ijb/23.4.110-124.

196 K. Ahmouda, M. Boudiaf, D. Barani and B. Benhaoua, *J. Photochem. Photobiol. A Chem.*, 2024, **450**, 115442.

197 Z.-Y. Yao, J.-H. Qi and L.-H. Wang, *J. Hazard. Mater.*, 2010, **174**, 137–143.

198 T. M. Budnyak, M. Błachnio, A. Slabon, A. Jaworski, V. A. Tertykh, A. Deryło-Marczewska and A. W. Marczewski, *J. Phys. Chem. C*, 2020, **124**, 15312–15323.

199 R. Singh and R. Bhateria, *ACS Omega*, 2020, **5**, 10826–10837.

200 I. Fatimah, E. Zunita Pratiwi and W. Prio Wicaksono, *Egypt. J. Aquat. Res.*, 2020, **46**, 35–40.

201 F. Chen, Q. Yang, X. Li, G. Zeng, D. Wang, C. Niu, J. Zhao, H. An, T. Xie and Y. Deng, *Appl. Catal. B Environ.*, 2017, **200**, 330–342.

202 S. Dong, L. Cui, Y. Zhao, Y. Wu, L. Xia, X. Su, C. Zhang, D. Wang, W. Guo and J. Sun, *Appl. Surf. Sci.*, 2019, **463**, 659–667.

203 H. Wang, X. Yuan, Y. Wu, G. Zeng, H. Dong, X. Chen, L. Leng, Z. Wu and L. Peng, *Appl. Catal. B Environ.*, 2016, **186**, 19–29.

204 F. Chen, Q. Yang, C. Niu, X. Li, C. Zhang, J. Zhao, Q. Xu, Y. Zhong, Y. Deng and G. Zeng, *Catal. Commun.*, 2016, **73**, 1–6.

205 M. Pelaez, P. Falaras, V. Likodimos, K. O'Shea, A. A. de la Cruz, P. S. M. Dunlop, J. A. Byrne and D. D. Dionysiou, *J. Mol. Catal. A Chem.*, 2016, **425**, 183–189.

206 J. T. Schneider, D. S. Firak, R. R. Ribeiro and P. Peralta-Zamora, *Phys. Chem. Chem. Phys.*, 2020, **22**, 15723–15733.

207 X. Zhang, T. Guo, X. Wang, Y. Wang, C. Fan and H. Zhang, *Appl. Catal. B Environ.*, 2014, **150–151**, 486–495.

208 F. Alcalde-Garcia, S. Prasher, S. Kaliaguine, J. R. Tavares and M.-J. Dumont, *ACS Eng. Au*, 2023, **3**, 443–460.

209 A. Kumar Das, A. Marwal and R. Verma, *Nano Hybrids*, 2014, **7**, 69–86.

210 D. F. Mercado, P. Caregnato, L. S. Villata and M. C. Gonzalez, *J. Inorg. Organomet. Polym. Mater.*, 2018, **28**, 519–527.

211 H. M. Fahmy, F. M. Mohamed, M. H. Marzouq, A. B. E.-D. Mustafa, A. M. Alsoudi, O. A. Ali, M. A. Mohamed and F. A. Mahmoud, *Bionanoscience*, 2018, **8**, 491–503.

212 M. Alvarado, A. E. Matías Reyes, A. Cruz-Orea, J. Santoyo-Salazar, F. A. Domínguez-Pacheco, C. Hernández-Aguilar and A. A. Duran-Ledezma, *Rev. Mex. Física*, 2024, **70**, 011601.

213 M. A. J. Kouhbanani, N. Beheshtkhoo, S. Taghizadeh, A. M. Amani and V. Alimardani, *Adv. Nat. Sci. Nanosci. Nanotechnol.*, 2019, **10**, 015007.

214 E. Ghoohestani, F. Samari, A. Homaei and S. Yosuefinejad, *Sci. Rep.*, 2024, **14**, 84.

215 M. M. S. Abdullah, A. M. Atta, H. A. Allohedan, H. Z. Alkhathlan, M. Khan and A. O. Ezzat, *Nanomaterials*, 2018, **8**, 855.

216 G. Magnacca, A. Allera, E. Montoneri, L. Celi, D. E. Benito, L. G. Gagliardi, M. C. Gonzalez, D. O. Mártire and L. Carlos, *ACS Sustain. Chem. Eng.*, 2014, **2**, 1518–1524.

217 K. Csach, A. Juríková, J. Miškuf, M. Koneracká, V. Závišová, M. Kubovčíková and P. Kopčanský, *Mater. Sci. Forum*, 2014, **782**, 607–610.

218 S. Jafarirad, P. Hajat Ardehjani and A. Movafeghi, *J. Environ. Sci. Heal. Part A*, 2019, **54**, 516–527.

219 L. S. Ganapathe, M. A. Mohamed, R. Mohamad Yunus and D. D. Berhanuddin, *Magnetochemistry*, 2020, **6**, 68.

220 X. Guan, J. Guo, H. Zhang, S. Tao, G. Mailhot, F. Wu and J. Xu, *Molecules*, 2022, **27**, 8037.

221 D. Uzunoğlu and A. Özer, *ACS Appl. Bio Mater.*, 2022, **5**, 5465–5476.

222 P. Shanmugam, S. Boonyuen, Y. Tangjaideborisu, P. Na Nakorn, S. Tantayanon, R. Pothu and R. Boddula, *Inorg. Chem. Commun.*, 2023, **156**, 111291.

223 M. M. Zaman, M. A. S. Karal, M. N. I. Khan, A. R. M. Tareq, S. Ahammed, M. Akter, A. Hossain and A. K. M. A. Ullah, *ChemistrySelect*, 2019, **4**, 7824–7831.

224 J. Sandhya and S. Kalaiselvam, *Mater. Res. Express*, 2020, **7**, 015045.

225 G. Sathishkumar, V. Logeshwaran, S. Sarathbabu, P. K. Jha, M. Jeyaraj, C. Rajkuberan, N. Senthilkumar and S. Sivaramakrishnan, *Artif. Cells, Nanomedicine, Biotechnol.*, 2018, **46**, 589–598.

226 A. N. Abdel Rahman, S. R. Masoud, M. M. S. Fouda, A. A. Abdelwarith, E. M. Younis, S. S. Khalil, H. T. Zaki, E. Mohammed, S. J. Davies and R. E. Ibrahim, *Aquac. Reports*, 2023, **32**, 101692.

227 S. Amutha and S. Sridhar, *J. Innov. Pharm. Biol. Sci.*, 2018, **5**(2), 22–26.

228 M. Alavi, N. Karimi and T. Valadbeigi, *ACS Biomater. Sci. Eng.*, 2019, **5**, 4228–4243.

229 G. Jagathesan and P. Rajiv, *Biocatal. Agric. Biotechnol.*, 2018, **13**, 90–94.

230 J. K. Patra, M. S. Ali, I.-G. Oh and K.-H. Baek, *Artif. Cells, Nanomedicine, Biotechnol.*, 2017, **45**, 349–356.

231 V. Veeramanikandan, G. C. Madhu, V. Pavithra, K. Jaianand and P. Balaji, *Int. J. Agric. Innov. Res.*, 2017, **6**(2), 242–250.

232 R. Golabiazar, *Iran. J. Chem. Chem. Eng.*, 2023, **42**, 2745–2756.

233 A. Menichetti, A. Mavridi-Printezi, D. Mordini and M. Montalti, *J. Funct. Biomater.*, 2023, **14**, 244.

234 S. Feijoo, S. González-García, Y. Moldes-Diz, C. Vazquez-Vazquez, G. Feijoo and M. T. Moreira, *J. Clean. Prod.*, 2017, **143**, 528–538.

235 M. F. Iannone, M. D. Groppa, M. S. Zawoznik, D. F. Coral, M. B. Fernández van Raap and M. P. Benavides, *Ecotoxicol. Environ. Saf.*, 2021, **211**, 111942.

236 C. Buzea, I. I. Pacheco and K. Robbie, *Biointerphases*, 2007, **2**, MR17–MR71.

237 A. Lourens, A. Falch and R. Malgas-Enus, *J. Mater. Sci.*, 2023, **58**, 2951–2970.

238 D. B. Olawade, O. Z. Wada, O. Fapohunda, B. I. Egbewole, O. Ajisafe and A. O. Ige, *Front. Nanotechnol.*, 2024, **6**, 1427843, DOI: 10.3389/fnano.2024.1427843.

239 A. Adenike Adesina, I. Uwanaobong Adeyeye, O. Ebunlomo Okuneye and Y. Temitope Abdulkareem, *J. Eng. Technol. Adv.*, 2025, **22**, 097–112.

240 J. Kaur, K. Kaur, K. Kaur, A. S. Matharu and S. K. Mehta, 04, *Adv. Environ. Eng. Res.*, 2023, 1–56.

241 S. Kumar, S. Jain and B. Y. Lamba, *Int. J. Environ. Anal. Chem.*, 2023, **103**, 6510–6525.

242 J. O. Adeyemi, A. O. Oriola, D. C. Onwudiwe and A. O. Oyedeji, *Biomolecules*, 2022, **12**, 627.

243 A. Ebrahiminezhad, A. Zare-Hoseinabadi, A. K. Sarmah, S. Taghizadeh, Y. Ghasemi and A. Berenjian, *Mol. Biotechnol.*, 2018, **60**, 154–168.

244 H. M. Ahmed, M. A. El-khateeb, N. A. Sobhy, M. M. Hefny and F. M. Abdel-Haleem, in *The 7th International Electronic Conference on Water Sciences*, MDPI, Basel Switzerland, 2023, p. 99.

245 E. C. Nnadozie and P. A. Ajibade, *Molecules*, 2020, **25**, 4110.

246 R. Indhur, I. Amoah, F. Bux and S. Kumari, *ACS ES&T Water*, 2023, **3**, 3741–3754.

247 S. Some, S. Das, R. Mondal, M. Gangopadhyay and G. K. Basak, *Int. J. PLANT Environ.*, 2021, **7**, 119–132.

248 A. Omidvari, F. Manteghi, B. Sohrabi and Y. Afra, in *Proceedings of the 18th International Electronic Conference on Synthetic Organic Chemistry*, MDPI, Basel, Switzerland, 2014.

249 A. Sharma, H. Goel, S. Sharma, H. S. Rathore, I. Jamir, A. Kumar, S. C. Thimmappa, K. K. Kesari and B. K. Kashyap, *Environ. Sci. Pollut. Res.*, 2024, **31**, 58263–58293.

250 A. Salama, R. Abouzeid, W. S. Leong, J. Jeevanandam, P. Samyn, A. Dufresne, M. Bechelany and A. Barhoum, *Nanomaterials*, 2021, **11**, 3008.

251 N. S. Omar, L. I. Abd Ali, A. F. Qader and R. A. Omer, *Rev. Inorg. Chem.*, 2025, **45**(4), 921–932, DOI: 10.1515/revic-2024-0117.